Jül-4357

Institut für Kernphysik (IKP-4)
Helmholtz-Institut für Strahlen- und Kernphysik,
University of Bonn, Germany

Counteracting Trapped Ion Effects in the HESR

Frank Hinterberger

Member of the Helmholtz Association

JÜLICH
FORSCHUNGSZENTRUM

Counteracting Trapped Ion Effects in the HESR

Frank Hinterberger

Berichte des Forschungszentrums Jülich; 4357
ISSN 0944-2952
Institut für Kernphysik (IKP-4)
Jül-4357

Vollständig frei verfügbar im Internet auf dem Jülicher Open Access Server (JUWEL)
unter http://www.fz-juelich.de/zb/juwel

Zu beziehen durch: Forschungszentrum Jülich GmbH · Zentralbibliothek, Verlag
D-52425 Jülich · Bundesrepublik Deutschland
☎ 02461 61-5220 · Telefax: 02461 61-6103 · e-mail: zb-publikation@fz-juelich.de

Counteracting Trapped Ion Effects in the HESR

Frank Hinterberger
Helmholtz-Institut für Strahlen- und Kernphysik, University of Bonn, Germany

Abstract
Methods to counteract trapped ion effects in the High-Energy Storage Ring HESR are studied in the present report. The circulating antiproton beam ionizes the residual gas molecules of the UHV vacuum. The produced ions are trapped in the negative potentential well of the antiproton beam. Trapped ions can be extracted using either single isolated clearing electrodes or continuous clearing electrodes. In addition resonant transverse shaking of trapped ions and damping of coherent ion-beam oscillations can be used in order to reduce the adverse effects of trapped ions. In the region of dipole magnets the problem of trapped ions can be mitigated by upgrading the UHV vacuum, i.e. by sputtering thin-film NEG coatings onto the surfaces of the vacuum chamber and by using heat jackets along the beam tubes. The highest clearing efficiencies in dipole magnets can be achieved by extracting the trapped ions in the vertical direction along the magnetic field lines. A distinctive feature of the HESR ring is the internal PANDA target which deteriorates the vacuum by a huge local pressure bump. Near the PANDA target continuous clearing electrodes are necessary in order to counteract the high production rate of trapped ions. In the region of the electron cooler (EC) the optimum neutralization is reached if $\eta = 1/\gamma_e^2$. Then, the azimuthal cross-field drift velocity of the electrons is zero and the space-charge potential is reduced. A stable neutralization with $\eta = 1/\gamma_e^2$ can be achieved using the Ion-Cyclotron-Resonance (ICR) heating. The ICR heating can be realized using the electrodes of the beam position monitors. The RF can be tuned to be in resonance with the characteristic cyclotron frequencies of the ion species in the magnetic field of the EC solenoid.

Contents

1. Introduction

The present report continues a recent study entitled 'Ion Trapping in the High-Energy Storage Ring HESR' [1]. It is devoted to the question of how to counteract trapped ion effects in the HESR. The problem of trapped ions in the HESR has also been studied in two previous reports [2, 3].

The High-Energy Storage Ring (HESR) of the future International Facility for Antiprotons and Ion Research (FAIR) at GSI in Darmstadt is designed as synchrotron and storage ring for antiprotons in the momentum range 1.5 – 15 GeV/c [4, 5]. Internal target experiments with antiprotons are planned by the PANDA collaboration [6]. In addition, two other collaborations (PAX [7, 8], ASSIA [9]) proposed spin physics experiments with polarized antiprotons.

The effects of trapped ions and trapped electrons have been observed in many accelerators and storage rings [10, 11, 12, 13, 14, 15, 16, 17, 18, 19, 20, 21]. The beam particles interact with the molecules of the residual gas in the vacuum and produce positive ions and electrons. Electrons are trapped in positive particle beams while ions are trapped in negative particle beams. The trapped particles can cause emittance growth, instabilities, coherent beam-ion oscillations and beam losses. Adverse effects of trapped ions have been observed at the CERN Antiproton Accumulator (AA), the Fermilab Accumulator and the Fermilab Recycler Ring (RR). Various methods have been used in order to remove the ions.

For the sake of completeness we resume some chapters from the recent report [1]. We first show the HESR lattice in Sect. 2., present the electric field of the antiproton beam in Sect. 3., show the updated UHV vacuum in Sect. 4., discuss the ionization process in Sect. 5., evaluate the mean thermal velocities of trapped ions in Sect. 6., define the terms production time T_p, clearing time T_c and neutralization η in Sect. 7. and sketch the ion motion in dipole magnets and solenoids in Sects. 8. and 9..

The main part of the present report is devoted to the important question of how to counteract trapped ion effects in the HESR. The extraction of trapped ions using either single isolated clearing electrodes or continuous clearing electrodes is presented in Sect. 10.. The extraction of trapped ions in the region of solenoids is studied in Sect. 11.. The problem of the very high neutralization in the neighbourhood of the PANDA target is studied in Sect. 12.. The mitigation of trapped ion effects in dipole magnets and the feasibility of continuous clearing electrodes is studied in Sect. 13.. The damping of coherent beam-ion oscillations is studied in Sect. 14.. The resonant transverse beam shaking is studied in Sect. 15.. The special problems of trapped ions in the region of the electron cooler (EC) are investigated in Sects. 16.-18..

2. HESR Layout and Beam Parameters

The layout of the HESR ring is shown in Fig. 1. The circumference C amounts to 575.2 m. In Fig. 2, the lattice functions β_x, β_y and the horizontal dispersion D_x of the standard HESR optics 'optic4' with $\gamma_{tr} = 6.2$, $Q_x = 7.5995$ and $Q_y = 7.6216$ are shown as a function of s with $s = 0$ at the beginning of the North arc (upper arc in Fig. 1). The beta functions amount to about 175 m in the region of the electron cooler and about 2 m in the region of the PANDA target. In Figs. 3 and 4, the beam envelopes, i.e. the 1-sigma values σ_x and σ_y, are plotted as a function of s for $1.0 \cdot 10^{11}$ antiprotons at 15 GeV/c.

For the calculation of the negative potential well of the antiproton beam we need the beam envelopes σ_x and σ_y as a function of s. We perform the calculations using the standard optics 'optic4' and the HESR List of beam parameters from July 2011 [22]. We calculate the envelopes assuming stochastic cooling. The effective target density of the PANDA target will be $4.0 \cdot 10^{15}$ hydrogen atoms per cm^2 if the pellet target is used. The stochastic cooling will be adjusted such that the transverse emittance growth by the beam-target interactions is compensated and the highest-possible momentum resolution is achieved. Therefore, the transverse rms emittances stay constant and we can assume normalized rms emittances ϵ_x and ϵ_y as given by the RESR beam at HESR injection. The longitudinal emittance is characterized by a long bunch of constant length $L_1 = 0.9C$ and the relative rms momentum spread δ. The rms values of δ which can be achieved with stochastic cooling are taken for the calculation of the envelopes. They are listed below. The corresponding momentum spreads are lesser than the momentum spreads at injection.

We assume the geometric rms emittances without cooling as given by the RESR beam at HESR injection. The kinetic energy at injection amounts to 3.0 GeV, the corresponding beam momentum is 3.825 GeV/c and $\beta\gamma = 4.077$. The normalized geometric rms emittances[1] $\epsilon_{x,y}^{normalized}$ amount to 1.0 mm mrad for $3.5 \cdot 10^{10}$ antiprotons in the ring. They scale as $(N_{\bar{p}}/3.5 \cdot 10^{10})^{4/5}$ with the number $N_{\bar{p}}$ of antiprotons. The relative rms momentum spread scales as $(N_{\bar{p}}/3.5 \cdot 10^{10})^{2/5}$. Taking as reference values the emittances ϵ_3 and relative beam spreads δ_3 at injection energy $T_{\bar{p}} = 3.0$ GeV one has

- $N_{\bar{p}} = 1.0 \cdot 10^{11}$: $\epsilon_3 = 0.58$ mm mrad, $\delta_3 = 0.50 \cdot 10^{-3}$,
- $N_{\bar{p}} = 1.0 \cdot 10^{10}$: $\epsilon_3 = 0.089$ mm mrad $\delta_3 = 0.20 \cdot 10^{-3}$.

Accelerating or decelerating the injected beam yields geometric rms emittances $\epsilon = \epsilon_x = \epsilon_y$ and relative rms momentum spreads δ which scale according to the adiabatic damping law,

$$\begin{aligned} \epsilon &= \epsilon_3 \frac{\beta_3\gamma_3}{\beta\gamma} \\ \delta &= \delta_3 \frac{\beta_3\gamma_3}{\beta\gamma} \end{aligned} \tag{1}$$

As mentioned, these values are kept constant by stochastic cooling during the measurements with the PANDA target.

At the beginning, the HESR will be operated with the collector ring (CR) as injector. Then, the start rms emittance at 3 GeV will be $\epsilon_3 = 1.25$ mm mrad and the relative rms momentum spread $\delta_3 = 0.25 \cdot 10^{-3}$. We assume the barrier bucket mode of operation with a bunch length $L_1 = 0.9C$ and a beam free gap of length $L_2 = 0.1C$. The circumference C amounts to 575.2 m.

[1] $\epsilon_{x,y}^{normalized} = \epsilon_{x,y}\beta\gamma$

Assuming Gaussian beam distributions the envelopes are represented by the one standard deviations $\sigma_x(s)$ and $\sigma_y(s)$,

$$\begin{aligned} \sigma_x &= \sqrt{\epsilon_x \beta_x + (D_x \delta)^2} \\ \sigma_y &= \sqrt{\epsilon_y \beta_y}. \end{aligned} \tag{2}$$

Here, ϵ_x and ϵ_y represent the geometrical rms emittances, β_x and β_y the horizontal and vertical beta-functions, δ the rms width of the relative momentum deviation and D_x is the horizontal dispersion. The momentum range of the HESR ring is between 1.5 GeV/c and 15 GeV/c. Usually, four standard momenta are considered. Here, we list the beam parameters ϵ and δ which are used for the calculation of the envelopes assuming 10^{11} antiprotons in the HESR ring,

1. S1: $p = 1.5$ GeV/c, $T = 0.831$ GeV, $\epsilon = 1.48$ mm mrad, $\delta = 1.9 \cdot 10^{-4}$,
2. S2: $p = 3.825$ GeV/c, $T = 3.0$ GeV, $\epsilon = 0.58$ mm mrad, $\delta = 1.4 \cdot 10^{-4}$,
3. S3: $p = 8.889$ GeV/c, $T = 8.0$ GeV, $\epsilon = 0.25$ mm mrad, $\delta = 1.2 \cdot 10^{-4}$,
4. S4: $p = 15$ GeV/c, $T = 14.091$ GeV. $\epsilon = 0.148$ mm mrad, $\delta = 0.9 \cdot 10^{-4}$.

The corresponding list for 10^{10} antiprotons reads

1. S1: $p = 1.5$ GeV/c, $T = 0.831$ GeV, $\epsilon = 0.23$ mm mrad, $\delta = 1.1 \cdot 10^{-4}$,
2. S2: $p = 3.825$ GeV/c, $T = 3.0$ GeV, $\epsilon = 0.089$ mm mrad, $\delta = 5.1 \cdot 10^{-5}$,
3. S3: $p = 8.889$ GeV/c, $T = 8.0$ GeV, $\epsilon = 0.043$ mm mrad, $\delta = 5.4 \cdot 10^{-5}$,
4. S4: $p = 15$ GeV/c, $T = 14.091$ GeV. $\epsilon = 0.023$ mm mrad, $\delta = 3.9 \cdot 10^{-5}$.

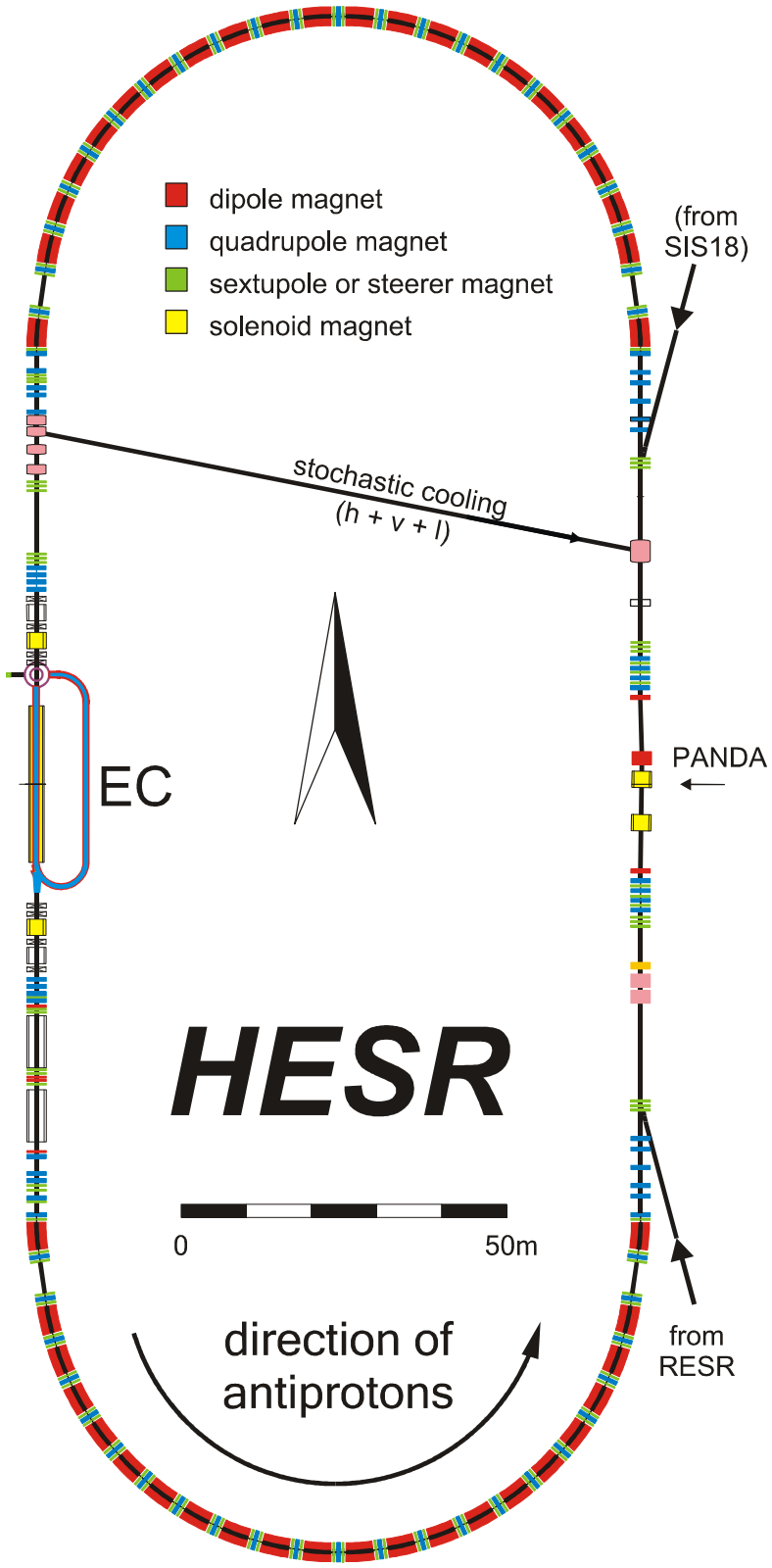

Fig. 1: Layout of the HESR ring.

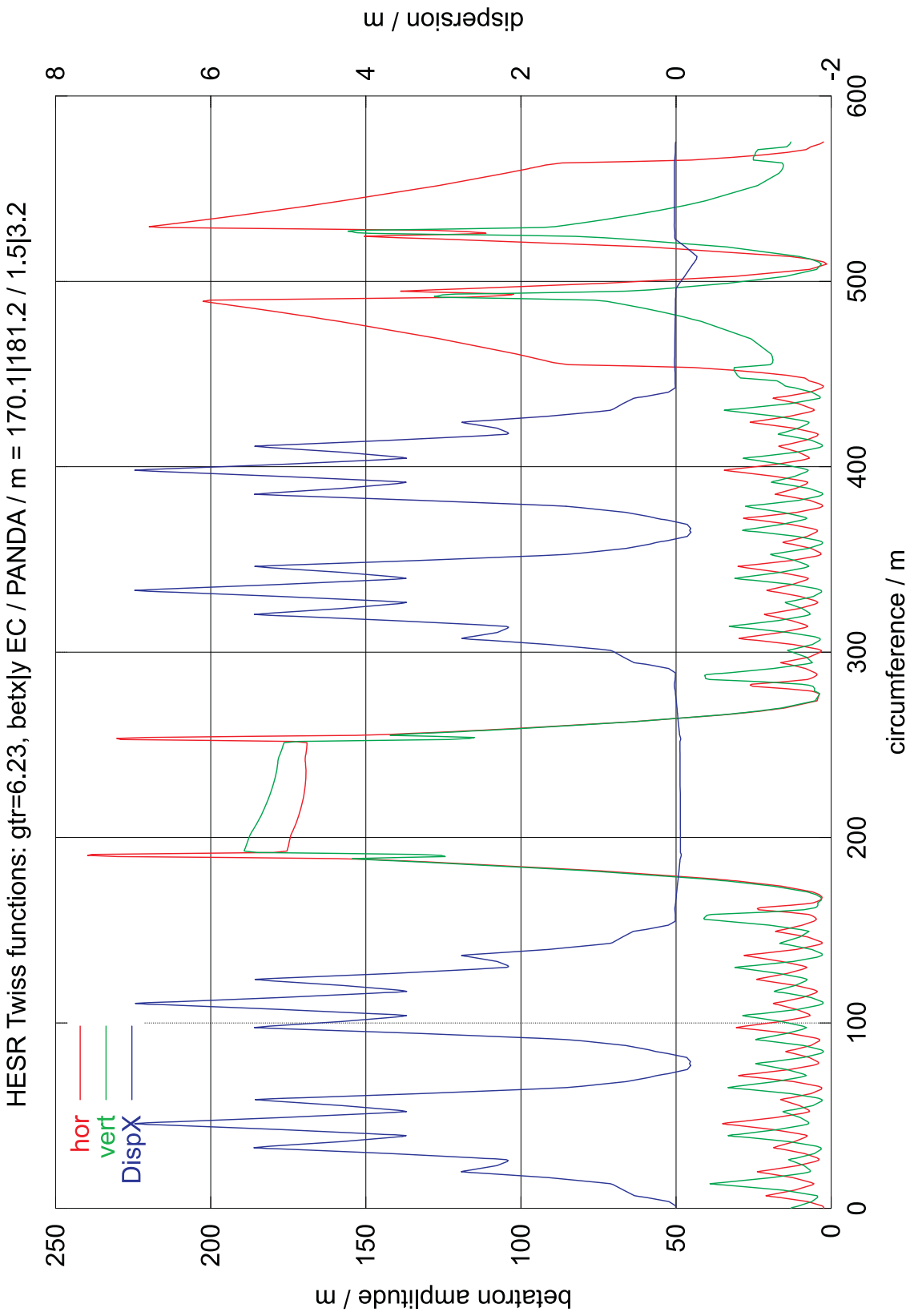

Fig. 2: The lattice functions β_x, β_y and the dispersion D_x of the standard HESR optics with $\gamma_{tr} = 6.2$.

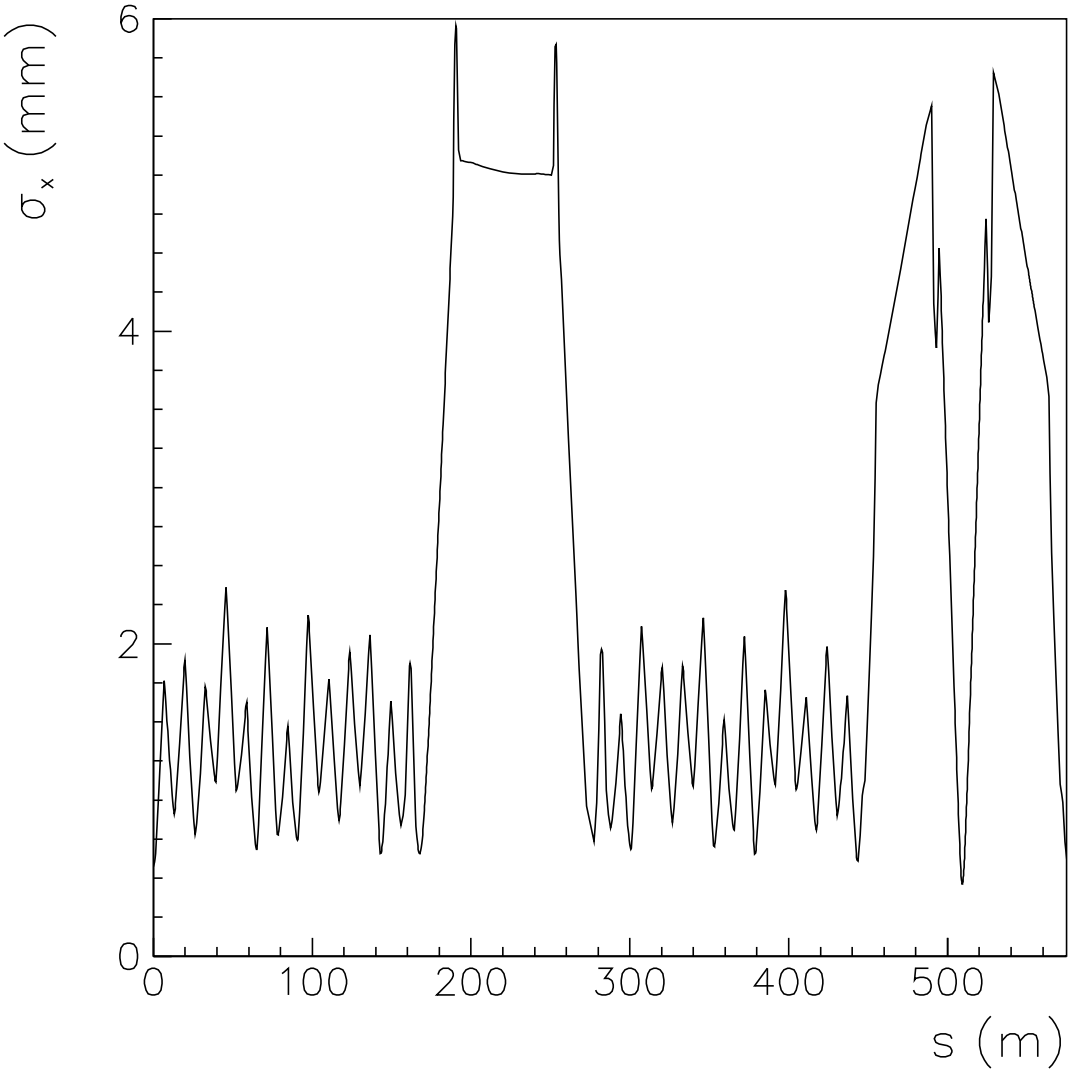

Fig. 3: Horizontal beam envelope $\sigma_x(s)$ for $1.0 \cdot 10^{11}$ antiprotons at 15 GeV/c. The electron cooler is located between $s = 207.390$ m and $s = 231.890$ m. The PANDA target is located at $s = 509.481$ m.

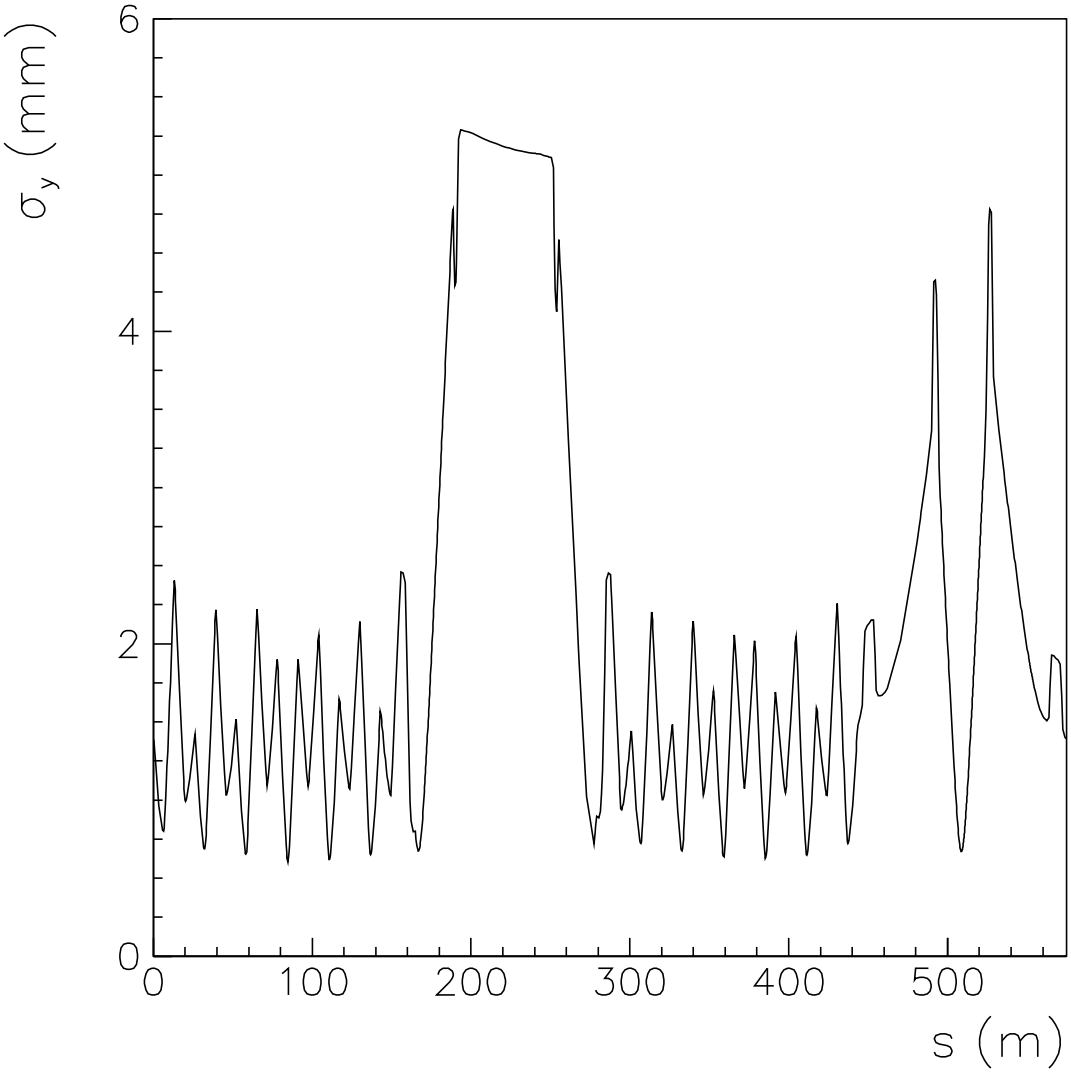

Fig. 4: Vertical beam envelope $\sigma_y(s)$ for $1.0 \cdot 10^{11}$ antiprotons at 15 GeV/c. The electron cooler is located between $s = 207.390$ m and $s = 231.890$ m. The PANDA target is located at $s = 509.481$ m.

3. Electric Field of the Antiproton Beam

3.1 Potential well and electric field of a round beam of constant density

The potential well of the antiproton beam can be calculated for various particle distributions and beam pipe profiles. The simplest case is to assume a round beam pipe of radius r_c and a round beam of constant density within the radius a. The linear charge density λ is

$$\lambda = -\frac{N_{\bar{p}} e}{L_1}. \tag{3}$$

Here, $N_{\bar{p}}$ is the number of stored antiprotons, e the elementary charge and L_1 the length of the barrier bucket bunches, e.g. $L_1 = 0.9\,C = 517.68$ m. The potential $U(r)$, with the constraint $U(r_c) = 0$ at the surface of the beam pipe, is given by

$$\begin{aligned} U(r) &= \frac{\lambda}{2\pi\epsilon_0} \ln \frac{r_c}{r} \quad r \geq a, \\ U(r) &= \frac{\lambda}{2\pi\epsilon_0} \left[\frac{1}{2} - \frac{r^2}{2a^2} + \ln\left(\frac{r_c}{a}\right) \right] \quad r \leq a. \end{aligned} \tag{4}$$

We note that $\lambda/(2\pi\epsilon_0) = -0.556$ V for $1.0 \cdot 10^{11}$ antiprotons in the ring. The corresponding electric field E_r reads

$$\begin{aligned} E_r(r) &= \frac{\lambda}{2\pi\epsilon_0} \frac{1}{r} \quad r \geq a, \\ E_r(r) &= \frac{\lambda}{2\pi\epsilon_0} \frac{r}{a^2} \quad r \leq a. \end{aligned} \tag{5}$$

Note the minus sign in the definition of the linear charge density! Therefore, the potential $U(r)$ is negative and the electric field E_r is directed to the beam center. The potential depth, i.e. the absolute value of the beam potential is maximal at the beam center $r = 0$,

$$U(0) = \frac{\lambda}{2\pi\epsilon_0} \left[\frac{1}{2} + \ln\left(\frac{r_c}{a}\right) \right]. \tag{6}$$

Thus, the local depth of the beam potential depends on the ratio of the beam pipe radius r_c and the beam radius a. The absolute value of the electric field is maximal at the beam edge $r = a$,

$$E_r(a) = \frac{\lambda}{2\pi\epsilon_0} \frac{1}{a}. \tag{7}$$

3.2 Potential well and electric field of a beam with a bi-Gaussian charge distribution

For a bi-Gaussian distribution of the beam particles with the rms values σ_x and σ_y and a round beam pipe with inner radius r_c, the potential U(x,y) can be calculated using the equations in the appendix of Zhou's PhD thesis [17]. We are only interested in the values $U(s)$ at the beam center $(x, y, s) = (0, 0, s)$ which can be calculated using

$$U(s) = U(0,0,s) = \frac{\lambda}{4\pi\epsilon_0} \left[\gamma + \ln\left(\frac{2\, r_c^2}{(\sigma_x + \sigma_y)^2} \right) \right], \tag{8}$$

where $\gamma \approx 0.577$ is Euler's constant. The profile[2] of the beam pipe radius r_c is shown in Fig. 5. The resulting values shown in Fig. 6 are calculated assuming the standard optics, $p_{\bar{p}} = 15$ GeV/c

[2] If the electron cooler is installed the radius r_c amounts to 100 mm in the region of the electron cooler.

and $N_{\bar{p}} = 1.0 \cdot 10^{11}$ and a continuous inner beam pipe radius of 44.5 mm outside of the PANDA target region (see Fig. 5). The potential distribution has minima at positions where the beam has sharp waists (more precisely where the ratio $r_c/(\sigma_x + \sigma_y)$ has a local maximum). The positive ions are accelerated in the longitudinal direction towards those potential minima which act as trapping pockets. These are the ideal locations for the clearing electrodes.

The magnitude of the potential $U(x, y, s)$ and the potential depth $U(s)$ depend on the number $N_{\bar{p}}$ of stored antiprotons. Since $\lambda \propto N_{\bar{p}}$ we get $U(s) \propto N_{\bar{p}}$ if the dependence of $(\sigma_x + \sigma_y)$ on $N_{\bar{p}}$ in the logarithmic term in Eq. (8) is ignored. Thus for $N_{\bar{p}} = 1.0 \cdot 10^{10}$, the potential depth $U(s)$ is a factor of ten lesser. Taking the dependence of $(\sigma_x + \sigma_y)$ on $N_{\bar{p}}$ ($\sigma_{x,y} \propto N_{\bar{p}}^{2/5}$, see Sect. 2.) in the logarithmic term into account yields a reduction factor of about eight.

For a bi-Gaussian distribution of beam particles with σ_x and σ_y and a round beam pipe with inner radius r_c the electric field distribution can be calculated using the complex error function $W(z)$ [32],

$$E_x = \frac{\lambda}{2\,\epsilon_0} \frac{1}{\sqrt{2\pi(\sigma_x^2 - \sigma_y^2)}} \Im \left[W\left(\frac{x + iy}{\sqrt{2(\sigma_x^2 - \sigma_y^2)}} \right) - e^{-\frac{1}{2}\left(\frac{x^2}{\sigma_x^2} + \frac{y^2}{\sigma_y^2}\right)} W\left(\frac{x\frac{\sigma_y}{\sigma_x} + iy\frac{\sigma_x}{\sigma_y}}{\sqrt{2(\sigma_x^2 - \sigma_y^2)}} \right) \right], \quad (9)$$

$$E_y = \frac{\lambda}{2\,\epsilon_0} \frac{1}{\sqrt{2\pi(\sigma_x^2 - \sigma_y^2)}} \Re \left[W\left(\frac{x + iy}{\sqrt{2(\sigma_x^2 - \sigma_y^2)}} \right) - e^{-\frac{1}{2}\left(\frac{x^2}{\sigma_x^2} + \frac{y^2}{\sigma_y^2}\right)} W\left(\frac{x\frac{\sigma_y}{\sigma_x} + iy\frac{\sigma_x}{\sigma_y}}{\sqrt{2(\sigma_x^2 - \sigma_y^2)}} \right) \right]. \quad (10)$$

Here, the symbols $\Re[...]$ and $\Im[...]$ denote the real and imaginary part of the analytical expression $[...]$, respectively.

The transverse electric field near the beam center, which is needed in order to estimate the oscillation frequency of the trapped ions, can be calculated using the following linear approximation

$$E_x(x, y) = \frac{\lambda}{2\pi\epsilon_0} \frac{1}{(\sigma_x + \sigma_y)} \frac{x}{\sigma_x}, \quad (11)$$

$$E_y(x, y) = \frac{\lambda}{2\pi\epsilon_0} \frac{1}{(\sigma_x + \sigma_y)} \frac{y}{\sigma_y}. \quad (12)$$

The transverse electric field components E_r, E_x and E_y of a round Gaussian beam with $\sigma_x = \sigma_y = \sigma_r$ can be evaluated quite simply using

$$E_r(r) = \frac{\lambda}{2\pi\epsilon_0} \left(1 - \exp - \frac{r^2}{2\sigma_r^2} \right) \frac{1}{r}, \quad (13)$$

$$E_x(x, y) = \frac{\lambda}{2\pi\epsilon_0} \left(1 - \exp - \frac{x^2 + y^2}{2\sigma_r^2} \right) \frac{x}{x^2 + y^2}, \quad (14)$$

$$E_y(x, y) = \frac{\lambda}{2\pi\epsilon_0} \left(1 - \exp - \frac{x^2 + y^2}{2\sigma_r^2} \right) \frac{y}{x^2 + y^2}. \quad (15)$$

3.3 Maximum transverse electric field

The absolute value of the transverse electric field is maximal on the short axis of the elliptical beam distribution. For instance if $\sigma_y < \sigma_x$, the maximum is near $y = 1.6\sigma_y$ and can be calculated using Eqs. (9) and (10). The electric fields of the clearing electrodes should be essentially larger than the maximum values of the transverse electric field in order to extract the positive ions out of the beam. Therefore we calculate a safe upper limit E_{max} of the transverse electric field distribution using the following simple formula

$$E_{max} = \frac{|\lambda|}{2\pi\epsilon_0} \frac{1}{\sqrt{2}\sqrt{\sigma_x^2 + \sigma_y^2}}. \tag{16}$$

This equation holds true for the maximal transverse electric field component $|E_{y,max}|$ if $\sigma_y < \sigma_x$ and for the maximal transverse electric field component $|E_{x,max}|$ if $\sigma_x < \sigma_y$. The resulting values E_{max} shown in Fig. 7 are calculated assuming the standard optics, $p_{\bar{p}} = 15$ GeV/c and $N_{\bar{p}} = 1.0 \cdot 10^{11}$. If positive ions are trapped within the negative antiproton beam the potentials and the electric fields are reduced by the factor $(1 - \eta)$ where η is the neutralization factor.

If the electron cooler is installed the effects of the electron beam have to be taken into account. The resulting modifications are discussed in Sect. 16..

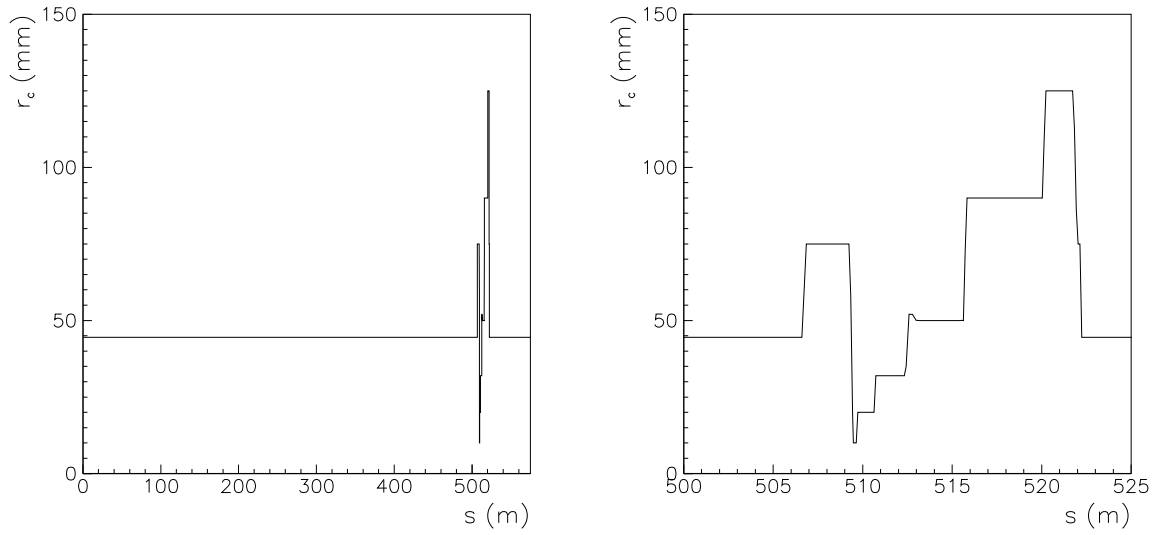

Fig. 5: Inner beam pipe radius $r_c(s)$ (without electron cooler). Left: the complete HESR ring from $s = 0$ m to $s = 575$ m. Right: the PANDA target region from $s = 500$ m to $s = 525$ m. The PANDA target is located at $s = 509.481$ m.

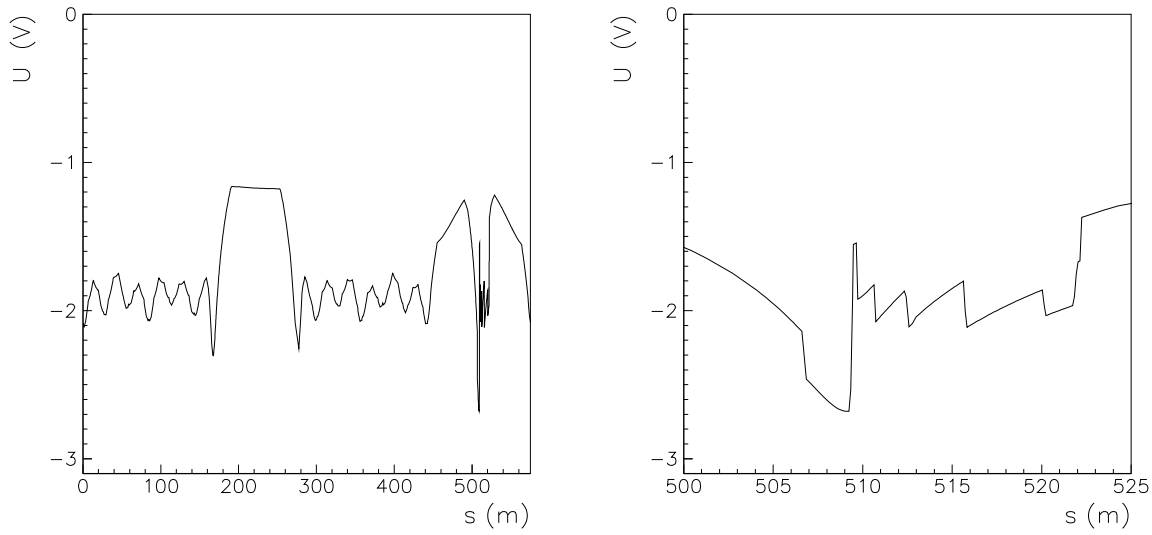

Fig. 6: Central beam potential $U(s)$ assuming the standard optics, $L_1 = 0.9C$, $p_{\bar{p}} = 15$ GeV/c, $N_{\bar{p}} = 1.0 \cdot 10^{11}$ and $\eta = 0$. Left: the complete HESR ring from $s = 0$ m to $s = 575$ m. Right: the PANDA target region from $s = 500$ m to $s = 525$ m.

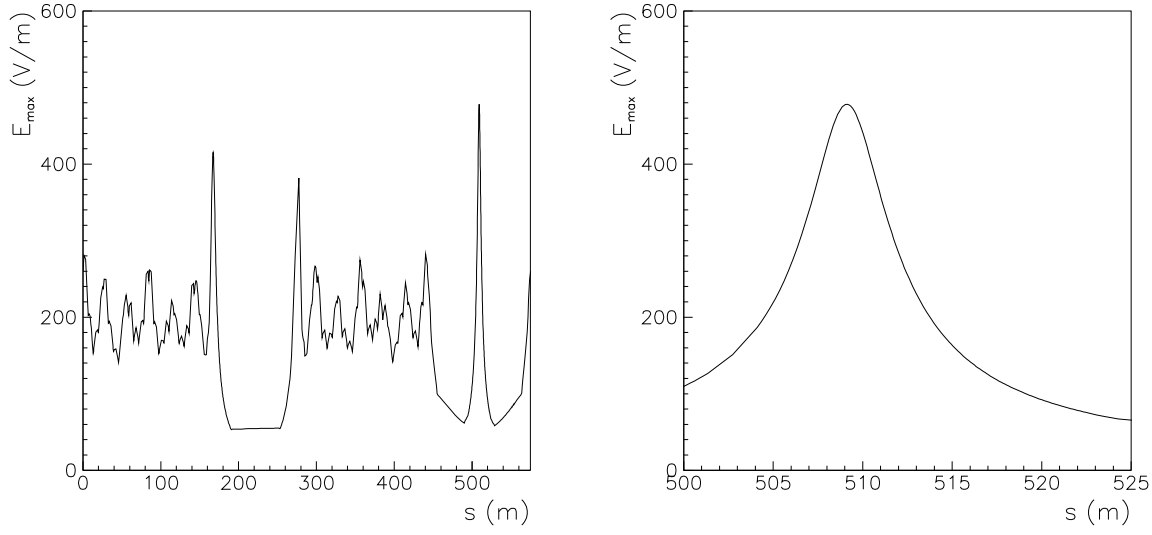

Fig. 7: Upper limit E_{max} of the transverse electric field distribution of the antiproton beam assuming the standard optics, $L_1 = 0.9C$, $p_{\bar{p}} = 15$ GeV/c, $N_{\bar{p}} = 1.0 \cdot 10^{11}$ and $\eta = 0$. Left: the complete HESR ring from $s = 0$ m to $s = 575$ m. Right: the PANDA target region from $s = 500$ m to $s = 525$ m.

3.4 Longitudinal electric field components E_s

It is important to study the longitudinal electric field components E_s of the antiproton beam. In drift spaces (and solenoids) the produced ions are accelerated in the longitudinal direction by those field components towards the potential minima. Knowing the central potential $U(s)$ in fine steps s_i one can deduce numerically the longitudinal electric field component E_s,

$$E_s = -\frac{U_{i+1} - U_i}{s_{i+1} - s_i}. \tag{17}$$

The resulting longitudinal electric field along the beam axis is shown in Fig. 8. The longitudinal field E_s is directed in the positive or negative direction depending on the local gradient of the central potential. The zero crossings mark the positions of maxima and minima of the beam potential $U(s)$. The longitudinal electric field components vary on the average between a few mV/m and about 100 mV/m. The peak-like structures near the PANDA target are due to sudden changes of the inner radius of the beam pipe which are listed in the following list.

1. Between $s = 506.606$ m and $s = 506.856$ m, the inner radius increases from 44.5 mm to 75 mm within 0.25 m yielding a longitudinal field excursion of up to +1.29 V/m which is large and has the same sign as the preceding longitudinal field of about +0.12 V/m.
2. Between $s = 509.231$ m and $s = 509.481$ m, the inner radius decreases from 75 mm to 10 mm within 0.25 m yielding a longitudinal field excursion of up to -7.5 V/m which is very large and has an opposite sign compared to the preceding longitudinal field values of about +0.01 V/m.
3. Between $s = 509.631$ m and $s = 509.731$ m, the inner radius increases from 10 mm to 20 mm within 0.10 m yielding a longitudinal field excursion of +3.79 V/m with an opposite sign with respect to the neighbouring field values of about -0.13 V/m.
4. Between $s = 510.631$ m and $s = 510.731$ m, the inner radius increases from 20 mm to 32 mm within 0.10 m yielding a longitudinal field excursion of +2.48 V/m with an opposite sign with respect to the neighbouring field values of about -0.13 V/m.
5. Between $s = 512.331$ m and $s = 512.581$ m, the inner radius increases from 32 mm to 52 mm within 0.25 m yielding a longitudinal field excursion of up to +1.35 V/m again with an opposite sign with respect to the neighbouring field values of about -0.12 V/m.
6. Between $s = 512.781$ m and $s = 513.181$ m, the inner radius decreases from 52 mm to 50 mm within 0.40 m yielding a longitudinal field excursion of up to -0.22 V/m in the same direction as the neighbouring field values of about -0.11 V/m.
7. Between $s = 515.631$ m and $s = 515.831$ m, the inner radius increases from 50 mm to 90 mm within 0.20 m yielding a longitudinal field excursion of up to +2.02 V/m with an opposite sign with respect to the neighbouring field values of about -0.08 V/m.
8. Between $s = 520.031$ m and $s = 520.231$ m, the inner radius increases from 90 mm to 125 mm within 0.20 m yielding a longitudinal field excursion of up to +1.01 V/m with an opposite sign with respect to the neighbouring field values of about -0.048 V/m.
9. Between $s = 521.731$ m and $s = 522.031$ m, the inner radius decreases from 125 mm to 75 mm within 0.30 m yielding a longitudinal field excursion of up to -1.52 V/m in the same direction as the neighbouring field values of about -0.0428 V/m.
10. Between $s = 522.131$ m and $s = 522.231$ m, the inner radius decreases from 75 mm to 44.5 mm within 0.10 m yielding a longitudinal field excursion of up to -2.94 V/m in the same direction as the neighbouring field values of about -0.042 V/m.

The longitudinal electric field components can be used in order to accelerate trapped ions towards clearing electrodes. This is possible in the region of straight sections which consist of drift spaces, quadrupole magnets, sextupole magnets and solenoids. However, it is not possible to use this effect in the region of dipole magnets. There, the ions gyrate around the magnetic field lines. Finally, we note that the longitudinal electric field components E_s depend strongly on the number $N_{\bar{p}}$ of stored antiprotons. For $N_{\bar{p}} = 1.0 \cdot 10^{10}$, the potential depths and therewith the field components E_s decrease by about a factor of eight, see discussion at the end of Subsect. 3.1.

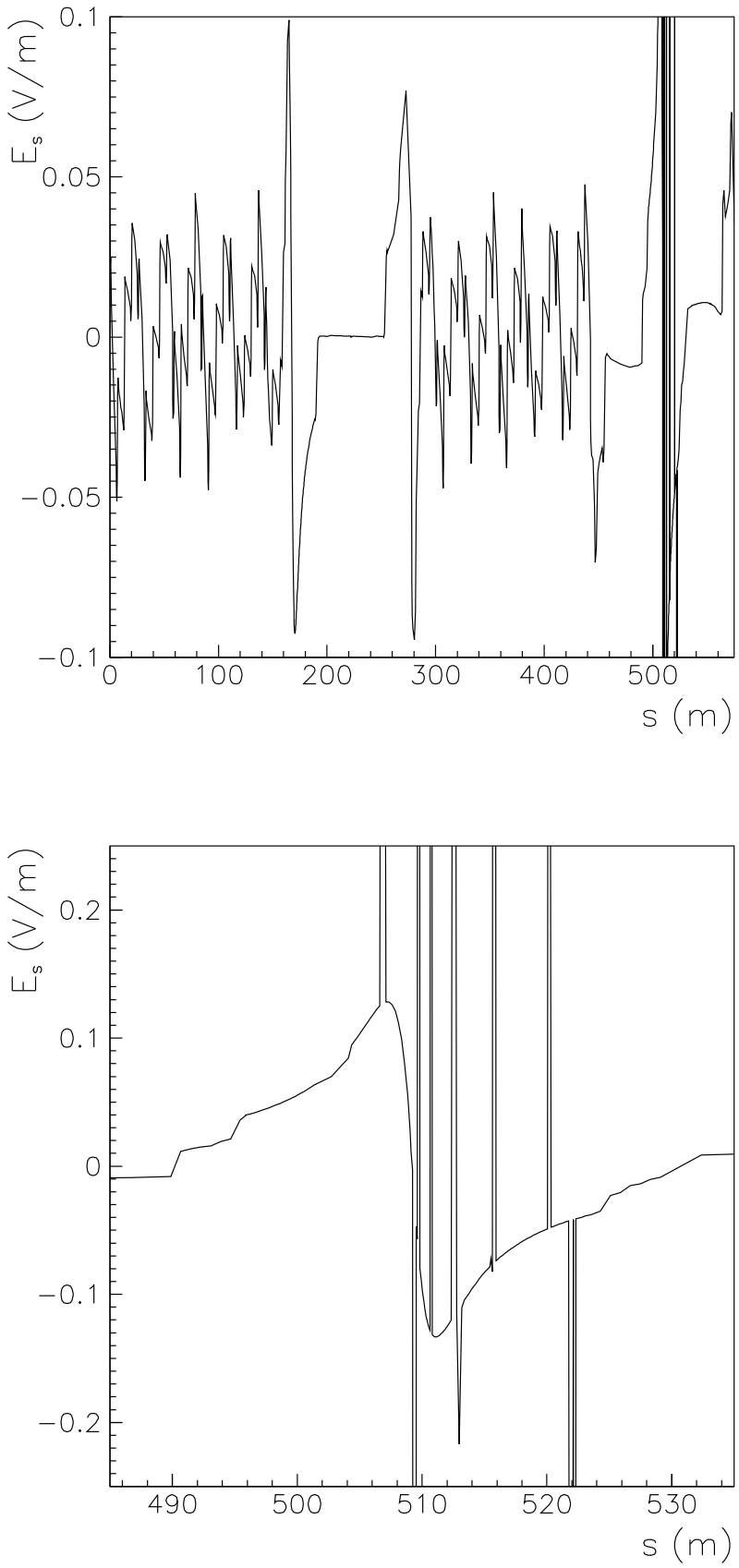

Fig. 8: Longitudinal electric field component E_s of the antiproton beam assuming the standard optics, $L_1 = 0.9C$, $p_{\bar{p}} = 15$ GeV/c and $N_{\bar{p}} = 1.0 \cdot 10^{11}$.The modification of the beam potential by the neutralization η is neglected. Top: the complete HESR ring from $s = 0$ m to $s = 575$ m. Bottom: the PANDA target region from $s = 485$ m to $s = 535$ m. The peak-like structures near the PANDA target are due to sudden changes of the inner radius of the beam pipe.

4. UHV Update

In order to cure the adverse effects of trapped ions in the region of the dipole magnets an especially high UHV vacuum is needed in the region of the arcs. The original design value of the UHV pressure was $\leq 1.0 \cdot 10^{-9}$ mbar. Now, it is planned to improve the UHV vacuum substantially in the North and Sout arc [23]. This can be achieved by sputtering thin-film NEG[3] coatings onto the surface of the vacuum chamber and by using heating jackets along the beam tubes. The aim is to achieve residual gas pressures of about $1.0 \cdot 10^{-11}$ mbar in the North and South arc, see Fig. 9.

Outside the arcs and the PANDA target region the UHV vacuum pressure amounts to $\leq 1.0 \cdot 10^{-9}$ mbar which can be achieved without heating the beam pipes. Nevertheless, it is recommended to install bake-out jackets everywhere outside the PANDA target region. The baked UHV vacuum system at the CERN Antiproton Accelerator was operated at pressures of about $1.3 \cdot 10^{-11}$ mbar.

In the region of the PANDA target the pressure rises up to about $6 \cdot 10^{-5}$ mbar if the pellet target is used [24, 25]. The target is located at $s = 509.481$ m. The pressure as a function of the position s in the ring is shown in Fig. 9. The residual gas contains mainly H_2 molecules. Therefore, the beam neutralization by trapped ions is dominated by H_2^+ ions. The interaction of the beam with trapped H_2^+ ions yields also a certain amount of trapped H^+ ions in the beam. In addition, there are always heavier ions, especially CO^+ ions present. The CO molecules in the residual gas of the UHV are produced by surface processes near gauges and pumps. Surface hydroxides are reduced by hot electrons or ions (in gauges and ion pumps) and liberate oxygen which combines with carbon on surfaces (which is always there also) [26].

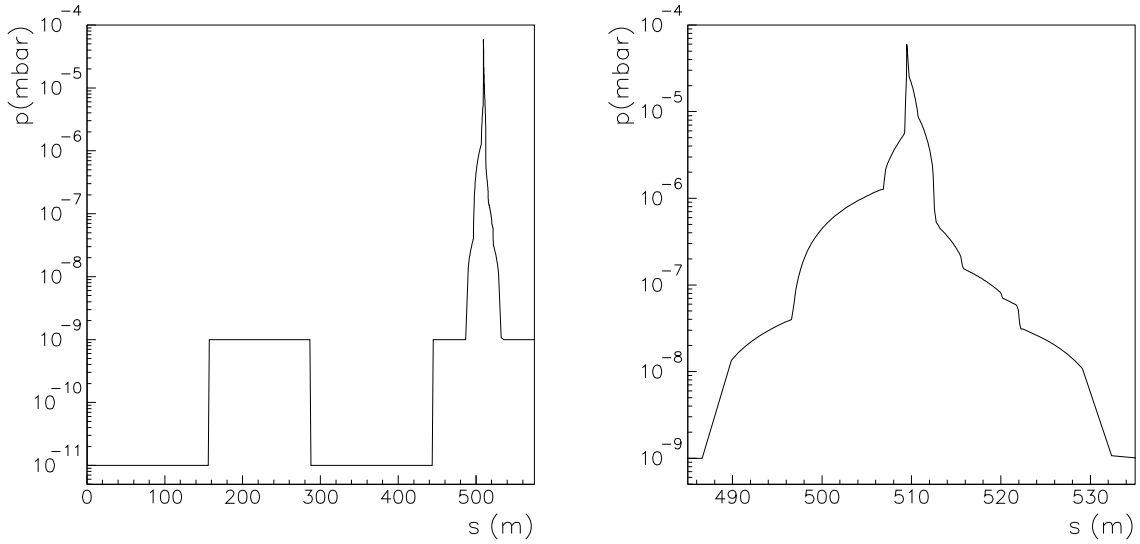

Fig. 9: Vacuum pressure $p(s)$. Left: Complete HESR ring from $s = 0$ m to $s = 575$ m with $p \leq 1.0 \cdot 10^{-9}$ mbar outside of the PANDA target region and with $p = 1.0 \cdot 10^{-11}$ mbar in the region of the North and South arc. Right: PANDA target region from $s = 485$ m to $s = 535$ m. The PANDA target is located at $s = 509.481$ m.

[3]Non-Evaporating Getter Material

5. The Ionization Process

5.1 Energy transfer

The circulating antiprotons interact with the electrons of the residual gas molecules. The differential cross section for an ionization process with an energy transfer between E and $E + \mathrm{d}E$ may be written

$$\frac{\mathrm{d}\sigma}{\mathrm{d}E} = 2\,\pi \frac{m_e c^2}{\beta^2} r_e^2 \frac{Z}{A} \left(1 \,-\, \beta^2 \frac{E}{E_{max}}\right) \frac{1}{E^2}. \tag{18}$$

Here, Z/A refers to the residual gas molecule. The constants are the electron mass, $m_e c^2 = 0.511$ MeV, the classical electron radius, $r_e = 2.818 \cdot 10^{-13}$ cm and the maximum energy transfer E_{max},

$$E_{max} = \frac{2\,m_e c^2 \beta^2 \gamma^2}{1 + 2\,\gamma (m_e/m) + (m_e/m)^2}. \tag{19}$$

Here, m_e is the electron mass, m the antiproton mass and β and γ depend on the beam energy. We get for instance for a kinetic energy of 8.0 GeV $\beta = 0.9945$, $\gamma = 9.526$ and $E_{max} = 91.7$ MeV. This numerical example shows that the energy transfer can be very high. But due to the $1/E^2$ dependence of the differential cross section, ionization events occur mainly at rather low transfer energies. It is interesting to evaluate the mean energy transfer $\bar{E}$,

$$\bar{E} = \int_I^{E_{max}} \frac{\mathrm{d}\sigma}{\mathrm{d}E} E \mathrm{d}E \,/\, \int_I^{E_{max}} \frac{\mathrm{d}\sigma}{\mathrm{d}E} \mathrm{d}E. \tag{20}$$

The minimum energy transfer is not zero. It is given by the mean excitation energy I of the residual gas molecule. An ionization occurs only if the energy transferred to the electron is above the ionization potential. Solving (20), we get

$$\bar{E} = I \left(\ln \frac{E_{max}}{I} - \beta^2\right). \tag{21}$$

For H_2 gas molecules I amounts to 19.2 eV. For an antiproton beam of 8.0 GeV kinetic energy and H_2 molecules we get a mean energy transfer to the electron of

$$\bar{E} = 430 \text{ eV}. \tag{22}$$

This example shows that the mean electron energies from ionization processes are much larger than the mean thermal energy of 0.039 eV at 300 K. The corresponding rms velocity amounts to about $1.23 \cdot 10^7$ m/s. Thus, the electrons leave the potential well of the antiproton beam with rather high velocities.

In contrast the energy transfer to the ion is negligibly small. Therefore, the rms velocities of the ions can be estimated using the mean thermal energy of 0.039 eV at 300 K, see Subsection 6..

5.2 Ionization cross section

The ionization cross section σ depends on the molecules in the residual gas and the velocity $\beta = v/c$ of the beam particles. It does not depend on the charge and the mass of the beam particles. Using Bethe's formula it can be described by

$$\sigma = 4\pi \left(\frac{\hbar}{m_e c}\right)^2 \left\{ M^2 \left[\frac{1}{\beta^2} \ln \left(\frac{\beta^2}{1-\beta^2}\right) - 1\right] + \frac{C}{\beta^2} \right\}, \tag{23}$$

where

$$4\pi \left(\frac{\hbar}{m_e c} \right)^2 = 1.874 \cdot 10^{-24}\ \mathrm{m}^2. \tag{24}$$

The other constants are listed in Table 1. The resulting ionization cross sections are listed in Table 2 for different molecules and four beam momenta. The cross sections for CO and N_2 are nearly equal.

Table 1: The constants M^2 and C for the calculation of the ionization cross section.

Molecule	M^2	C	Z	A
H_2	0.695	8.115	2	2
CH_4	4.23	41.85	10	16
H_2O	3.24	32.26	10	18
N_2	3.74	34.84	14	28
CO	3.70	35.14	14	28
O_2	4.20	38.80	16	32
CO_2	5.75	55.92	22	44

Table 2: Ionization cross sections.

$p_{\bar{p}}$ (GeV/c)	$\sigma(H_2)$ (m^2)	$\sigma(CH_4)$ (m^2)	$\sigma(H_2O)$ (m^2)	$\sigma(CO)$ (m^2)	$\sigma(O_2)$ (m^2)
1.500	$2.16 \cdot 10^{-23}$	$1.12 \cdot 10^{-22}$	$8.60 \cdot 10^{-23}$	$9.37 \cdot 10^{-23}$	$1.04 \cdot 10^{-22}$
3.825	$1.87 \cdot 10^{-23}$	$9.88 \cdot 10^{-23}$	$7.61 \cdot 10^{-23}$	$8.35 \cdot 10^{-23}$	$9.27 \cdot 10^{-23}$
8.889	$2.00 \cdot 10^{-23}$	$1.07 \cdot 10^{-22}$	$8.27 \cdot 10^{-23}$	$9.11 \cdot 10^{-23}$	$1.01 \cdot 10^{-22}$
15.000	$2.12 \cdot 10^{-23}$	$1.15 \cdot 10^{-22}$	$8.84 \cdot 10^{-23}$	$9.78 \cdot 10^{-23}$	$1.09 \cdot 10^{-22}$

Finally, we note that the ionization cross sections depend only weakly on the beam velocity in the momentum range 1.5 - 15 GeV/c of the HESR. Therefore, we take in the following the calculated values at 15 GeV/c.

6. Mean Thermal Energy and Mean Thermal Velocity

Since the momentum transfer during the ionization process is negligibly small the mean energy of the ions at the moment of ionization is equal to the mean thermal energy of the molecules,

$$\bar{W}_i = \frac{3}{2}kT. \tag{25}$$

For $T = 300$ K we get $\bar{W}_i = 0.039$ eV. This mean thermal energy of the positive ions is small compared to the typical well depth of the antiproton beam (1 V - 3 V). Therefore, the positive ions can be trapped by the antiproton beam.

The corresponding mean velocities are the rms velocity v_{rms}

$$v_{rms} = \sqrt{\frac{3kT}{m_i}}, \tag{26}$$

and the mean value of the magnitude of the velocities in one direction $\bar{v}_{\parallel}$,

$$\bar{v}_{\parallel} =< |v_x| >=< |v_y| >=< |v_z| >= \sqrt{\frac{2kT}{\pi m_i}}. \tag{27}$$

They are listed in Tab. 3.

Table 3: Mean thermal velocities ($T = 300$ K, $\bar{W}_i = 0.039$ eV).

Particle	A	v_{rms} (m/s)	$\bar{v}_{\parallel}$ (m/s)
e	1/1836	$1.17{\cdot}10^5$	$5.38{\cdot}10^4$
H	1	$2.73{\cdot}10^3$	$1.26{\cdot}10^3$
H_2	2	$1.93{\cdot}10^3$	$8.89{\cdot}10^2$
CH_4	16	$6.81{\cdot}10^2$	$3.14{\cdot}10^2$
H_2O	18	$6.42{\cdot}10^2$	$2.96{\cdot}10^2$
CO/N_2	28	$5.15{\cdot}10^2$	$2.37{\cdot}10^2$
O_2	32	$4.82{\cdot}10^2$	$2.22{\cdot}10^2$
CO_2	44	$4.11{\cdot}10^2$	$1.89{\cdot}10^2$

7. Production Time T_p, Clearing Time T_c and Neutralization η

7.1 Production time T_p

In order to estimate the amount of neutralization we define the production time $T_{p,i}$, the production rate $R_{p,i} = 1/T_{p,i}$, the clearing time $T_{c,i}$ and the clearing rate $R_{c,i} = 1/T_{c,i}$. The index i is refers to the special ion. The production time $T_{p,i}$ refers to the ionization produced by one single antiproton in the beam. It is defined as the time which is needed to neutralize the negative elementary charge of the antiproton. The corresponding production rate $R_{p,i} = 1/T_{p,i}$ of a certain ion species may be written

$$R_{p,i}(s) = \sigma_i \rho_{m,i}(s) \beta c. \tag{28}$$

Here, σ_i is the ionization cross section, $\rho_{m,i}(s)$ the local number of molecules per volume, and βc the beam velocity. The local number density $\rho_{m,i}(s)$ is given by

$$\rho_{m,i}(s) = \frac{\mathrm{d}N_{m,i}(s)}{\mathrm{d}V} = \frac{p_i(s)}{kT}. \tag{29}$$

Here, $p_i(s)$ is the partial pressure, k the Boltzmann constant and T the absolute temperature. With $p_i = 1.0 \cdot 10^{-9}$ mbar = $1.0 \cdot 10^{-7}$ Pa and $T = 293$ K we get for instance

$$\rho_{m,i} = 2.47 \cdot 10^{13}\ \mathrm{m}^{-3}. \tag{30}$$

The resulting production of ions depends on the number $N_{\bar{p}}$ of antiprotons in the ring and the production time $T_{p,i}$

$$\frac{dN_i(s)}{dt} = \frac{N_{\bar{p}}}{T_{p,i}(s)}. \tag{31}$$

We note that the production time $T_{p,i}(s)$ depends on the local partial densities $\rho_{m,i}(s)$ and therewith on the local partial pressures $p_i(s)$.

In Fig. 10 we show the production time $T_p(s)$ of H_2^+ ions assuming that the partial pressure of H_2 molecules is equal to the total pressure, $p_{H_2}(s) = p(s)$. This assumption neglects the contributions from other ions. It yields a rough estimate of $T_p(s)$. The vacuum pressure in the HESR ring outside the PANDA target region will be $p \leq 1 \cdot 10^{-9}$ mbar. In the North and South arc the residual gas pressure is much lower, $p = 1 \cdot 10^{-11}$ mbar. In the PANDA target region the pressure rises up to about $6 \cdot 10^{-5}$ mbar. In order to take this pressure bump into account the pressure profile $p(s)$ near the PANDA target [24, 25] has been taken into account in the calculations. The pressure profile is shown in Fig. 9. In the PANDA target region, the production time has a marked dip with nearly $1 \cdot 10^{-4}$ s at the minimum. In regions with $1 \cdot 10^{-9}$ mbar, the production time amounts to 6.4 s (at 15 GeV/c). In the region of the North and South arc the production time amounts to 640 s.

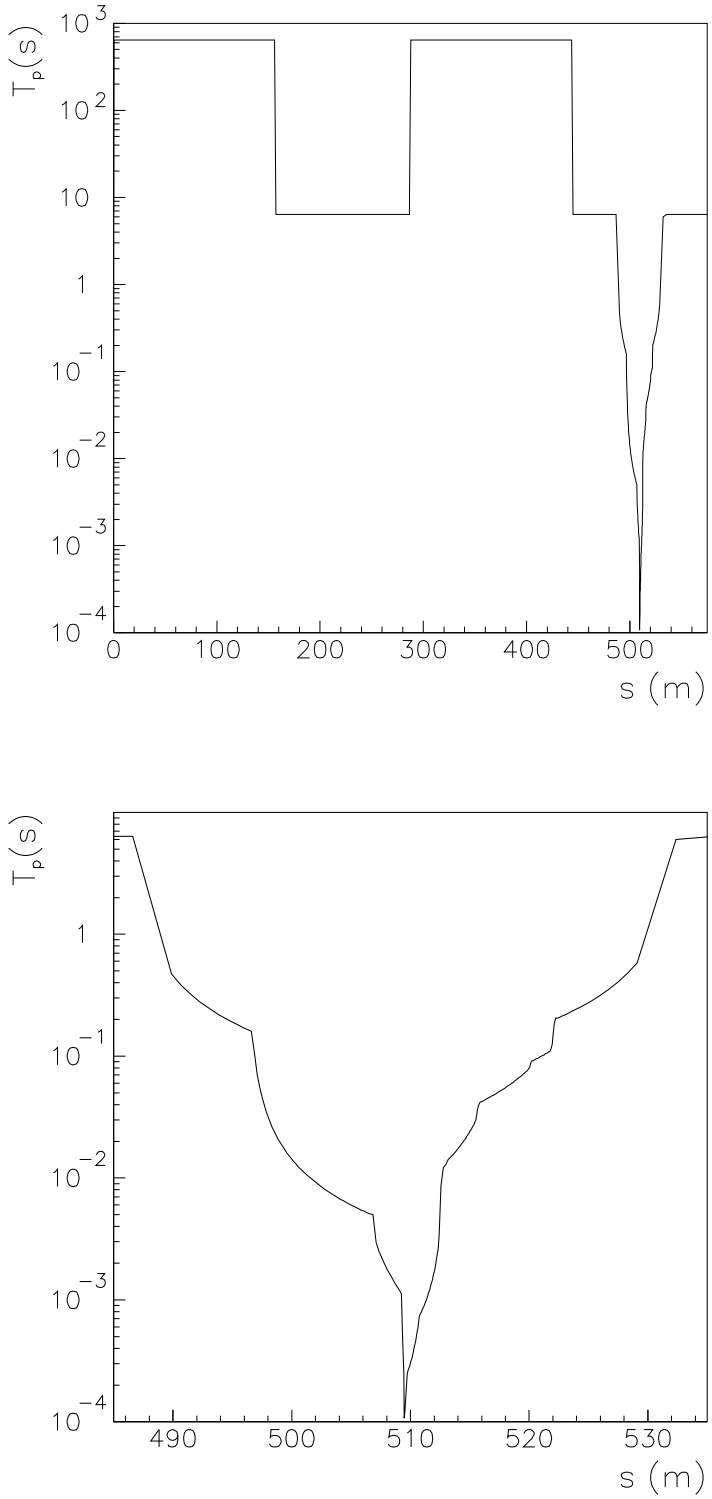

Fig. 10: Production time $T_p(s)$ for H_2^+ ions assuming that the total pressure $p(s)$ is dominated by the partial pressure of H_2 molecules, i.e. $p_i(s) = p(s)$, taking the pressure profile $p(s)$ shown in Fig. 9, and assuming the standard optics, $L_1 = 0.9C$, $p_{\bar{p}} = 15$ GeV/c and $N_{\bar{p}} = 1.0 \cdot 10^{11}$. Top: the complete HESR ring from $s = 0$ m to $s = 575$ m. Bottom: the PANDA target region from $s = 485$ m to $s = 535$ m. The PANDA target is located at $s = 509.481$ m.

7.2 Clearing time T_c

The local clearing time $T_{c,i}(s)$ refers to the mean time which is needed to remove one positive elementary charge of a certain ion i out of the beam. If singly charged ions dominate it is the time needed to remove one single ion. In other words, the clearing time $T_{c,i}(s)$ defines the mean lifetime of the positive ion in the beam. The clearing rate is the inverse of the clearing time,

$$R_{c,i}(s) = \frac{1}{T_{c,i}(s)}. \tag{32}$$

The clearing time depends on the velocity of the ions moving towards the clearing electrodes. Therefore, we need the index i in order to discriminate between H_2^+ ions and heavier ions like for instance CO^+ ions.

In order to illustrate the relation between production time, clearing time and neutralization we consider the neutralization caused by a certain ion species, e.g. H_2^+ ions. To this end, we consider the differential equation of the number of ions N_i in the beam as a function of the time t (again assuming only singly charged ions),

$$\frac{dN_i}{dt} = \frac{N_{\bar{p}}}{T_{p,i}} - \frac{N_i}{T_{c,i}}. \tag{33}$$

The production of ions is proportional to the number of antiprotons. The number of removed ions per second depends on the momentary number of ions N_i in the beam. The solution may be written

$$N_i(t) = N_i(0)\exp(-\frac{t}{T_{c,i}}) + N_{\bar{p}}\frac{T_{c,i}}{T_{p,i}}[1 - \exp(-\frac{t}{T_{c,i}})]. \tag{34}$$

Normally, the number of ions $N_i(0)$ at the beginning is zero and the number of ions in the beam tends asymptotically towards $N_{\bar{p}}T_{c,i}/T_{p,i}$. That means the number of produced ions is equal to the number of cleared ions and we have in the steady state

$$N_i = N_{\bar{p}}\frac{T_{c,i}}{T_{p,i}} = N_{\bar{p}}\frac{R_{p,i}}{R_{c,i}}. \tag{35}$$

This steady state is quickly reached after a few time periods $T_{c,i}$.

7.3 Neutralization η

The resulting local neutralization $\eta_i(s)$ of the beam caused by a certain ion species may be written

$$\eta_i(s) = \frac{L_1}{C}\frac{T_{c,i}(s)}{T_{p,i}(s)} = \frac{L_1}{C}\frac{R_{p,i}(s)}{R_{c,i}(s)}. \tag{36}$$

Thus, the local clearing time $T_{c,i}(s)$ and the local production time $T_{p,i}(s)$ are needed in order to estimate the local neutralization $\eta_i(s)$ caused by a certain ion species. We note that $L_1/C = 0.9$ for the barrier bucket mode of the HESR. Thus, we get $\eta_i(s) = 0.9\,T_{c,i}(s)/T_{p,i}(s)$ for the HESR. Summing all contributions $\eta_i(s)$ yields the total neutralization $\eta(s)$,

$$\eta(s) = \sum \eta_i(s) = \frac{L_1}{C}\sum \frac{T_{c,i}(s)}{T_{p,i}(s)}. \tag{37}$$

8. Ion Motion in Dipole Magnets

8.1 Cyclotron motion of trapped ions in bending magnets

The motion of an ion in the vertical direction along the magnetic field $\vec{B} = (0, B_y, 0)$ of the bending magnets is like in a field-free drift space. Thus, the vertical ion oscillations due to the vertical component E_y of the electric field of the beam are not influenced by the magnet field. In order to extract ions out of the beam one should install clearing electrodes yielding external electric fields in the vertical y-direction.

The motion of the ions in the transverse x- and the longitudinal z-direction is far from being free. An ion with a velocity $v_\perp$ perpendicular to the uniform magnetic field of a bending magnet performs the well known cyclotron motion around the magnetic field lines. The angular frequency ω_i (cyclotron frequency) is given by

$$\omega_i = \frac{q_i B}{m_i}. \tag{38}$$

The radius of the gyration around the magnetic field depends on the velocity v_i perpendicular to the field lines,

$$r_i = \frac{m_i v_i}{q_i B}. \tag{39}$$

In the following Tables we list for some typical magnetic fields B the angular frequency ω_i, the revolution frequency $f_i = \omega_i/(2\pi)$, the revolution time $T_i = 1/f_i$ and the cyclotron radius $r_i = v_i/\omega_i$ for H^+, H_2^+ and CO^+ ions. For v_i, we take the mean thermal velocity in one direction, $\bar{v}_\parallel = \sqrt{2kT/(\pi m_i)}$, with $T = 300$ K (see Table 3). We mention that the cyclotron frequencies f_i of the ions are generally quite high, and the radii r_i for mean thermal velocities $\bar{v}_\parallel$ are very small.

Table 4: Cyclotron motion of thermal $\mathbf{H^+}$ **ions** ($T = 300$ K): magnetic field B, angular frequency ω_i, cyclotron frequency f_i, revolution time T_i, mean radius $\bar{r}_i$.

B (T)	ω_i (s^{-1})	f_i (Hz)	T_i (s)	$\bar{r}_i$ (m)
3.0	$2.87 \cdot 10^8$	$4.57 \cdot 10^7$	$2.19 \cdot 10^{-8}$	$4.37 \cdot 10^{-6}$
2.0	$1.92 \cdot 10^8$	$3.06 \cdot 10^7$	$3.29 \cdot 10^{-8}$	$6.56 \cdot 10^{-6}$
1.7	$1.63 \cdot 10^8$	$2.59 \cdot 10^7$	$3.86 \cdot 10^{-8}$	$7.71 \cdot 10^{-6}$
1.5	$1.44 \cdot 10^8$	$2.29 \cdot 10^7$	$4.37 \cdot 10^{-8}$	$8.74 \cdot 10^{-6}$
0.2	$1.92 \cdot 10^7$	$3.06 \cdot 10^6$	$3.28 \cdot 10^{-7}$	$6.55 \cdot 10^{-5}$
0.17	$1.63 \cdot 10^7$	$2.59 \cdot 10^6$	$3.86 \cdot 10^{-7}$	$7.71 \cdot 10^{-5}$
0.03	$2.87 \cdot 10^6$	$4.57 \cdot 10^5$	$2.19 \cdot 10^{-6}$	$4.37 \cdot 10^{-4}$
0.02	$1.92 \cdot 10^6$	$3.06 \cdot 10^5$	$3.28 \cdot 10^{-6}$	$6.55 \cdot 10^{-4}$
0.01	$0.96 \cdot 10^6$	$1.52 \cdot 10^5$	$6.57 \cdot 10^{-6}$	$1.31 \cdot 10^{-3}$

Table 5: Cyclotron motion of thermal $\mathbf{H}_2^+$ **ions** ($T = 300$ K): magnetic field B, angular frequency ω_i, cyclotron frequency f_i, revolution time T_i, mean radius $\bar{r}_i$.

B (T)	ω_i (s^{-1})	f_i (Hz)	T_i (s)	$\bar{r}_i$ (m)
3.0	$1.44 \cdot 10^8$	$2.29 \cdot 10^7$	$4.37 \cdot 10^{-8}$	$6.18 \cdot 10^{-6}$
2.0	$9.60 \cdot 10^7$	$1.53 \cdot 10^7$	$6.54 \cdot 10^{-8}$	$9.27 \cdot 10^{-6}$
1.7	$8.14 \cdot 10^7$	$1.30 \cdot 10^7$	$7.72 \cdot 10^{-8}$	$1.09 \cdot 10^{-5}$
1.5	$7.18 \cdot 10^7$	$1.14 \cdot 10^7$	$8.75 \cdot 10^{-8}$	$1.24 \cdot 10^{-5}$
0.2	$9.58 \cdot 10^6$	$1.52 \cdot 10^6$	$6.56 \cdot 10^{-7}$	$9.27 \cdot 10^{-5}$
0.17	$8.14 \cdot 10^6$	$1.30 \cdot 10^6$	$7.72 \cdot 10^{-7}$	$1.09 \cdot 10^{-4}$
0.03	$1.44 \cdot 10^6$	$2.29 \cdot 10^5$	$4.37 \cdot 10^{-6}$	$6.18 \cdot 10^{-4}$
0.02	$9.58 \cdot 10^5$	$1.52 \cdot 10^5$	$6.56 \cdot 10^{-6}$	$9.27 \cdot 10^{-4}$
0.01	$4.79 \cdot 10^5$	$7.60 \cdot 10^4$	$1.31 \cdot 10^{-5}$	$1.85 \cdot 10^{-3}$

Table 6: Cyclotron motion of thermal $\mathbf{CO}^+$ **ions** ($T = 300$ K): magnetic field B, angular frequency ω_i, cyclotron frequency f_i, revolution time T_i, mean radius $\bar{r}_i$.

B (T)	ω_i (s^{-1})	f_i (Hz)	T_i (s)	$\bar{r}_i$ (m)
3.0	$1.03 \cdot 10^7$	$1.64 \cdot 10^6$	$6.10 \cdot 10^{-7}$	$2.30 \cdot 10^{-5}$
2.0	$6.91 \cdot 10^6$	$1.10 \cdot 10^6$	$9.08 \cdot 10^{-7}$	$3.46 \cdot 10^{-5}$
1.7	$5.87 \cdot 10^6$	$9.32 \cdot 10^5$	$1.07 \cdot 10^{-6}$	$4.06 \cdot 10^{-5}$
1.5	$5.18 \cdot 10^6$	$8.24 \cdot 10^5$	$1.21 \cdot 10^{-6}$	$4.61 \cdot 10^{-5}$
0.2	$6.91 \cdot 10^5$	$1.10 \cdot 10^5$	$9.08 \cdot 10^{-6}$	$3.45 \cdot 10^{-4}$
0.17	$5.87 \cdot 10^5$	$9.32 \cdot 10^4$	$1.07 \cdot 10^{-5}$	$4.06 \cdot 10^{-4}$
0.03	$1.03 \cdot 10^5$	$1.64 \cdot 10^4$	$6.10 \cdot 10^{-5}$	$2.30 \cdot 10^{-3}$
0.02	$6.91 \cdot 10^4$	$1.10 \cdot 10^4$	$9.08 \cdot 10^{-5}$	$3.45 \cdot 10^{-3}$
0.01	$3.46 \cdot 10^4$	$5.50 \cdot 10^3$	$1.82 \cdot 10^{-4}$	$6.90 \cdot 10^{-3}$

8.2 $\vec{E} \times \vec{B}/B^2$ cross-field drift velocity in dipole magnets

Now, we discuss the combined effect of an electric field $\vec{E}$ and a magnetic field $\vec{B}$, the so-called cross-field drift velocity $\vec{v}_D$. The cross-field drift velocity $\vec{v}_D$ arises, if $\vec{E}$ is perpendicular to $\vec{B}$,

$$\vec{v}_D = \frac{\vec{E} \times \vec{B}}{B^2}. \tag{40}$$

Thus, for an electric field $\vec{E} = (E_x, 0, 0)$ directed in the positive/negative x-direction and a magnetic field in the y-direction, $\vec{B} = (0, B_y, 0)$, the cross-field drift velocity $\vec{v}_D$ is directed into the positive/negative z-direction and amounts to

$$v_z = \frac{E_x}{B_y}. \tag{41}$$

The illustrative explanation of the cross-field drift velocity is shown in Fig. 11. An ion created

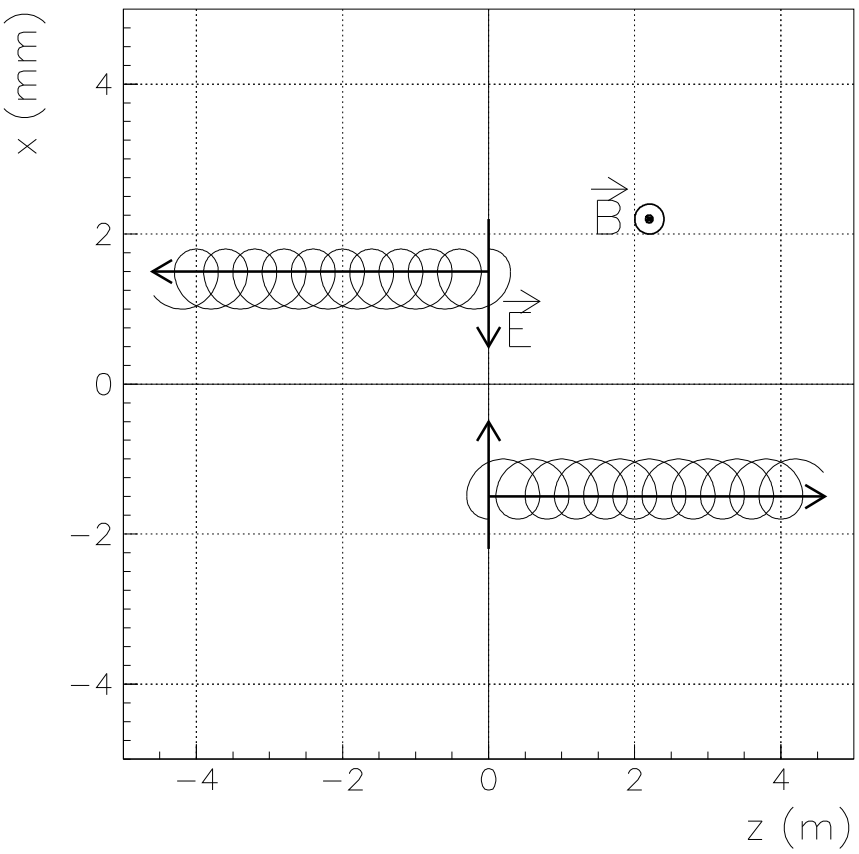

Fig. 11: Illustrative explanation of the cross-field ($\vec{E} \times \vec{B}$) drift velocity $\vec{v}_D$ of a positive ion.

with the start velocity $v_\perp$ moves on a cyclotron-like trajectory around the magnetic field lines. During the time where the ion moves in the direction of the electric field E_x it is accelerated and the radius of it's trajectory is increased. During the time where the ion moves against the direction of the electric field it is decelerated and the radius of it's trajectory is decreased. As a consequence, a mean drift velocity $\vec{v}_D$ perpendicular to the $\vec{B}$- and $\vec{E}$ fields arises. The cross-field drift velocity $\vec{v}_D$ is independent of the start velocity $v_\perp$, the charge q_i, the sign of the charge q_i and the mass m_i of the ion. Thus, ions (of whatever mass and charge) and electrons move in the same direction at the same velocity $\vec{v}_D$.

We note that the electric field $E_x(x)$ is not constant. Near the beam axis E_x depends linearly on x, $E_x = \frac{\lambda}{2\,\pi\epsilon_0}\frac{1}{\sigma_x+\sigma_y}\frac{x}{\sigma_x}$. Therefore, Eq. (41) only applies if the variation of the electric field E_x over the cyclotron motion is small, i.e. if

$$|r_i \partial E_x/\partial x| \ll |E_x(x)|. \tag{42}$$

This condition is fulfilled if the Larmor radius r_i of the ions is very small and if the ions are created at a certain distance x from the central axis with

$$|x| \gg r_i. \tag{43}$$

For instance, the Larmor radius of H_2^+ ions at $B_y = 1.7$ T amounts to about 11 μm, see Table 5. Thus, one can apply Eq. (41) for transverse distances x with $|x| \gg 11$ μm.

The cross-field drift velocities due to the electric field components E_x of the antiproton beam are largest near the edge of the beam. The absolute value of the electric field component $|E_x|$ of a bi-Gaussian beam distribution with $\sigma_x \approx \sigma_y$ has a maximum at $|x| = 1.585\,\sigma_x$. For $\lambda/(2\pi\epsilon_0) = -0.556$ V ($1.0 \cdot 10^{11}$ antiprotons) and $\sigma_x = 1.5$ mm at 15 GeV/c we get $|E_x| = 167$ V/m. This yields with $B_y = 1.7$ T

$$|v_D| \approx 98 \text{ m/s}. \tag{44}$$

We note that the cross-field drift velocity along the beam is in opposite directions on either side of the central beam axis. On the right side it is directed in the forward direction, on the left side in the backward direction. The electric field components E_x and therewith the drift velocities fall to very low values for ions born near the center of the beam. They are even zero at the beam center. Therefore, high ion concentrations and high neutralization levels can exist in bending magnets, if only the mean cross-field drift velocity (see Subsect. 8.3) is used in order to extract the ions in the longitudinal direction.

There is another cross-field drift velocity component $v_x = E_s/B_y$ due to the longitudinal electric field E_s of the beam (see Fig. 8). It is directed in the transverse x-direction. In dipole magnets, the longitudinal electric field components E_s together with the transverse magnetic field component B_y yield drift velocities $v_x = E_s/B_y$ which are much too small to extract the ions in the transverse x-direction. We get for a typical longitudinal electric field of about 0.01 V/m $|v_x| = 0.006$ m/s at 15 GeV/c.

Magnetic mirror effects occur for ions drifting from field-free regions towards the fringe field of magnets. The longitudinal gradient of the magnetic field can reverse the ion motion thus creating a barrier. Therefore, it is also important to install clearing electrodes in the field-free sections between the magnets.

8.3 Estimate of the mean cross-field drift velocity in dipole magnets

Here, we evaluate the mean cross-field drift velocities $\bar{v}_D$ in dipole magnets for $x > 0$, i.e. for ions created on the left side of the beam axis and drifting in the backward direction. Ions created on the right side of the beam axis drift in the forward direction. They experience the same mean cross-field drift velocity in opposite direction, i.e. $\bar{v}_D(x \le 0) = -\bar{v}_D(x \ge 0)$. We assume bi-Gaussian beam distributions with $\sigma_x = \sigma_y = \sigma$ in the region of the dipole magnets. The transverse electric field E_x due to the beam charge is given by

$$E_x(x,y) = \frac{\lambda}{2\pi\epsilon_0}\left(1 - \exp -\frac{x^2+y^2}{2\sigma^2}\right)\frac{x}{x^2+y^2} \tag{45}$$

with $\lambda/(2\pi\epsilon_0) = -0.556$ V for $1.0 \cdot 10^{11}$ antiprotons. The absolute value of E_x is zero at the beam center and rises linearly for small x. It has a maximum near $x = 1.585\,\sigma$, $y = 0$. The normalized transverse beam distribution function $f(x,y)$ is given by

$$f(x,y) = \frac{1}{2\pi\sigma^2}\exp -\frac{x^2+y^2}{2\sigma^2}. \tag{46}$$

The mean value $\bar{E}_x$ of the electric field components $E_x(x,y)$ on the left side of the beam distribution, i.e. for $x \ge 0$, is obtained by folding $E_x(x,y)$ with $f(x,y)$,

$$\bar{E}_x = \frac{\int_{-\infty}^{+\infty}\int_{0}^{+\infty} E_x(x,y) f(x,y)\mathrm{d}x\mathrm{d}y}{\int_{-\infty}^{+\infty}\int_{0}^{+\infty} f(x,y)\mathrm{d}x\mathrm{d}y}. \tag{47}$$

The folding can be done analytically. It yields the mean value $\bar{E}_x$,

$$\bar{E}_x = \frac{\lambda}{2\pi\epsilon_0} \frac{1}{\sqrt{2\pi}\sigma} \frac{2-\sqrt{2}}{\pi}. \tag{48}$$

The absolute value of the mean drift velocity $|\bar{v}_D|$ in longitudinal direction reads

$$|\bar{v}_D| = \frac{|\bar{E}_x|}{B_y}. \tag{49}$$

The length L of the dipole magnets amounts to 4.2 m. Now, we assume that the ions are captured by clearing electrodes with clearing fields E_y at the entrance and exit of a dipole magnet. We assume that the clearing electrodes are located outside of the dipole magnets and that the distance between them amounts to about 4.5 m. Thus, the mean drift distance is $L/2 = 2.25$ m and the mean clearing time T_c is given by

$$T_c = \frac{L}{2|\bar{v}_D|}. \tag{50}$$

This equation holds true for ions created at $x \geq 0$ as well as $x \leq 0$. We note that the beam width σ scales like $1/\sqrt{p}$ according to the adiabatic damping law with $\sigma \approx 1.5$ mm at 15 GeV/c. This scaling is taken into account in the evaluation of $\bar{E}_x$. The transverse magnetic field B_y scales linearly with the beam momentum p. In Table 7, we list the mean cross-field drift velocity $|\bar{v}_D|$ and the mean clearing time T_c for $L/2 = 2.25$ m. We recall that the cross-field drift velocity does not depend on the mass and charge of the ions. Thus, CO^+ ions experience the same drift velocity as H_2^+ ions.

Table 7: Mean cross-field drift velocity $|\bar{v}_D|$ and mean clearing time T_c for $1.0 \cdot 10^{11}$ antiprotons and $L = 4.5$ m.

p GeV/c	$\lvert\bar{v}_D\rvert$ (m/s)	T_c (s)
1.5	51.3	0.0439
3.825	32.1	0.0701
8.889	21.1	0.107
15.0	16.2	0.139

The mean cross-field drift velocities $|\bar{v}_D|$ are rather small. This is due to the fact that the electric field E_x and therewith the cross-field drift velocity v_D drops down to zero at the beam center. Therefore, ions created near the beam center are practically not cleared and the resulting mean cross-field drift velocities are rather low in dipole magnets when averaged over the Gaussian beam profile. As a consequence, the resulting clearing times T_c are rather high.

In addition, the mean electric fields and therewith the mean cross-field drift velocities depend critically on the number $N_{\bar{p}}$ of stored protons. The linear charge density λ is proportional to $N_{\bar{p}}$, and the beam width σ is proportional to $N_{\bar{p}}^{2/5}$ (see Sect. 2.). Therefore, the mean cross-field drift velocity $\bar{v}_D$ is proportional to $N_{\bar{p}}^{3/5}$. Compared to $1.0 \cdot 10^{11}$ antiprotons the mean cross-field drift velocities for $1.0 \cdot 10^{10}$ antiprotons are by a factor of $10^{3/5}$=3.98 lesser and the mean clearing times T_c are by a factor of $10^{3/5}$=3.98 larger, see Table 8.

Table 8: Mean cross-field drift velocity $|\bar{v}_D|$ and mean clearing time T_c for $1.0 \cdot 10^{10}$ antiprotons and $L = 4.5$ m.

p GeV/c	$\|\bar{v}_D\|$ (m/s)	T_c (s)
1.5	12.9	0.175
3.825	8.06	0.279
8.889	5.30	0.426
15.0	4.07	0.553

9. Ion Motion in Solenoids

The ion motion in solenoids has been analyzed in detail in a previous report [1]. Here, we summarize the main results of this study.

A speciality of the HESR ring are solenoids which are used for special purposes. The electron cooler (EC) consists of a long solenoid of about 24.0 m length which guides the electron beam along the axis of the antiproton beam. The solenoid field amounts to 0.2 T yielding a solenoid strength of 4.8 Tm. In addition, there are two compensation solenoids of about 5.0 m length with a maximum solenoid field $B = 1.5$ T and a maximum solenoid strength of 7.5 Tm. They are located upstream and downstream near by the EC solenoid. In the region of the PANDA target the spectrometer magnet consists of a superconducting solenoid with external iron return yoke which allows to achieve a uniform longitudinal field of 2.0 T and to keep enough space for detectors surrounding the interaction point. The maximum solenoid strength is about 7.0 Tm. In addition, there is one compensation solenoid of about 5.0 m length with a maximum solenoid field of 1.5 T and a maximum solenoid strength of 7.5 Tm in front of the target solenoid.

9.1 Cyclotron motion of trapped ions in solenoids

First, we discuss the situation in the beam-free time gaps. An ion which is created inside of a solenoid cannot escape in the transverse direction. The Lorentz force $q_i\vec{v}_i \times \vec{B}$ causes each ion to spiral around a magnetic field line. We assume that the ion has a certain thermal velocity with velocity components perpendicular and parallel to the magnetic field, $v_\perp$ and $v_\parallel$. In the transverse direction (i.e. in the plane perpendicular to the magnetic field direction) the ion performs a cyclotron motion around the magnetic field lines of the solenoid. In the longitudinal direction the ion moves freely along the magnetic field line of its guiding center. The cyclotron frequency ω_i depends on the magnetic field strength B, $\omega_i = q_i B/m_i$. The cyclotron radius r_i depends on the transverse thermal velocity $v_\perp$, $r_i = (m_i v_\perp)/(q_i B)$. Typical values of ω_i and r_i are listed in subsection 8.1 in the Tables 4, 5 and 6.

9.2 Magnetron motion and modified cyclotron motion in solenoids due to the electric field of the beam

The superposition of the radial electric field $\vec{E}$ of the beam and the longitudinal magnetic field $\vec{B}$ yields a modified cyclotron motion and a slow motion around the solenoid axis. The latter motion is due to the $\vec{E} \times \vec{B}$ drift in azimuthal direction. It is called magnetron motion since it has been first observed during the development of the magnetron [36]. This motion has also been analyzed during the development of the Penning traps [37]. The modified cyclotron motion and

the resulting magnetron motion is illustrated in the left panel of Fig. 12. The figure shows the projection of the ion motion upon the (x,y) plane. The cyclotron motion due to the longitudinal magnetic field is modified by the radial acceleration and deceleration. If the ion moves in the direction of the electric field it is accelerated and the radius of the trajectory is increased. If the ion moves against the direction of the electric field it is decelerated and the radius of the trajectory is decreased. As a consequence a mean drift velocity in the azimuthal direction arises. The rotational direction of the magnetron motion (ω_-) is opposite to that of the cyclotron motion. This is due to the fact that the electric field $\vec{E}$ of the antiproton beam is directed radially towards the central axis. The resultant motion can be described by an epicycloid, i.e. the superposition of a slow circular magnetron motion with radius r_- and angular velocity ω_- and a modified cyclotron motion with radius r_+ and angular velocity ω_+, see right panel of Fig. 12. The fast cyclotron motion with a small radius r_+ is carried along by the slow magnetron motion with a large radius r_-.

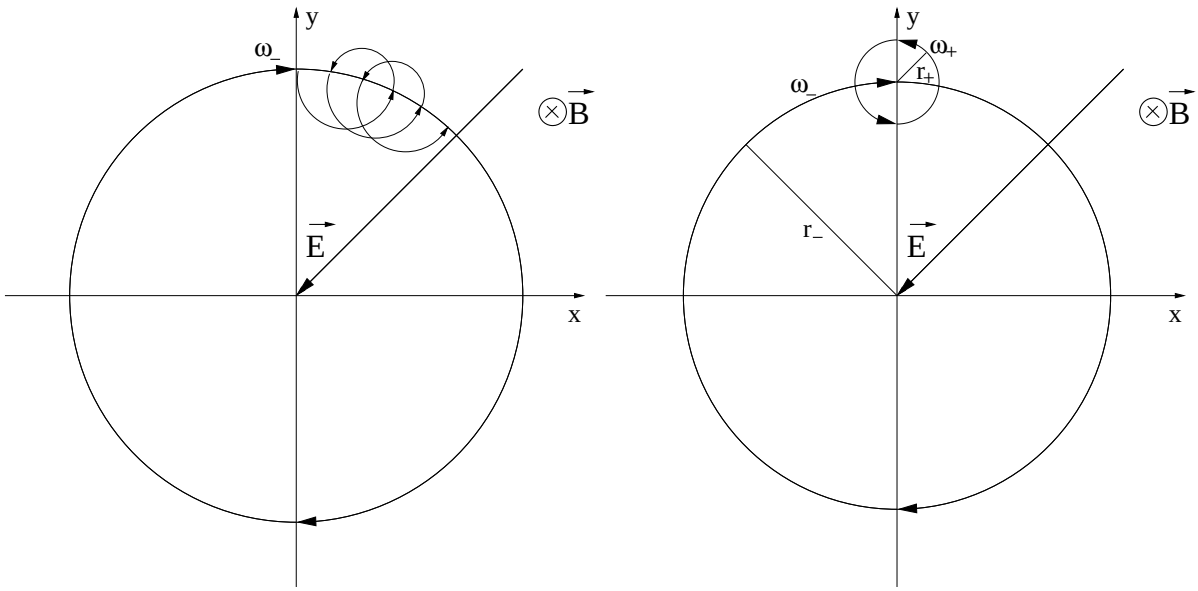

Fig. 12: Left: Illustration of the motion of trapped ions in a solenoid. The cyclotron motion is modified by the acceleration and deceleration due to the electric field $\vec{E}$ of the antiproton beam. The resulting magnetron motion (ω_-) is opposite to the cyclotron motion (ω_+). Right: The motion can be described as an epicycloid that is the superposition of a slow circular magnetron motion with radius r_- and angular velocity ω_- and a modified cyclotron motion with radius r_+ and angular velocity ω_+.

Here, we sketch the solution. We use a Cartesian coordinate system $(x, y.z)$ which corresponds to the standard coordinate system (x, y, s) of accelerator physics. The z-axis is the central axis of the solenoid. The ion motion is described radially by $\vec{\rho} = (x, y)$ and axially by z. The equations of motion read

$$m\ddot{\vec{\rho}} = q(\vec{E}_\rho + \dot{\vec{\rho}} \times \vec{B}), \tag{51}$$

$$m\ddot{z} = qE_z. \tag{52}$$

We assume a linear approximation of the radially attractive electric field

$$\vec{E}_\rho = -E_0\vec{\rho}. \tag{53}$$

We note that $E_0 = |\lambda|/(2\pi\epsilon_0 a^2)$ for a round beam with constant density within the radius a, see Eq. 5. We introduce the angular frequency[4] $\omega_b = \sqrt{qE_0/m}$ in order to take the electric field strength into account,

$$\omega_b^2 = \frac{q}{m}\frac{|\lambda|}{2\pi\epsilon_0}\frac{1}{a^2}. \tag{54}$$

We assume that the magnetic field is oriented in the negative z-direction

$$\vec{B} = -(0, 0, B). \tag{55}$$

The magnetic field strength is represented by the angular frequency $\omega_c = qB/m$ of the free cyclotron motion (i.e. for $\vec{E}_\rho = 0$). The solution of the radial equation (51) may be written

$$\vec{\rho} = \vec{r}_+ + \vec{r}_-, \tag{56}$$

$$\vec{r}_+ = r_+(\cos(\omega_+ t + \alpha_+), \sin(\omega_+ t + \alpha_+)), \tag{57}$$

$$\vec{r}_- = r_-(\cos(\omega_- t + \alpha_-), \sin(\omega_- t + \alpha_-)), \tag{58}$$

where

$$\omega_+ = \frac{\omega_c}{2} + \sqrt{\left(\frac{\omega_c}{2}\right)^2 + \omega_b^2}, \tag{59}$$

$$\omega_- = \frac{\omega_c}{2} - \sqrt{\left(\frac{\omega_c}{2}\right)^2 + \omega_b^2}. \tag{60}$$

The radial motion of an ion is characterized by the superposition of two motions: (i) the modified cyclotron motion with angular frequency ω_+ and radius r_+ and (ii) the magnetron motion with angular frequency ω_- and radius r_-. The angular velocity ω_+ is positive whereas the angular velocity ω_- is negative. This is due to the radially attractive electric potential, see Fig. 12. The parameters r_+, r_-, α_+ and α_- are constants of integration determined by the initial position and velocity of the ion in the moment of ionization.

It is interesting to evaluate the velocity $v_- = r_-\omega_-$ of the magnetron motion. If $\omega_b^2 \ll (\omega_c/2)^2$ we get

$$r_-\,\omega_- = -r_-\,\frac{\omega_b^2}{\omega_c} = -r_-\frac{E_0}{B} = -\frac{|\vec{E}|}{B} = \frac{\vec{E}\times\vec{B}}{B^2}. \tag{61}$$

That means, the velocity v_- of the magnetron motion is given by the $\vec{E}\times\vec{B}$ cross-field velocity.

9.3 Fringe field of solenoids

The inside magnetic field of a long solenoid is nearly uniform. The field strength B_z along the axis may be written

$$B_z(z) = \frac{B_0}{2}\left(\frac{L+z}{\sqrt{(L+z)^2+a^2}} - \frac{z}{\sqrt{z^2+a^2}}\right). \tag{62}$$

Here, $B_0 = \mu_0 N I$ with μ_0 is the magnetic field constant, N the number of windings per meter, I the current, L the length, a the radius of the solenoid coil and z the longitudinal position with

[4] In drift spaces ω_b is the 'bouncing frequency' of a trapped ion

$z = 0$ at the exit of the solenoid. Thus, the extent of the fringe field depends on the radius a. We have for instance $B_z = 0.985\, B_0$ at $z = -4\, a$ and $B_z = 0.015\, B_0$ at $z = +4\, a$.

The PANDA spectrometer solenoid [40] consists of three large coils in a large iron yoke. The inner radius of the coils amounts to 0.930 m and the total coil length amounts to about 2.8 m. The magnetic field distribution has been calculated with the program TOSCA [40]. The solenoid strength amounts to about 7.0 Tm. The longitudinal field distribution along the solenoid axis can be approximated using a trapezoidal model with a minor basis of 1.5 m and a major basis (at zero field) of about 5.5 m. The minor basis, i.e. the central part, exhibits a highly uniform magnetic field $B_0 = 2.0$ T. It is about 1.5 m long. The upstream and downstream fringe fields extend to about $l = 2.0$ m. The magnetic field $B_z(z)$ in the fringe field region $0 \leq |z| \leq l$ can be approximated using

$$B_z(z) \approx B_0 \left(1 - \frac{|z|}{l}\right), \quad 0 \leq |z| \leq l. \tag{63}$$

The total length of the trapezoidal field distribution amounts to about 5.5 m.

The equations (63) - (65) may be used in order to calculate the increasing radii r_+ and r_- of trapped ions at the entrance and exit of the solenoids, see next Subsection.

9.4 Adiabatic motion of trapped ions in the fringe field of solenoids

In the fringe field of the solenoid a slow ion (i.e. the guiding center of the ion) follows adiabatically the expanding field lines. Thus, the cyclotron radius r_i and the distance R_i of the guiding center from the solenoid axis increase according to

$$B_z r_i^2 = const, \quad B_z R_i^2 = const. \tag{64}$$

The last two equations follow directly from Busch's theorem, i.e. the magnetic flux through the cyclotron orbit with radius r_i and the magnetic flux through a circle around the z-axis with radius R_i are conserved. Thus, r_i and R_i increase in the fringe field like

$$r_i(z) = \sqrt{\frac{B_z(z_0)}{B_z(z)}}\, r_i(z_0), \quad R_i(z) = \sqrt{\frac{B_z(z_0)}{B_z(z)}}\, R_i(z_0). \tag{65}$$

Another consequence of the adiabatic motion is the fact that the velocity component $v_\perp$ perpendicular to the field line decreases slowly in the fringe field while the velocity component $v_\parallel$ parallel to the field line increases,

$$v_\perp(z) = \sqrt{\frac{B_z(z)}{B_z(z_0)}}\, v_\perp(z_0), \tag{66}$$

$$v_\parallel(z) = \sqrt{v_0^2 - v_\perp^2(z)}, \tag{67}$$

where $v_0^2 = v_\perp^2 + v_\parallel^2 = const$. The last equation is due to the conservation of kinetic energy.

9.5 Magnetic mirror effect of solenoids

Now, we consider an ion near a solenoid which moves in the direction of increasing longitudinal field $B_z(z)$. The magnetic field component $B_z(z_0)$ at the starting point z_0 is rather low. The

velocity components at the starting point z_0 are denoted by $v_\perp(z_0)$ and $v_\parallel(z_0)$ and the total velocity amounts to $v_0 = \sqrt{v_\perp^2(z_0) + v_\parallel^2(z_0)}$. Now, the velocity component $v_\perp(z)$ perpendicular to the field line increases slowly in the fringe field while the velocity component $v_\parallel(z)$ parallel to the field line decreases, see Eqs. (66) and (67). If the velocity component $v_\perp(z)$ perpendicular to the field line becomes equal to v_0, the velocity component $v_\parallel(z)$ parallel to the field line becomes zero and the motion parallel to the field line is stopped. As a consequence the ion spirals back. The stop occurs if

$$v_0^2 - \frac{B_z(z)}{B_z(z_0)} v_\perp^2(z_0) = 0, \tag{68}$$

i.e. if

$$v_\parallel^2(z_0) + v_\perp^2(z_0) - \frac{B_z(z)}{B_z(z_0)} v_\perp^2(z_0) = 0. \tag{69}$$

That means if

$$\frac{B_z(z)}{B_z(z_0)} = 1 + \frac{v_\parallel^2(z_0)}{v_\perp^2(z_0)}. \tag{70}$$

9.6 Mean thermal ion drift and clearing times T_c in solenoids

In the longitudinal direction, the ions move freely along the magnetic field lines of the solenoids. Here, we estimate the resulting clearing times T_c if the ions are moving with their mean thermal velocity in the longitudinal direction and are captured by clearing electrodes at the entrance and exit of the solenoids. These estimates are only valid if the longitudinal electric fields E_s of the beam are negligibly small. Such a situation occurs for $1.0 \cdot 10^{11}$ antiprotons in the region of the EC-solenoid and the EC-compensation solenoids, see E_s in Fig. 8 between $s = 190$ m and $s = 250$ m. For $1.0 \cdot 10^{10}$ antiprotons, the longitudinal electric field components of the beam are negligibly small everywhere in the ring. The mean thermal velocity in one direction, $\bar{v}_\parallel$, amounts to 889 m/s for H_2^+ ions and 238 m/s for CO^+ ions. We assume as mean path length the half length of a solenoid, i.e. $\bar{l} = L/2 = 12$ m for the electron cooler solenoid and $\bar{l} = L/2 = 2.5$ m for the compensation solenoids The resulting mean clearing times are given by

$$T_c = \bar{l}/\bar{v}_\parallel. \tag{71}$$

They are listed in Table 9 for various molecules.

Table 9: Mean thermal ion drift velocity $\bar{v}_\parallel$ in one direction and clearing times T_c in solenoids.

Molecule	A	$v_\parallel$ (m/s)	T_c (s), EC solenoid	T_c (s), compensation solenoid
H	1	$1.2{\cdot}10^3$	$10{\cdot}10^{-3}$	$2.1{\cdot}10^{-3}$
H_2	2	$8.9{\cdot}10^2$	$13{\cdot}10^{-3}$	$2.8{\cdot}10^{-3}$
CH_4	16	$3.1{\cdot}10^2$	$37{\cdot}10^{-3}$	$7.9{\cdot}10^{-3}$
H_2O	18	$3.0{\cdot}10^2$	$40{\cdot}10^{-3}$	$8.3{\cdot}10^{-3}$
CO/N_2	28	$2.4{\cdot}10^2$	$50{\cdot}10^{-3}$	$10{\cdot}10^{-3}$
CO_2	44	$1.9{\cdot}10^2$	$63{\cdot}10^{-3}$	$13{\cdot}10^{-3}$

10. Clearing Electrodes

10.1 Introductory remarks

The positive ions can be extracted by clearing electrodes if the external electric fields are larger than the electric fields created by the antiproton beam, see Fig. 7. Thus, isolated electrodes near the inner surface of the beam pipe (inner diameter: 89 mm) providing sufficiently large electric fields of more than 500 V/m can be used in order to extract the produced ions. The electrodes of the beam position monitors in the ring can also be used to extract the positive ions out of the antiproton beam. Finally, we mention that the closed orbit distortions by the transverse electric fields of the clearing electrodes are negligibly small.

We differentiate between single isolated clearing electrodes and continuous clearing electrodes extending over several meters. The technology of single isolated clearing electrodes has been described in the literature. Often, clearing electrodes of the button type are used in order to achieve negligible coupling to the beam, i.e. low impedances [20]. Continuous electrodes can be used in regions where extremely high clearing rates are needed. In the neighbourhood of the PANDA target such electrodes are mandatory in order to counteract the high production rates of trapped ions. Continuous clearing electrodes are described in Subsection 10.3.

The number of single isolated clearing electrodes should be as large as possible. Ideal locations are the minima of the beam potential which act as trapping pockets. In the arcs, it is mandatory to locate clearing electrodes at the entrance and exit of the dipole magnets, see Subsection 13.1.

Clearing electrodes can also provide valuable diagnostic information if the clearing current on each electrode can be measured using fast picoamperemeters [17]. For instance such measurements yield a relatively good information about the local production time $T_p(s)$ which depends on the local pressure $p(s)$. Switching on and off of certain clearing electrodes or groups of clearing electrodes allows to study the local effects of trapped ions.

10.2 Clearing rates using single isolated clearing electrodes in straight sections

Here, we estimate the clearing rates R_c and clearing times T_c assuming that the ions move with a mean thermal velocity $\bar{v}_{\|}$ (see Table 3) towards single isolated clearing electrodes. We assume drift spaces with a distance $L = 5$ m between the single isolated electrodes. The resulting mean clearing time T_c can be evaluated using

$$T_c = \frac{L}{2\,\bar{v}_{\|}}. \tag{72}$$

We note that similar estimates are obtained if one takes the longitudinal acceleration $a_s = qE_s/m$ due to the longitudinal electric field components of the beam into account. The resulting beam neutralization $\eta = 0.9\,T_c/T_p$ depends on the production time T_p of the ions. The clearing times T_c, the clearing rates R_c, the production times T_p and the resulting neutralizations η are estimated for H_2^+ and CO^+ ions assuming total pressures of about $1.0 \cdot 10^{-9}$ mbar pressures, see Tables 10 and 11.

Table 10: Mean thermal velocity $|\bar{v}_{\parallel}|$, mean clearing time T_c ($L = 5$ m), production time T_p and neutralization η for H_2^+ ions using single isolated clearing electrodes and assuming a partial H_2 pressure of $0.8 \cdot 10^{-9}$ mbar.

p (GeV/c)	$\|\bar{v}_{\parallel}\|$ (m/s)	T_c (s)	R_c(s^{-1})	T_p (s)	η
1.5	889	0.00281	356	9.22	$2.74 \cdot 10^{-4}$
3.825	889	0.00281	356	9.29	$2.72 \cdot 10^{-4}$
8.889	889	0.00281	356	8.69	$2.91 \cdot 10^{-4}$
15.0	889	0.00281	356	7.98	$3.17 \cdot 10^{-4}$

Table 11: Mean thermal velocity $|\bar{v}_{\parallel}|$, mean clearing time T_c ($L = 5$ m), production time T_p and neutralization η for CO^+ ions using single isolated clearing electrodes and assuming a partial CO pressure of $0.2 \cdot 10^{-9}$ mbar.

p (GeV/c)	$\|\bar{v}_{\parallel}\|$ (m/s)	T_c (s)	R_c(s^{-1})	T_p (s)	η
1.5	237	0.0106	94.3	8.50	$1.12 \cdot 10^{-3}$
3.825	237	0.0106	94.3	8.33	$1.15 \cdot 10^{-3}$
8.889	237	0.0106	94.3	7.45	$1.28 \cdot 10^{-3}$
15.0	237	0.0106	94.3	6.92	$1.38 \cdot 10^{-3}$

10.3 Continuous clearing electrodes

The highest clearing rates can be achieved using continuous clearing electrodes inside the beam pipes. However, long clearing electrodes inside the beam tubes must be compatible with the requirements of the HESR ring. They must have good vacuum properties, little aperture reduction and a low beam coupling impedance. Such clearing electrodes have recently been developed at CERN [28, 29]. We suggest to use this new design at HESR. Similar clearing electrodes for electron cloud mitigation at KEKB positron ring have been developed recently [30].

The continuous electrode consists of a highly resistive layer deposited onto a very thin isolating strip inside the beam pipe, see Fig. 13. In Ref. [28] beam pipes with different inner radii have been studied. We refer to the investigation of the PS beam pipe with an inner radius of 50 mm. This inner radius is comparable to the inner radius of 44.5 mm of the HESR beam pipe. The 0.1 mm thick and about 30 mm wide isolating layer can be made by the application of enamel or by plasma spraying of alumina (Al_2O_3). On top of the isolating layer a 25 mm wide highly resistive thick film coating with a few $10\,\mu\mathrm{m}$ thickness is applied. The length of such an electrode can be a few meters. It can be installed in straight sections and in magnetic dipole sections. The clearing voltage can be applied by feedthroughs at one or both ends of the electrode. Clearing voltages up to -1.0 kV are possible.

The surface resistance $R_{surface}$ of the highly resistive layer must be higher than the free space impedance $Z_0 = 377\ \Omega$ but small enough that the voltage drop along the electrode is not too high. If $R_{surface} \gg Z_0$ the layer is "invisible" to the electromagnetic waves. Therefore values of $R_{surface} = 10$ kΩ to 100 kΩ are recommended. In this context we note that the currents from the ion clearing are very small.

The longitudinal and transverse impedances of the new electrode have been estimated in Ref. [28]. The real part of the longitudinal impedance, $\Re(Z/n)$, is not affected by a thin lossless dielectric. The imaginary part of the longitudinal impedance $\Im(Z/n)$ can be estimated in first order approximation (for a thin dielectric layer inside a round beam pipe extending over the machine circumference)

$$\Im(\frac{Z}{n}) = \sqrt{\frac{\mu_0}{\epsilon_0}} \left(1 - \frac{1}{\epsilon_r}\right) \frac{t}{r_i}. \tag{73}$$

Here, t is the dielectric thickness, r_i the inner radius of the beam pipe and ϵ_r the permittivity ($\epsilon_r = 5$ for enamel). The longitudinal impedance of a single 25 mm wide and 0.1 mm thick high resistive layer inside a beam pipe with inner radius $r_i = 50$ mm has been estimated to yield $\Im(Z/n) \approx 0.07$ (Ω) [28].

The real part of the transverse impedance, $\Re(Z_{tr})$, is not affected by the new electrode. The imaginary part is also not affected at low frequencies (up to 10 kHz). Above 10 kHz $\Im(Z_{tr})$ is increased. For thin layers $\Im(Z_{tr})$ is proportional to the layer thickness.

Concerning the dielectrics Fritz Caspers recommended recently [29] to use Al_2O_3 instead of vitreous enamel due to it's better mechanical stability. A thin 30 mm wide Al_2O_3 layer can be deposited at the bottom of the beam pipe using plasma spraying. The highly resistive coating on top of the dielectric can be realized using commercially available thick film pastes from Heraeus. These thick film pastes are developed for the production of electronic circuits and sensors [31].

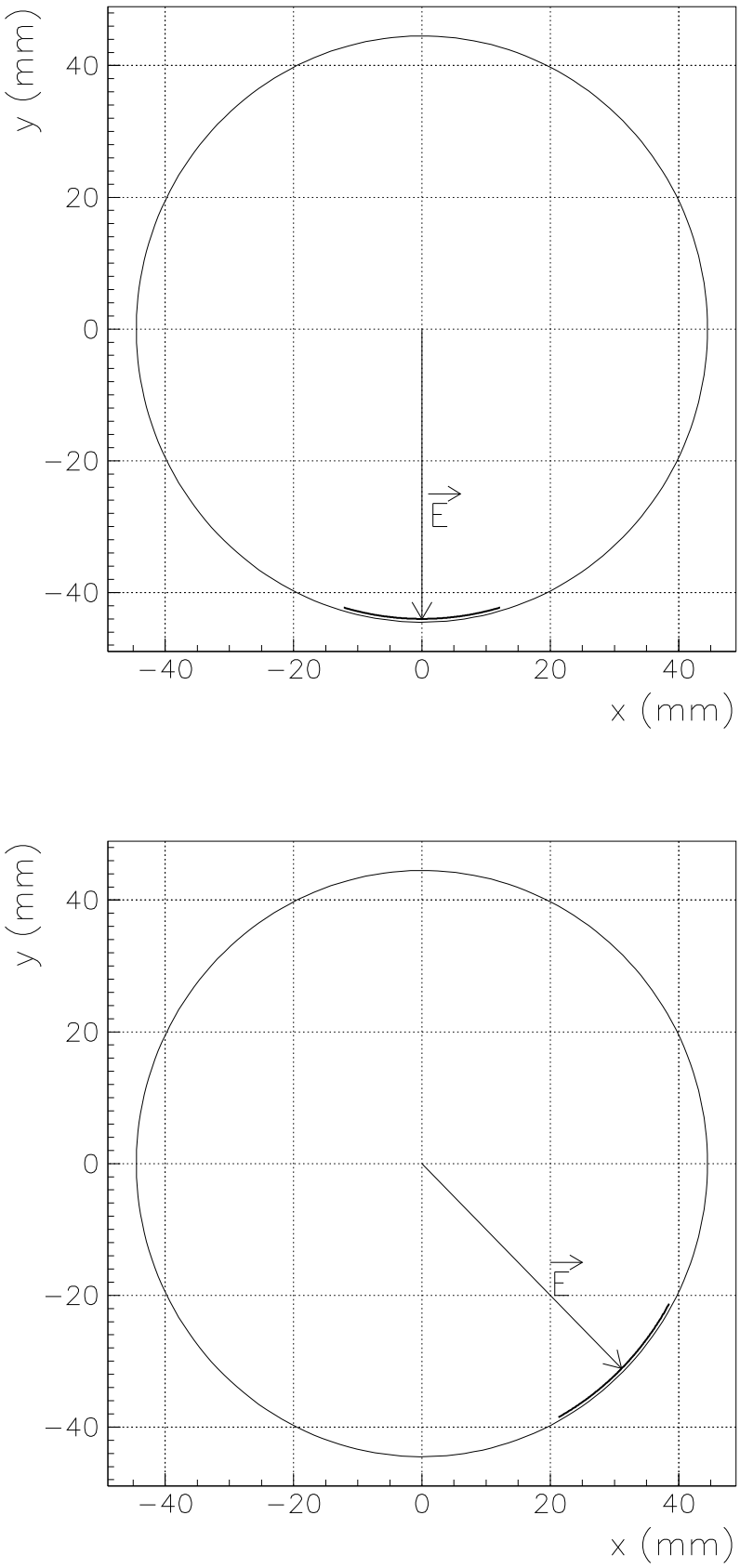

Fig. 13: Continuous clearing electrodes. **Top**: Clearing electrodes on the bottom of the beam pipe in the region of drift spaces and dipole magnets. **Bottom**: Clearing electrodes in the region of quadrupole magnets. The ions are extracted under $-45°$ along the principal direction of the magnetic field lines towards the clearing electrode.

10.4 Electric field of continuous clearing electrodes

We assume 25 mm wide clearing electrodes at the bottom of the beam pipes. The positive ions which are created inside the beam envelopes are immediately accelerated towards the clearing electrode. The clearing rate depends on the electric field distribution inside the beam pipe, especially on the electric field component E_y at the beam center.

The potential distribution $\Phi(\rho, \phi)$ inside the beam pipe can be evaluated using the following equation (see Problem 2.12 in the book 'Classical Electrodynamics', by John David Jackson, John Wiley & Sons Inc., New York (1998), Third Edition, page 89)

$$\Phi(r, \phi) = \frac{1}{2\pi} \int_0^{2\pi} \Phi(b, \phi') \frac{b^2 - r^2}{b^2 + r^2 - 2br\cos(\phi' - \phi)} d\phi'. \tag{74}$$

Here, $\Phi(b, \phi')$ is the potential specified on the surface of a cylinder of radius b, r and ϕ are the cylinder coordinates inside the cylinder. The potential on the surface is mainly zero (earth potential of the beam pipe). In a small angle interval $\Delta\phi'$ near $\phi' = 3\pi/2$, i.e. $3\pi/2 - \Delta\phi'/2 < \phi' < 3\pi/2 + \Delta\phi'/2$, it is equal to the clearing voltage $\Phi_0 = -1.0$ kV. Thus we have

$$\begin{aligned} \Phi(b, \phi') &= \Phi_0 \text{ for } 3\pi/2 - \Delta\phi'/2 < \phi' < 3\pi/2 + \Delta\phi'/2, \\ \Phi(b, \phi') &= 0 \text{ for } 0 < \phi' < 3\pi/2 - \Delta\phi'/2 \text{ and } 3\pi/2 + \Delta\phi'/2 < \phi' < 2\pi. \end{aligned} \tag{75}$$

We are mainly interested in the potential Φ and the electric field component E_y along the y-axis, i.e. for $\phi = 3\pi/2$ along the negative y-axis and for $\phi = \pi/2$ along the positive y-axis. The angle interval $\Delta\phi'$ which is covered by the 25 mm wide clearing electrode is very small. Therefore, $\cos(\phi' - \phi)$ is practically constant in the angle interval $\Delta\phi'$ and we get approximately

$$\begin{aligned} \cos(\phi' - \phi) &\approx +1 \text{ for } \phi = 3\pi/2, \\ \cos(\phi' - \phi) &\approx -1 \text{ for } \phi = \pi/2. \end{aligned} \tag{76}$$

Using this approximation[5] we can solve the integral (74),

$$\begin{aligned} \Phi(r, \phi) &= \Phi_0 \frac{\Delta\phi}{2\pi} \frac{b^2 - r^2}{b^2 + r^2 - 2br} \text{ for } \phi = 3\pi/2, \\ \Phi(r, \phi) &= \Phi_0 \frac{\Delta\phi}{2\pi} \frac{b^2 - r^2}{b^2 + r^2 + 2br} \text{ for } \phi = \pi/2. \end{aligned} \tag{77}$$

Using Cartesian coordinates $x = r\cos\phi$ and $y = r\sin\phi$ yields the solution along the y-axis in the following form

$$\Phi(x = 0, y) = \Phi_0 \frac{\Delta\phi}{2\pi} \frac{b^2 - y^2}{b^2 + y^2 + 2by}. \tag{78}$$

Using $\vec{E} = -grad\,\Phi$ yields the electric field $\vec{E}$ inside the beam pipe. The electric field component $E_y = -\partial\Phi/\partial y$ along the y-axis can be written

$$E_y(x = 0, y) = \frac{\Delta\phi}{2\pi} \Phi_0 \frac{2y(b^2 + y^2 + 2by) + (2y + 2b)(b^2 - y^2)}{(b^2 + y^2 + 2by)^2}. \tag{79}$$

Numerically, we get for a 25 mm wide clearing electrode and a beam pipe radius $b = 44.5$ mm $\Delta\phi = 25/(2\pi\,44.5) = 0.08941$ rad $= 5.12^\circ$ and $\Delta\phi/(2\,\pi) = 0.0142$. Assuming a

[5] The approximation cannot be used for test points very close to the clearing electrode.

clearing voltage $\Phi_0 = -1.0$ kV we get for $(x, y) = (0, 0)$, i.e. for the beam center

$$\begin{aligned} \Phi(0,0) &= -14.2 \text{ V}. \\ E_y(0,0) &= -640 \text{ V/m}. \end{aligned} \tag{80}$$

We note that the beam pipe radius is not always $b = 44.5$ mm. For instance in the region of the PANDA dipole magnet the radius b amounts to 50 mm. Thus, assuming a 25 mm wide clearing electrode and a clearing voltage $\Phi_0 = -1.0$ kV we get $\Phi(0, 0) = -12.7$ V and $E_y(0, 0) = -507$ V/m.

10.5 Estimate of the beam deflection by continuous clearing electrodes

Finally, we estimate the beam deflection by the electric field of continuous clearing electrodes. We assume an electric field component E_y of -640 V/m at the beam center and an effective length L of about 20 m. As discussed in the previous Subsection such electric fields can be made using clearing voltages of -1.0 kV in a 89 mm wide beam pipe. The resulting deflection angle Θ can be calculated using

$$\Theta = \frac{eE_yL}{pv}. \tag{81}$$

Here, p is the momentum and $v = \beta c$ the velocity of the beam. For a typical beam momentum $p = 8.889$ GeV/c we get

$$\Theta = 1.45 \cdot 10^{-6} \text{ rad}. \tag{82}$$

Thus, the deflection angle is negligibly small.

10.6 Clearing rates using continuous clearing electrodes

Here, we estimate the clearing rates R_c and clearing times T_c of continuous clearing electrodes. The clearing rate R_c is related to the mean clearing time T_c which is needed in order to extract a trapped ion out of the antiproton beam, $R_c = 1/T_c$.

We assume an electric field at the beam center of $E_y = -640$ V/m. The average value of the electric field of the beam (averaged over the full Gaussian beam distribution) is zero since $E_{y,beam}$ is positive for $y < 0$ and negative for $y > 0$. Thus, we assume a mean electric field $\bar{E}_y = -640$ V/m. For singly charged trapped ions the resulting mean acceleration is

$$\bar{a}_y = \frac{e\bar{E}_y}{m}. \tag{83}$$

Estimating the mean clearing time T_c we assume a mean flight path length of $3\sigma_y$. That means ions which are created in the beam center $y = 0$ reach the beam edge at $y = 3\sigma_y$. This assumption yields

$$T_c \approx \sqrt{\frac{6\sigma_y}{|\bar{a}_y|}}. \tag{84}$$

For σ_y we take $\sigma_y = 3$ mm which is a typical value near the PANDA target, see Fig. 4. The resulting mean accelerations $|\bar{a}_y|$, clearing times T_c, clearing rates R_c, production times T_p and neutralizations η are listed for H_2^+ and CO^+ ions in Tables 12 and 13.

Summarizing we note that continuous clearing electrodes yield very high clearing rates. They can be used to counteract trapped ion effects in the region of the PANDA target, see Sect. 12..

Table 12: Mean acceleration $|\bar{a}_y|$, mean clearing time T_c ($L = 3\sigma_y \approx 9$ mm), production time T_p and neutralization η for H_2^+ ions using continuous clearing electrodes and assuming a partial H_2 pressure of $0.8 \cdot 10^{-9}$ mbar.

p (GeV/c)	$\lvert\bar{a}_y\rvert$ (m/s^2)	T_c (s)	R_c(s^{-1})	T_p (s)	η
1.5	$3.07 \cdot 10^{10}$	$7.66 \cdot 10^{-7}$	$1.31 \cdot 10^{6}$	9.22	$7.48 \cdot 10^{-8}$
3.825	$3.07 \cdot 10^{10}$	$7.66 \cdot 10^{-7}$	$1.31 \cdot 10^{6}$	9.29	$7.42 \cdot 10^{-8}$
8.889	$3.07 \cdot 10^{10}$	$7.66 \cdot 10^{-7}$	$1.31 \cdot 10^{6}$	8.69	$7.93 \cdot 10^{-8}$
15.0	$3.07 \cdot 10^{10}$	$7.66 \cdot 10^{-7}$	$1.31 \cdot 10^{6}$	7.98	$8.64 \cdot 10^{-8}$

Table 13: Mean acceleration $|\bar{a}_y|$, mean clearing time T_c ($L = 3\sigma_y \approx 9$ mm), production time T_p and neutralization η for CO^+ ions using continuous clearing electrodes and assuming a partial CO pressure of $0.2 \cdot 10^{-9}$ mbar.

p (GeV/c)	$\lvert\bar{a}_y\rvert$ (m/s^2)	T_c (s)	R_c(s^{-1})	T_p (s)	η
1.5	$2.19 \cdot 10^{9}$	$2.87 \cdot 10^{-6}$	$3.48 \cdot 10^{5}$	8.50	$3.03 \cdot 10^{-7}$
3.825	$2.19 \cdot 10^{9}$	$2.87 \cdot 10^{-6}$	$3.48 \cdot 10^{5}$	8.33	$3.10 \cdot 10^{-7}$
8.889	$2.19 \cdot 10^{9}$	$2.87 \cdot 10^{-6}$	$3.48 \cdot 10^{5}$	7.45	$3.47 \cdot 10^{-7}$
15.0	$2.19 \cdot 10^{9}$	$2.87 \cdot 10^{-6}$	$3.48 \cdot 10^{5}$	6.92	$3.73 \cdot 10^{-7}$

11. Ion Clearing in Solenoids Using Transverse Cross-Field-Drift Velocities

In a field-free region of a drift space trapped ions can easily be extracted using clearing electrodes. Such a direct extraction is not possible in the region of a solenoid due to the longitudinal magnetic field. However one can use the effect of the $\vec{E} \times \vec{B}/B^2$ cross-field-drift velocity, see Subsection 8.2 and Fig. 11.

By adjusting for instance a certain transverse electric field E_y the resulting cross-field-drift velocity amounts to $|E_y/B_z|$ and is directed in the x-direction. Using this effect one can guide the trapped ions towards clearing electrodes located on the left- or right-hand side of the beam. Similarly, it is possible to adjust a certain transverse electric field E_x in order to extract trapped ions with electrodes located above or below the antiproton beam.

The scheme of ion clearing in a solenoid is shown in Fig. 14. The ion clearing device consists of two metallic half cylinders separated by high-resistive-glass insulators connected to earth and acting as clearing electrodes. The clearing device and the neighbouring vacuum chamber have the same inner diameter (89 mm). The length can be chosen freely. One can take for instance the effective length of the solenoid.

The voltages $V_2 = -U_0$ and $V_1 = +U_0$ on the opposite electrodes are oppositely equal. Thus, we have $V_2 - V_1 = -2U_0$. The resulting electric field must be higher than the electric field of the $\bar{\mathrm{p}}$-beam. The electric field can be evaluated using the following equation (see Problem 2.12 in the book 'Classical Electrodynamics', by John David Jackson, John Wiley & Sons Inc., New York (1998), Third Edition, page 89)

$$\Phi(r,\phi) = -\frac{2U_0}{\pi} \arctan\left(\frac{2br\sin\phi}{b^2 - r^2}\right). \tag{85}$$

where b is the radius of the half-cylinders and ϕ is measured from a plane through the gap (i.e. the x-axis). Using Cartesian coordinates instead of cylinder coordinates we have $x = r\cos\phi$ and $y = r\sin\phi$. The electric field $\vec{E}$ inside a very long clearing device is given by

$$(E_x, E_y, E_z) = -\left(\frac{\partial\Phi}{\partial x}, \frac{\partial\Phi}{\partial y}, 0\right). \tag{86}$$

We are mainly interested to evaluate E_y,

$$E_y = \frac{2U_0}{\pi}\left(1 + \tan^2\frac{2by}{b^2 - (x^2+y^2)}\right)\frac{2b(b^2 - (x^2+y^2)) + 4by^2}{(b^2 - (x^2+y^2))^2}. \tag{87}$$

This yields for the beam center $(x, y) = (0, 0)$

$$E_y(x,0) = \frac{4}{\pi}\frac{U_0}{b}. \tag{88}$$

We note that $E_y(x,0)$ increases on the way from the beam center towards the clearing electrode. For a radius $b = 44.5$ mm and a voltage $U_0 = 105$ V we get $E_y(0,0) \approx 3.0$ kV/m in the beam center.

An electric field of about 3.0 kV/m and a solenoid field of 1.5 T yield rather high cross-field-drift velocities of about 2000 m/s. The ions drift towards the high-resistive-glass electrodes where they are neutralized. We mention that such clearing devices have been used at LEAR in order to extract the secondary electrons from the ionization processes of the residual gas in the electron-cooling beam [49].

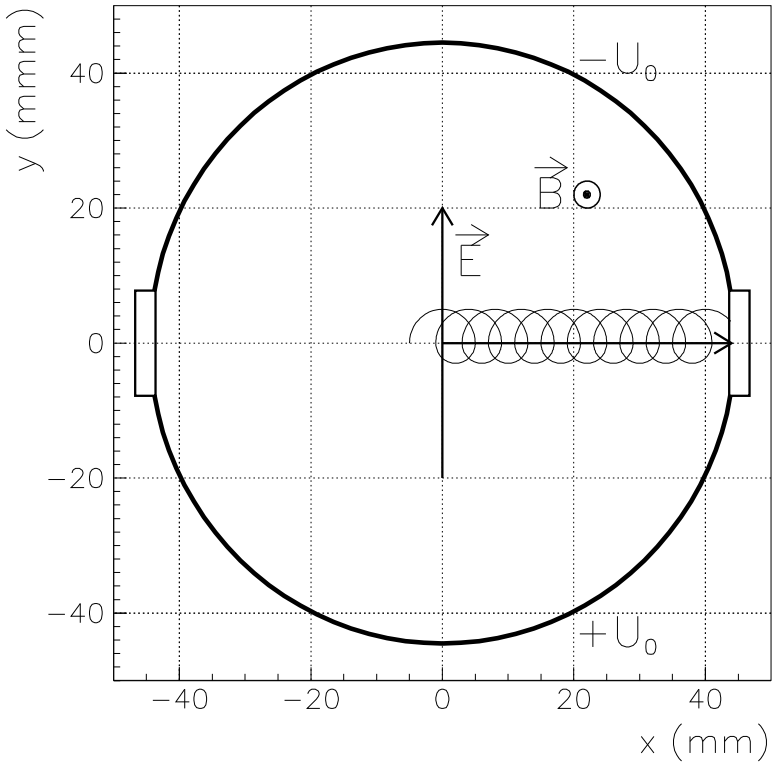

Fig. 14: Scheme of ion clearing in a solenoid: The transverse electric field $\vec{E}$ is generated with two metallic half cylinders separated by high-resistive-glass insulators which act as clearing electrodes. Here, the resulting cross-field-drift velocity $\vec{v}_D = \vec{E} \times \vec{B}/B^2$ is directed in the positive x-direction. The modified cyclotron motion of the ions is not true to scale. In reality the cyclotron radii of thermal ions amount to a few micrometers.

12. Counteracting Trapped Ion Effects near the PANDA Target

12.1 Preliminary remark

In the immediate neighbourhood of the PANDA target (see Figs. 15 and16) the vacuum pressure is very high due to the H_2 cluster jet or pellet target [25], see Figs. 17 and 18. Therefore, the H_2^+ ion production rate is much higher than in the remaining sections outside the target region. Without clearing the antiproton beam is fully neutralized within a few milliseconds. It is interesting to note that the pressure bump of the pellet target is about a factor of hundred higher than that of the cluster jet target. Therefore, we consider in the following the worst case, i.e. the H_2 gas input from the pellet target.

In the following Subsection 12.2 we estimate the clearing times $T_c(s)$ and the neutralizations $\eta(s)$ which can be achieved using either single isolated clearing electrodes (see Subsect. 10.2) or continuous clearing electrodes (see Subsects.10.3 - 10.6). The comparison of both methods shows that a sufficient low neutralization can only be achieved using continuous clearing electrodes.

Continuous ion clearing in the immediate neighbourhood of the PANDA target would be the optimum solution to the trapped ion problem. However, it is necessary to consider the geometrical constraints which are due to the PANDA experiment. The possibility to abandon continuous ion clearing in the regions of the target solenoid and the compensation solenoid is discussed in Subsections 12.3-12.4.

In Subsection 12.5, we show the resulting neutralization profile $\eta(s)$ near the PANDA target if continuous clearing is abandoned in the regions of the compensation solenoid and the PANDA target solenoid.

The remaining sections between $s = 488$ m and $s = 508$ m and between $s = 512.5$ m and $s = 532$ m consist of a dipole spectrometer, drift spaces, quadrupole magnets and correction dipole magnets of the PANDA chicane. Most critical are the transition regions where the neutralization decreases slowly from 100 % to 1 %. There, dangerous coherent ion-beam oscillations can occur. The necessity of continuous ion clearing in those regions is discussed in Subsections 12.6 - 12.9.

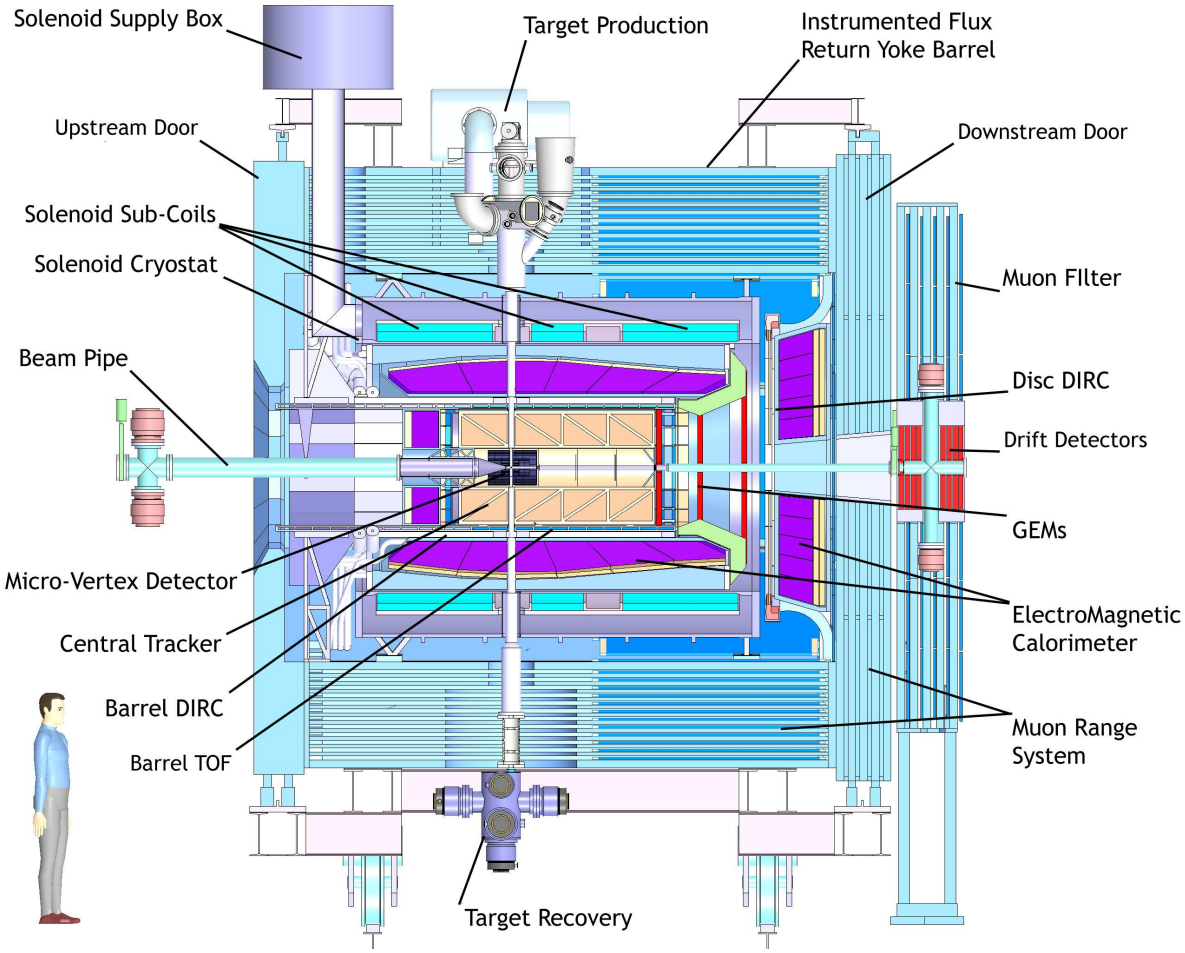

Fig. 15: PANDA target spectrometer with solenoid and detector components. The figure is taken from the Technical Design Report for the PANDA Internal Targets [25].

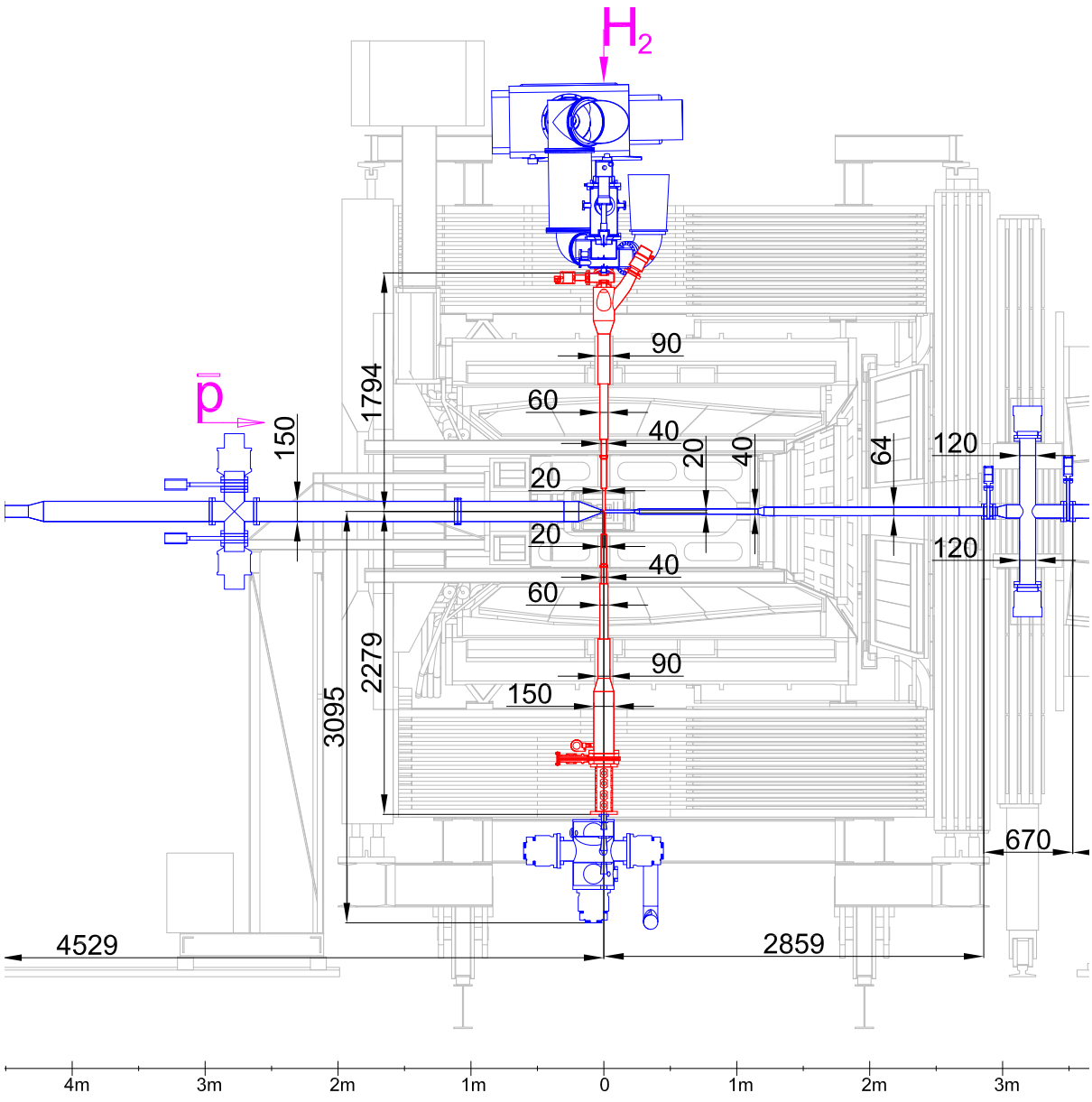

Fig. 16: Cross section of the PANDA target spectrometer with solenoid and detector components. The target and dump lines are marked in red, the $\bar{p}$ beam pipe in blue. The dimensions are given in mm. The diameters refer to inner diameters of the tubes. The figure is taken from the Technical Design Report for the PANDA Internal Targets [25].

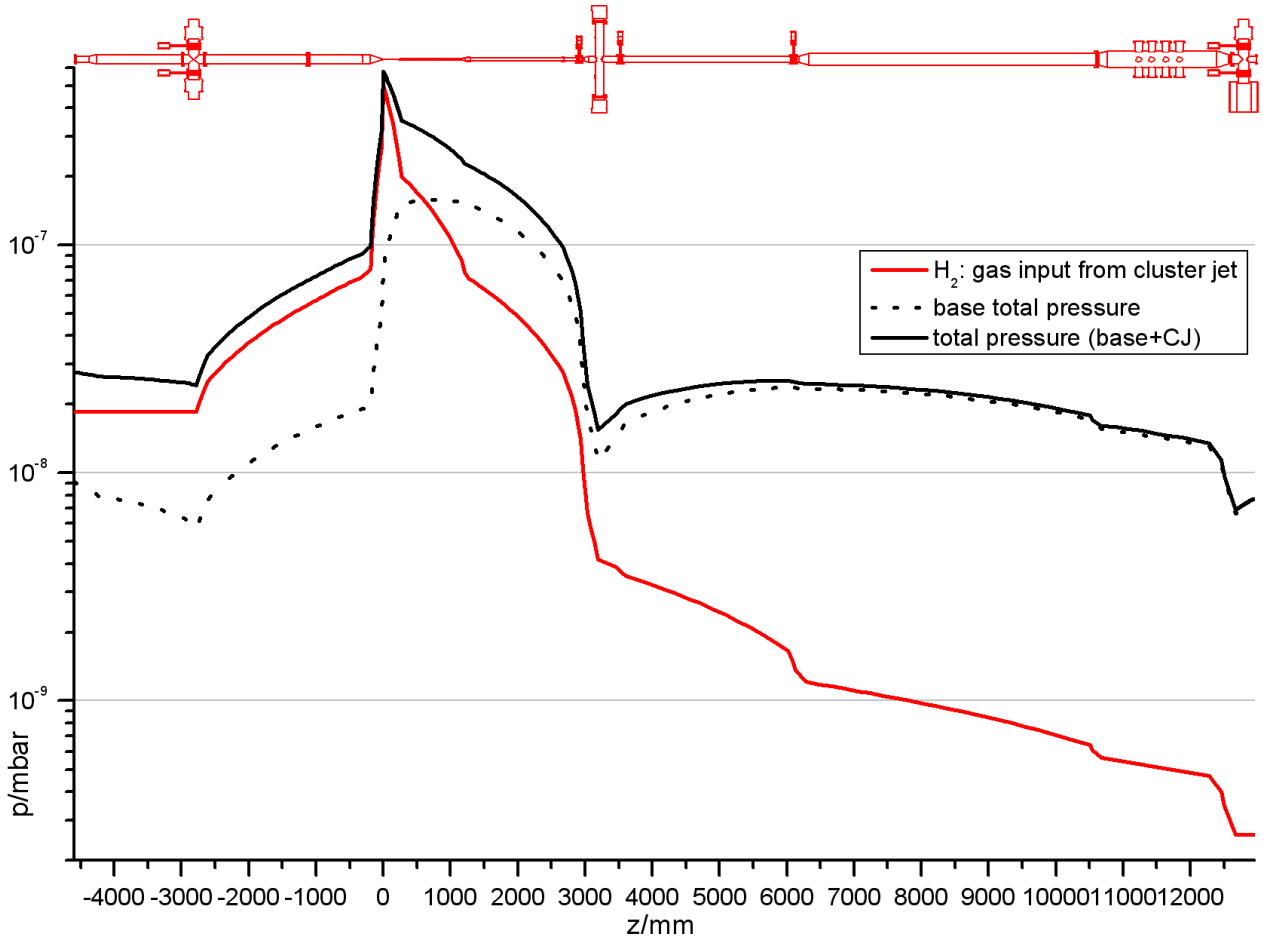

Fig. 17: Pressure profile with cluster-jet target. The beam pipe is shown above the plots. The figure is taken from the Technical Design Report for the PANDA Internal Targets. [25].

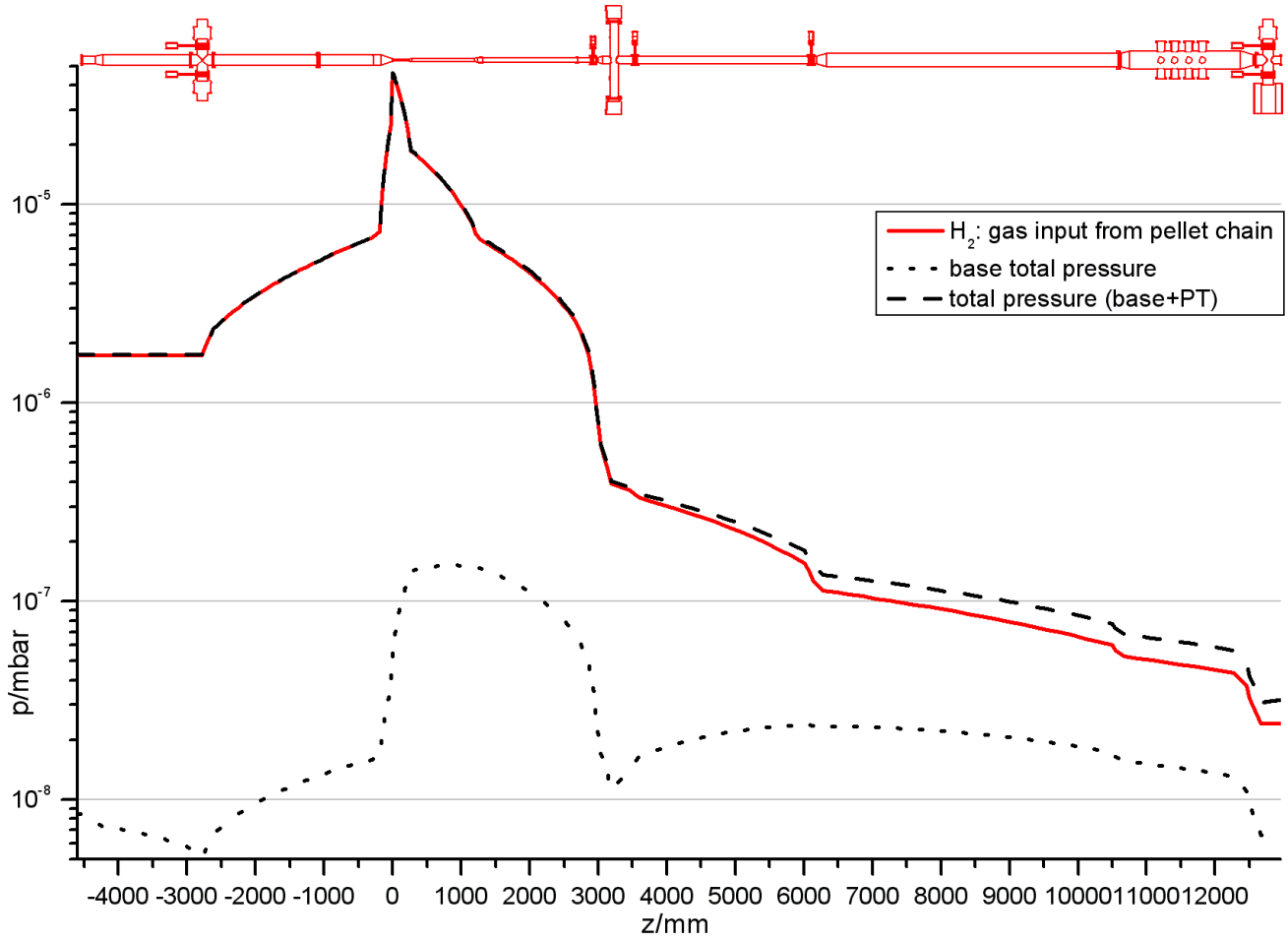

Fig. 18: Pressure profile with pellet target. The beam pipe is shown above the plots. The figure is taken from the Technical Design Report for the PANDA Internal Targets. [25].

12.2 Counteracting the very high production rates of H_2^+ ions near the PANDA target

In order to counteract the very high production rates of H_2^+ ions near the PANDA target especially high clearing rates are necessary. We show that the necessary clearing rates can be achieved with continuous clearing electrodes, see Subsect. 10.6. The clearing rates of single isolated clearing electrodes (see Subsect. 10.2) are not sufficient. In the following we consider only the dominating H_2^+ ions.

Concerning single isolated clearing electrodes (see Subsect. 10.2) we assume that they are located at a distance $L = 5.0$ m. We note that this distance corresponds to the length of the compensation solenoid. The clearing time T_c depends on the longitudinal electric field E_s of the antiproton beam. The resulting acceleration a_s may be written $a_s = (e/m)E_s$. Taking as mean flight-path length $L/2 = 2.5$ m yields a mean clearing time $T_c = \sqrt{L/a_s}$ and a neutralization $\eta = 0.9\,T_c/T_p$. The longitudinal electric field E_s depends strongly on the number $N_{\bar{p}}$ of circulating antiprotons. For $1.0 \cdot 10^{11}$ antiprotons the longitudinal electric field varies between 0.057 V/m and 0.11 V/m in the region of the compensation solenoid. For $1.0 \cdot 10^{10}$ antiprotons the longitudinal electric field is about a factor of eight lower. In the top graphs of Fig. 19 and 20 the resulting neutralization $\eta(s)$ is shown for $N_{\bar{p}} = 1.0 \cdot 10^{11}$ and $N_{\bar{p}} = 1.0 \cdot 10^{10}$, respectively.

The continuous clearing electrodes (see Subsect. 10.6) are deposited at the bottom of the beam pipe. In the region of quadrupole magnets the electrodes are deposited at the -45° side. The positive ions which are created inside the beam envelopes are immediately accelerated towards the clearing electrode. We assume an electric field at the beam center of $E_y = 640$ V/m. This can be achieved with a clearing voltage of -1.0 kV for a beam pipe diameter of 89 mm. For H_2^+ ions the resulting mean acceleration is $a_y = 3.07 \cdot 10^{10}$ m/s^2. Estimating the mean clearing time T_c we assume a mean flight path length of $3\sigma_y$. That means, ions which are created in the beam center $y = 0$ reach the beam edge at $y = 3\sigma_y$. This assumption yields $T_c \approx \sqrt{6\sigma_y/a_y}$ and $\eta = 0.9T_c/T_p$. Taking for instance $\sigma_y = 3$ mm and $a_y = 3.07 \cdot 10^{10}$ m/s^2 yields $T_c = 7.66 \cdot 10^{-7}$ s.

In the region of solenoids (PANDA target solenoid between $s = 508.0$ m and $s = 512.5$ m and compensation solenoid between $s = 500.2$ m and $s = 505.2$ m) continuous clearing can be achieved using the transverse cross-field velocity, see Sect. 11.. To this end, the beam pipe consists of two metallic half cylinders separated by high resistive glass-insulators acting as clearing electrodes. A transverse electric field E_y and a longitudinal magnetic field B_z yield a transverse cross-field velocity $v_x = E_y/B_z$. A high velocity of 1000 m/s can be achieved with $E_y = 1.5$ kV/m and $B_z = 1.5$ T in the region of the compensation solenoid and with $E_y = 2.0$ kV/m and $B_z = 2.0$ T in the region of the target solenoid. Assuming a mean flight path length of $3\sigma_x$ the clearing time may be estimated using $T_c = 3\sigma_x/v_x$. The resulting clearing times are sufficient low. Taking for instance $\sigma_x = 3$ mm and $v_x = 2000$ m/s yields $T_c = 1.5 \cdot 10^{-6}$ s. In the bottom graphs of Fig. 19 and 20 the resulting neutralization $\eta(s)$ is shown for $N_{\bar{p}} = 1.0 \cdot 10^{11}$ and $N_{\bar{p}} = 1.0 \cdot 10^{10}$, respectively.

Summarizing, single isolated electrodes yield dangerous high neutralizations near the PANDA target. The highest neutralizations result for $1.0 \cdot 10^{10}$ antiprotons (see top graphs in Figs. 19 and 20) yielding $\eta > 0.1$ between about $s = 500$ m and $s = 515$ m and $\eta > 0.01$ between about $s = 490$ m and $s = 530$ m. Sufficient low neutralizations with $\eta < 0.01$ can only be achieved with continuous clearing electrodes, see bottom graphs in Figs. 19 and 20.

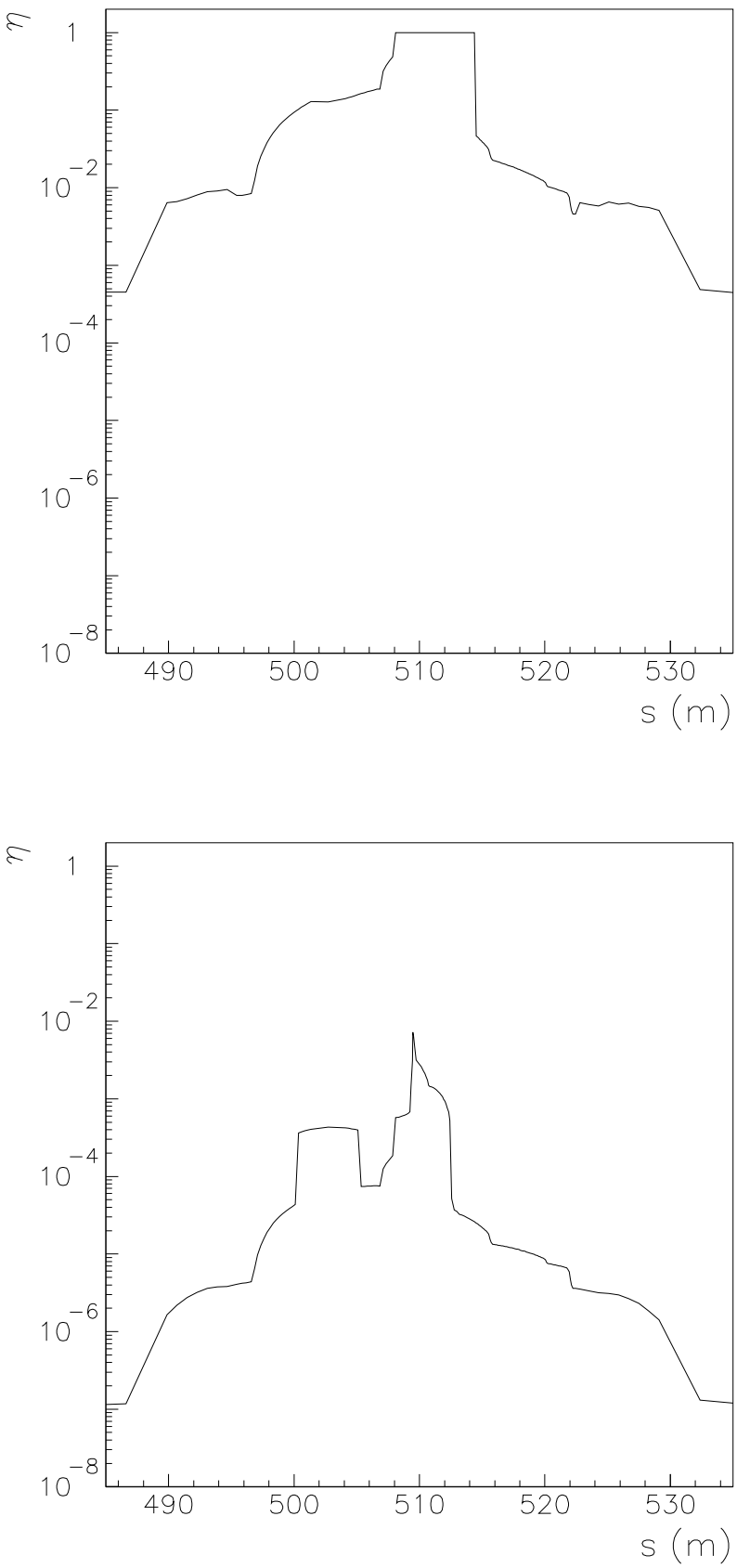

Fig. 19: Neutralization $\eta(s)$ near PANDA target for $N_{\bar{p}} = 1.0 \cdot 10^{11}$ and $p_{\bar{p}} = 8.889$ GeV/c. **Top**: Single isolated clearing electrodes (distance 5.0 m). **Bottom**: Continuous clearing electrodes.

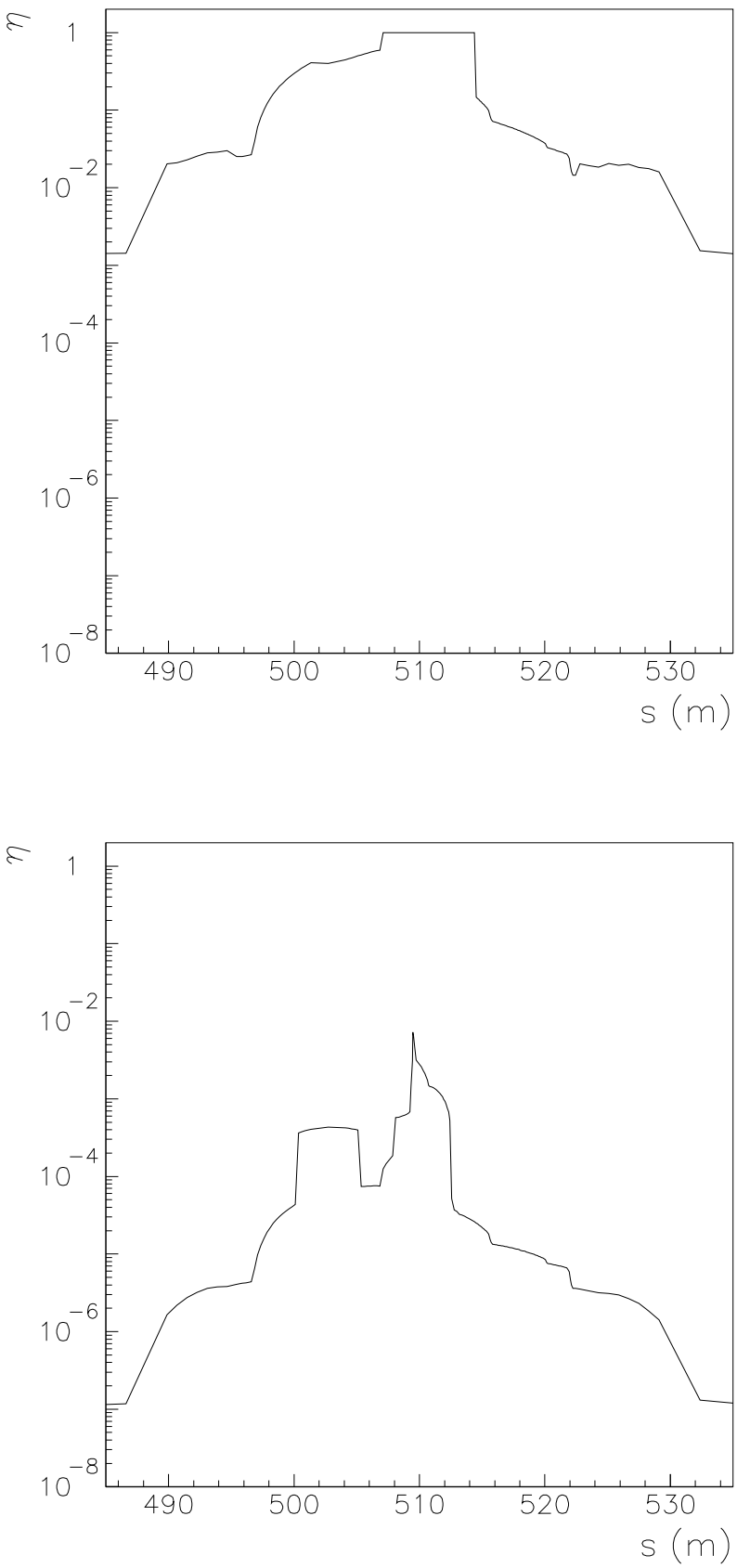

Fig. 20: Neutralization $\eta(s)$ near PANDA target for $N_{\bar{p}} = 1.0 \cdot 10^{10}$ and $p_{\bar{p}} = 8.889$ GeV/c. **Top**: Single isolated clearing electrodes (distance 5.0 m). **Bottom**: Continuous clearing electrodes.

12.3 The PANDA target solenoid

Here, we discuss the necessity to abandon continuous clearing in the region of the PANDA target solenoid. We first sketch the geometrical constraints in the region of the PANDA target solenoid. Then, we discuss the situation if continuous clearing is abandoned in the region of the PANDA target solenoid.

The PANDA target solenoid surrounds the interaction point, see Figs. 15 and 16. It is used as spectrometer for the detection of scattered particles in a highly homogeneous solenoidal field. The magnetic field of the solenoid is provided by a large superconducting coil with an inner diameter of 2.010 m and a length of 2.80 m. The maximum magnetic field amounts to 2.0 T. The detectors are located inside the large solenoid. Including the fringe fields, the magnetic field of the PANDA solenoid extends over a distance of about 5.50 m from $s = 507.5$ m to $s = 513.0$ m. The PANDA target is located at $s = 509.481$ m.

In order to sketch the geometrical constraints near the PANDA target we consider the geometry of the beam pipe, see Fig. 16. The upstream beam pipe between the pumping station outside the target solenoid and the target point has a total length of about 2.86 m and a large inner diameter of 150 mm. Near the target the beam pipe changes over to a very small inner diameter of 20 mm. The downstream beam pipe next to the target is a very small and fragile tube with a total length of 0.200 m, an inner diameter of 20 mm and a wall thickness of 0.5 mm. It consists of a special BeAl alloy in order to keep the small angle scattering of the scattered particles as small as possible. The downstream beam pipe continues with a transition to an inner diameter of 40 mm and a total length of 0.923 m.

The upstream and downstream beam pipe is tightly surrounded by the PANDA detector system nested inside the solenoidal magnetic field. It consists of Micro-Vertex Detectors (MVD), Central Trackers, Barrel DIRC's and Disc DIRC's (Detectors of Internally Reflected Cherenkov light), Barrel Time-Of-Flight (TOF) detectors, Gas Electron Multiplier (GEM) detectors, Drift Detectors and Electromagnetic Calorimeters (EMC).

In view of the tight geometrical constraints it is probably not possible to install continuous ion clearing in the region PANDA target solenoid. Especially, it is very difficult to cut the 0.5 mm thick beam pipe next to the interaction point into two half cylinders separated by very thin and high resistive glass-insulators acting as clearing electrodes. Therefore, we discuss the situation if continuous clearing is abandoned.

The local density of H_2 molecules is very high near the PANDA target due to the gas input from the PANDA target. As mentioned, we consider the gas input from the pellet target. Near the target point the pressure and the production time T_p for H_2^+ ions amount to about $6.0 \cdot 10^{-5}$ mbar and 0.113 ms, respectively, see Figs. 9 and 10. At the entrance and exit of the target solenoid the pressures are still very high. They amount to about $5.2 \cdot 10^{-6}$ mbar and $6.0 \cdot 10^{-6}$mbar, respectively. The corresponding production times T_p amount to about 1.3 ms and 1.1 ms, respectively.

In addition, there is a narrow beam waist in x- and y-direction at the target point. As a consequence the longitudinal electric field E_s of the antiproton beam is directed towards the target point, both downstream and upstream, see Fig. 8. Thus, positive ions are accelerated towards the target point instead of being accelerated towards clearing electrodes at the entrance and exit of the target solenoid. The magnetic field of the solenoid and the longitudinal electric field component of the beam act as a perfect ion trap. Without clearing the antiproton beam is fully neutralized within a very short period of time ($t < 1$ ms) and the longitudinal electric field

E_s of the beam is canceled by the space charge of the trapped ions.

Then, the antiproton beam produces continuously further ions and electrons with a very high production rate. These ions and electrons can only escape in the longitudinal direction along the magnetic field lines of the target solenoid. In the fringe field of the solenoid the ions and electrons follow adiabatically the magnetic field lines towards the beam pipe where they are neutralized, see Subsect. 9.4.

There are two reasons why dangerous transverse ion oscillations cannot occur. (i) The potential well of the antiproton beam is fully neutralized by the trapped ions. (ii) The ions perform tight cyclotron motions around the longitudinal magnetic field lines of the PANDA solenoid (2.0 T). Therefore, one can abandon continuous clearing in the region of the PANDA target solenoid.

12.4 The compensation solenoid near the PANDA target

Here, we discuss the possibility to abandon continuous clearing in the region of the compensation solenoid as shown in Fig. 14. The 5 m long compensation solenoid with a magnetic field direction opposite to the magnetic field direction of the PANDA target solenoid extends from $s = 500.23$ m to $s = 505.23$ m. First, we estimate the neutralization in the region of the compensation solenoid. Fortunately, the longitudinal electric field E_s is unidirectional (directed in the positive s-direction). The trapped ions move along the magnetic field lines towards the fringe field of the compensation solenoid. There, the ions follow adiabatically the magnetic field lines towards the beam pipe where they are neutralized, see Subsect. 9.4. The mean clearing time T_c depends on the strength of the longitudinal electric field. For $1.0 \cdot 10^{11}$ antiprotons the longitudinal electric field varies between 0.057 V/m and 0.11 V/m and the clearing time T_c is dominated by the longitudinal acceleration of the ions. It yields for H_2^+ ions $T_c \approx 1.1$ ms and $\eta \approx 0.11$ in the region of the compensation solenoid. For $1.0 \cdot 10^{10}$ antiprotons the longitudinal electric field is about a factor of eight lower but the clearing time T_c is still dominated by the longitudinal acceleration of the ions. It yields for H_2^+ ions $T_c \approx 3.0$ ms and $\eta \approx 0.29$ in the region of the compensation solenoid. Thus, the potential well of the antiproton beam is not fully neutralized by the trapped ions. But dangerous transverse ion oscillations cannot be excited due to the longitudinal magnetic field of the solenoid. The ions perform tight cyclotron motions around the longitudinal magnetic field lines of the PANDA solenoid (1.5 T). Therefore, one can abandon continuous clearing in the region of the compensation solenoid.

12.5 Neutralization $\eta(s)$ if continuous ion clearing is abandoned in the region of the compensation solenoid and the PANDA target solenoid

Here, we show the resulting neutralization $\eta(s)$ if continuous ion clearing is abandoned in the region of the compensation solenoid and the PANDA target solenoid as discussed in the previous Subsects. 12.3 and 12.4. We emphasize that it is absolutely necessary to provide continuous ion clearing in the dipole specrometer, the drift spaces, the quadrupole magnets and the correction dipoles near the PANDA target, see Subsects. 12.6 - 12.9. Otherwise, the neutralization levels would be in the most critical range $1\% < \eta < 100\%$ where dangerous coherent ion-beam oscillations can occur. The resulting neutralization $\eta(s)$ is shown in Fig. 21 for $p_{\bar{p}} = 8.889$ GeV/c. The top and bottom graphs refer to $N_{\bar{p}} = 1.0 \cdot 10^{11}$ and $N_{\bar{p}} = 1.0 \cdot 10^{10}$, respectively.

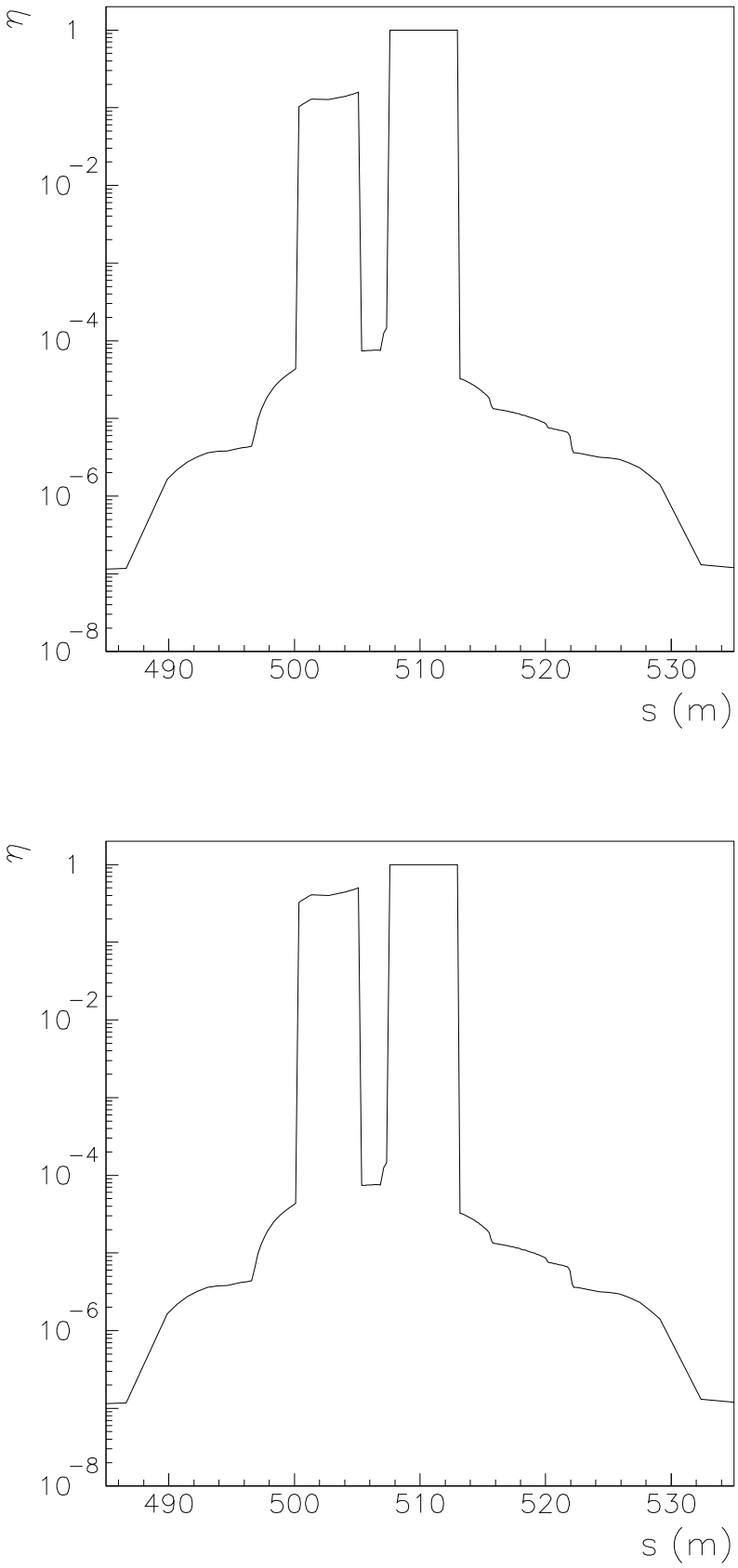

Fig. 21: Neutralization $\eta(s)$ near PANDA target for $p_{\bar{p}} = 8.889$ GeV/c if continuous ion clearing is abandoned in the regions of the compensation solenoid and the PANDA target solenoid. **Top**: $N_{\bar{p}} = 1.0 \cdot 10^{11}$. **Bottom**: $N_{\bar{p}} = 1.0 \cdot 10^{10}$.

12.6 The dipole spectrometer magnet near the PANDA target

Dangerous coherent oscillations in the vertical y-direction can occur in the region of the dipole magnet of the PANDA Forward Spectrometer, see Fig. 22. The field integral of the dipole spectrometer magnet amounts to 2 Tm at 15 GeV/c. The magnet yoke will occupy about 1.6 m in beam direction starting from 3.9 m downstream of the target. The magnetic field of the dipole spectrometer magnet [40] extends from about $s = 512.5$ m to about $s = 516.5$ m, see Fig. 22. It is part of the HESR lattice. The resulting bending angle of the beam amounts to 40 mrad. Two 0.5 m long correcting dipole magnets are located at $s = 496.181$ m and $s = 522.781$ m in order to compensate the bending angle caused by the dipole spectrometer magnet.

The dipole spectrometer magnet with a maximum bending power of 2.0 Tm provides the necessary field strength in order to determine the momentum of scattered charged particles with a momentum resolution of 1 %. The gap of the dipole covers the entire angular acceptance of the target spectrometer of $\pm 10^\circ$ and $\pm 5^\circ$ in the horizontal and vertical directions, respectively. It will be 3 m wide and between 0.8 m (at the entrance) and 1.0 m (at the exit) high. The detector system will be equipped with drift chambers for particle tracking and scintillation counters for time-of-flight measurements inside the dipole magnet. The deflection of particle trajectories will be measured with three pairs of tracking drift detectors. The first pair is placed in front, the second within and the third behind the dipole magnet. The detector system inside the dipole magnet will be completed by a full forward detection system including luminosity detectors.

The PANDA dipole spectrometer magnet is located in a region where the residual H_2 gas pressure is still rather high (about $4.2 \cdot 10^{-7}$ mbar), see Fig. 18 and the production time T_p for H_2^+ ions is rather low (about 16 ms), see Fig. 10. The vertical magnetic field of the spectrometer has the advantage that ion oscillations in the horizontal x-direction are suppressed. The disadvantage is the fact that dangerous ion oscillations can occur in the vertical y-direction. Therefore, continuous clearing electrodes[6] are needed in order to extract the ions in the y-direction along the magnetic field lines, see Subsects. 10.3 and 10.4.

[6]The feasibilty of continuous clearing electrodes in the dipole region has recently been discussed during a meeting in the FZ Jülich (04.07.2012).

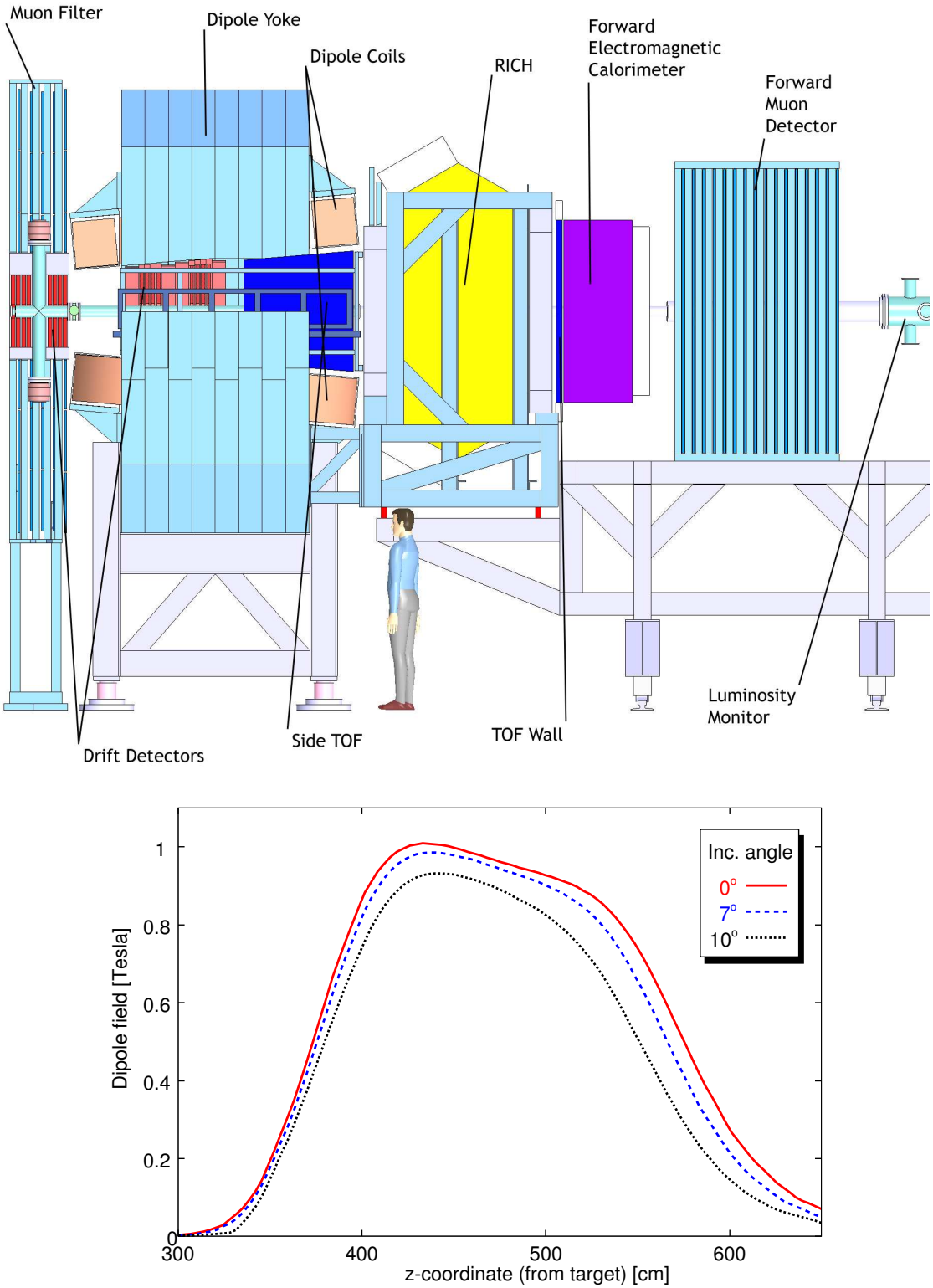

Fig. 22: Top: PANDA Forward Spectrometer with dipole magnet. The figure is from the PANDA-Target-TDR [41]. Bottom: Magnetic field along three straight lines in the horizontal plane of the dipole magnet. The straight lines originate at the PANDA interaction point with angles respective to the beam direction 0° (red solid curve), 7° (blue dashed curve) and 10° (black dotted curve). The figure is from the PANDA-Magnet-TDR [40].

12.7 The drift spaces near the PANDA target

Dangerous neutralization levels can also occur in the region of drift spaces near the PANDA target, i.e. drift spaces located upstream between $s = 488$ m and $s = 507.5$ m with T_p between 503 ms and 2.33 ms and downstream between $s = 513.0$ m and $s = 532$ m with T_p between 2.17 ms and 6.37 s, see Fig. 10. Clearing times down to $T_c < 2.4$ μs are needed in order to achieve a neutralization of less than 0.1 %. This can be achieved with continuous clearing electrodes inside the beam tubes, see Subsects. 10.3 and 10.4.

12.8 The quadrupole magnets near the PANDA target

Now, we discuss separately the situation in the region of the quadrupole magnets near the PANDA target. In order to produce a sharp double waist at the PANDA target point ever four quadrupoles are used as a quadrupole triplet. The centres of the quadrupoles QT3, QT4, QT4, QT3 in front of the target are located at 489.879 m, 491.479 m, 493.079 m and 494.679 m. The centres of the quadrupoles QT3B, QT4B, QT4B, QT3B after the target are located at 524.283 m, 525.883 m, 527.483 m and 529.083 m. The iron length of the quadrupoles is 0.58 m, the magnetic length is 0.60 m. The drift space between two adjacent quadrupole magnets is 1.0 m. The total length of a four-quadrupole array amounts to 5.4 m.

The continuous clearing in the region of the quadrupoles can be realized by extracting the ions along the principal direction of the magnetic field lines towards one of the pole tips, i.e. along one of the 45° diagonals of the quadrupole, see bottom graph in Fig. 13. To this end, the clearing electrode is **not** deposited at the bottom of the beam pipe but at the side of one of the 45° diagonals of the quadrupole. In the bottom graph of Fig. 13 the azimuthal position of the clearing electrode is -45°. The extraction along one of the 45° diagonals is necessary in order to keep the magnetic deflection of the ions on their way towards the clearing electrode negligibly small.

In principle, one can also use the -45° clearing electrode in the drift spaces between the quadrupoles. Thus, it is possible to use a single 5.4 m long clearing electrode in the region of a four-quadrupole array near the PANDA target.

12.9 The upstream and downstream dipole magnets of the PANDA chicane

The insertion of an internal dipole spectrometer in a straight section requires two additional dipole magnets in order to compensate the beam deflection. These correction dipole magnets are located near the PANDA target, i.e. DIPOL1 upstream at $s = 496.181$ m and DIPOL3 downstream at $s = 522.781$ m. The magnetic length of those dipole magnets amounts to 0.6 m, i.e. DIPOL1 extends from $s = 495.881$ m to 496.481 m and DIPOL3 from 522.481 m to 523.081 m. These dipole magnets are located in a region where the residual gas pressure is still rather high ($3.8 \cdot 10^{-8}$ mbar and $3.0 \cdot 10^{-8}$ mbar respectively) and the corresponding production time T_p of H_2^+ ions is rather low (0.177 s and 0.227 s, respectively). In order to avoid dangerous vertical ion oscillations, the ions are extracted along the magnetic field lines in the vertical direction using continuous clearing electrodes as in the region of drift spaces, see top graph in Fig. 13.

13. Mitigation of Trapped Ion Effects in the Dipole Magnets of the Arcs

13.1 Ion clearing in dipole magnets by mean cross-field drift velocities

The cross-field drift velocity $\vec{v}_D = \vec{E} \times \vec{B}/B^2$ can be used in order to guide the trapped ions to the entrance and exit of the dipole magnets (see Subsects. 8.2 and 8.3). There, the ions can be extracted using single isolated clearing electrodes. The cross-field drift velocity yields a longitudinal velocity component $v_D = E_x/B_y$. Here, E_x is the transverse electric field component of the beam in x-direction and B_y the transverse magnetic field component in y-direction. The cross-field drift velocities of ions created on the left side of the beam axis are negative, i.e. they are directed in the backward direction. Ions created on the right side of the beam axis drift in the forward direction. On either side the mean cross-field drift velocity $|\bar{v}_D|$ is rather small. This is due to the fact that the electric field component E_x and therewith the cross-field drift velocity drops down to zero at the beam center. Therefore, ions created near the beam center are practically not cleared and the resulting mean cross-field drift velocity $|\bar{v}_D|$ is rather low on either side.

As a consequence, the resulting beam neutralization is rather high assuming a residual gas pressure of $1.0 \cdot 10^{-9}$ mbar. In Tables 14 and 15, we list the mean cross-field drift velocity $|\bar{v}_D|$, the mean clearing time T_c for a mean drift of $L/2 = 2.25$ m (we assume that the clearing electrodes are located in the 0.3 m long drift spaces at the entrance and exit of the dipole magnets), the production time T_p for H_2^+ and CO^+ ions and the resulting neutralization $\eta = (L_1/C)(T_c/T_p) = 0.9(T_c/T_p)$ assuming $N_{\bar{p}} = 1.0 \cdot 10^{11}$. In Table 14, we list the results for H_2^+ ions assuming a partial pressure of $0.8 \cdot 10^{-9}$ mbar for H_2 molecules and in Table 15 for CO^+ ions assuming a partial pressure of $0.2 \cdot 10^{-9}$ mbar for CO molecules. We mention that a CO molecule content of about 10-20 % is always present in the UHV of storage rings.

The situation is yet worse for $1.0 \cdot 10^{10}$ antiprotons. The mean cross-field drift velocities for $1.0 \cdot 10^{10}$ antiprotons are by a factor of $10^{3/5}$=3.98 lesser[7] and the mean clearing times T_c and the resulting neutralization η are by a factor of $10^{3/5}$=3.98 larger than the values listed in Tables 14 and 15, see Tables 18 and 19.

Such neutralization levels are dangerous in view of possible coherent instabilities. In this context, it should be noted that 44 dipole magnets are installed in the HESR ring. The total length of 44 dipole magnets amounts to 184.8 m which is about one third of the circumference. A possible solution of the problem is to improve the residual vacuum substantially.

In order to counteract the trapped ion effects, it is planned to improve the residual vacuum by about a factor 100 [23]. This can be achieved by sputtering thin-film NEG[8] coatings onto the surface of the vacuum chamber and by using heating jackets along the beam tubes. The aim is to achieve residual gas pressures of about $1.0 \cdot 10^{-11}$ mbar. In Tables 16 and 17 we list the resulting neutralizations η for H_2^+ and CO^+ ions assuming $N_{\bar{p}} = 1.0 \cdot 10^{11}$ and partial pressures of $0.8 \cdot 10^{-11}$ mbar and $0.2 \cdot 10^{-11}$ mbar for H_2 and CO molecules, respectively. The corresponding results for $N_{\bar{p}} = 1.0 \cdot 10^{10}$ are listed in Tables 20 and 21.

Unfortunately, the cross-field drift velocity $v_D = E_x/B_y$ vanishes at the beam center, see next Subsection 13.2. Ions created near the beam center are not cleared. In order to avoid the build-up of a trapped ion peak in the beam center we suggest to shift the beam periodically back and forth, see Subsects. 13.3 - 13.6.

[7] $\lambda \propto N_{\bar{p}}$, $\sigma \propto N_{\bar{p}}^{2/5}$, $|\bar{v}_D| \propto N_{\bar{p}}^{3/5}$, see Subsect. 8.3.

[8] Non-Evaporating Getter Material

Table 14: Mean cross-field drift velocity $|\bar{v}_D|$, mean clearing time T_c, production time T_p and neutralization η in dipole magnets for H_2^+ ions assuming a partial $\mathbf{H}_2$ pressure of $\mathbf{0.8 \cdot 10^{-9}}$ mbar and $N_{\bar{p}} = \mathbf{1.0 \cdot 10^{11}}$.

p (GeV/c)	$\lvert\bar{v}_D\rvert$ (m/s)	T_c (s)	T_p (s)	η
1.5	51.3	0.0439	9.22	$4.29 \cdot 10^{-3}$
3.825	32.1	0.0701	9.29	$6.79 \cdot 10^{-3}$
8.889	21.1	0.107	8.69	$1.11 \cdot 10^{-2}$
15.0	16.2	0.139	7.98	$1.57 \cdot 10^{-2}$

Table 15: Mean cross-field drift velocity $|\bar{v}_D|$, mean clearing time T_c, production time T_p and neutralization η in dipole magnets for CO^+ ions assuming a partial $\mathbf{CO}$ pressure of $\mathbf{0.2 \cdot 10^{-9}}$ mbar and $N_{\bar{p}} = \mathbf{1.0 \cdot 10^{11}}$.

p (GeV/c)	$\lvert\bar{v}_D\rvert$ (m/s)	T_c (s)	T_p (s)	η
1.5	51.3	0.0439	8.50	$4.64 \cdot 10^{-3}$
3.825	32.1	0.0701	8.33	$7.57 \cdot 10^{-3}$
8.889	21.1	0.107	7.45	$1.29 \cdot 10^{-2}$
15.0	16.2	0.139	6.92	$1.81 \cdot 10^{-2}$

Table 16: Mean cross-field drift velocity $|\bar{v}_D|$, mean clearing time T_c, production time T_p and neutralization η in dipole magnets for H_2^+ ions assuming a partial $\mathbf{H}_2$ pressure of $\mathbf{0.8 \cdot 10^{-11}}$ mbar and $N_{\bar{p}} = \mathbf{1.0 \cdot 10^{11}}$.

p (GeV/c)	$\lvert\bar{v}_D\rvert$ (m/s)	T_c (s)	T_p (s)	η
1.5	51.3	0.0439	922	$4.29 \cdot 10^{-5}$
3.825	32.1	0.0701	929	$6.79 \cdot 10^{-5}$
8.889	21.1	0.107	869	$1.11 \cdot 10^{-4}$
15.0	16.2	0.139	798	$1.57 \cdot 10^{-4}$

Table 17: Mean cross-field drift velocity $|\bar{v}_D|$, mean clearing time T_c, production time T_p and neutralization η in dipole magnets for CO^+ ions assuming a partial $\mathbf{CO}$ pressure of $\mathbf{0.2 \cdot 10^{-11}}$ mbar and $N_{\bar{p}} = \mathbf{1.0 \cdot 10^{11}}$.

p (GeV/c)	$\lvert\bar{v}_D\rvert$ (m/s)	T_c (s)	T_p (s)	η
1.5	51.3	0.0439	850	$4.64 \cdot 10^{-5}$
3.825	32.1	0.0701	833	$7.57 \cdot 10^{-5}$
8.889	21.1	0.107	745	$1.29 \cdot 10^{-4}$
15.0	16.2	0.139	692	$1.81 \cdot 10^{-4}$

Table 18: Mean cross-field drift velocity $|\bar{v}_D|$, mean clearing time T_c, production time T_p and neutralization η in dipole magnets for H_2^+ ions assuming a partial $\mathbf{H}_2$ pressure of $\mathbf{0.8 \cdot 10^{-9}}$ mbar and $N_{\bar{p}} = \mathbf{1.0 \cdot 10^{10}}$.

p (GeV/c)	$\lvert\bar{v}_D\rvert$ (m/s)	T_c (s)	T_p (s)	η
1.5	12.9	0.175	9.22	$1.71 \cdot 10^{-2}$
3.825	8.07	0.279	9.29	$2.70 \cdot 10^{-2}$
8.889	5.30	0.426	8.69	$4.42 \cdot 10^{-2}$
15.0	4.07	0.553	7.98	$6.25 \cdot 10^{-2}$

Table 19: Mean cross-field drift velocity $|\bar{v}_D|$, mean clearing time T_c, production time T_p and neutralization η in dipole magnets for CO^+ ions assuming a partial **CO** pressure of $\mathbf{0.2 \cdot 10^{-9}}$ mbar and $N_{\bar{p}} = \mathbf{1.0 \cdot 10^{10}}$.

p (GeV/c)	$\lvert\bar{v}_D\rvert$ (m/s)	T_c (s)	T_p (s)	η
1.5	12.9	0.175	8.50	$1.85 \cdot 10^{-2}$
3.825	8.07	0.279	8.33	$3.01 \cdot 10^{-2}$
8.889	5.30	0.426	7.45	$5.13 \cdot 10^{-2}$
15.0	4.07	0.553	6.92	$7.20 \cdot 10^{-2}$

Table 20: Mean cross-field drift velocity $|\bar{v}_D|$, mean clearing time T_c, production time T_p and neutralization η in dipole magnets for H_2^+ ions assuming a partial $\mathbf{H}_2$ pressure of $\mathbf{0.8 \cdot 10^{-11}}$ mbar and $N_{\bar{p}} = \mathbf{1.0 \cdot 10^{10}}$.

p (GeV/c)	$\lvert\bar{v}_D\rvert$ (m/s)	T_c (s)	T_p (s)	η
1.5	12.9	0.175	922	$1.71 \cdot 10^{-4}$
3.825	8.07	0.279	929	$2.70 \cdot 10^{-4}$
8.889	5.30	0.426	869	$4.42 \cdot 10^{-4}$
15.0	4.07	0.553	798	$6.25 \cdot 10^{-4}$

Table 21: Mean cross-field drift velocity $|\bar{v}_D|$, mean clearing time T_c, production time T_p and neutralization η in dipole magnets for CO^+ ions assuming a partial **CO** pressure of $\mathbf{0.2 \cdot 10^{-11}}$ mbar and $N_{\bar{p}} = \mathbf{1.0 \cdot 10^{10}}$.

p (GeV/c)	$\lvert\bar{v}_D\rvert$ (m/s)	T_c (s)	T_p (s)	η
1.5	12.9	0.175	850	$1.85 \cdot 10^{-4}$
3.825	8.07	0.279	833	$3.01 \cdot 10^{-4}$
8.889	5.30	0.426	745	$5.13 \cdot 10^{-4}$
15.0	4.07	0.553	692	$7.20 \cdot 10^{-4}$

13.2 Vanishing of cross-field drift velocity in the beam center

The transverse electric field component E_x is zero at the beam center $x = 0$. Therefore, the cross-field drift velocity $v_D = E_x/B_y$ vanishes also at the beam center. This effect is shown for a bi-Gaussian beam distribution with $\sigma_x = \sigma_y = 1.5$ mm in Fig. 23.

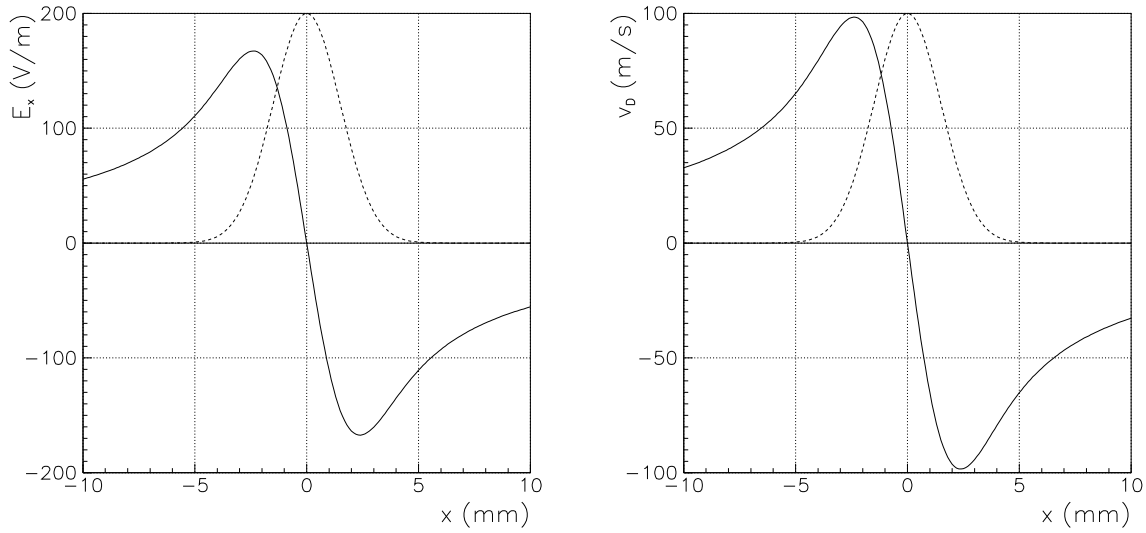

Fig. 23: Left: Electric field component E_x (solid line) of a Gaussian antiproton beam (dashhed line) with $\sigma_x = \sigma_y = 1.5$ mm and $N_{\bar{p}} = 1.0 \cdot 10^{11}$. Right: Resulting cross-field drift velocity $v_D = E_x/B_y$ with $B_y = 1.7$ T at maximum beam momentum of 15 GeV/c. Positive x values correspond to the left side of the beam.

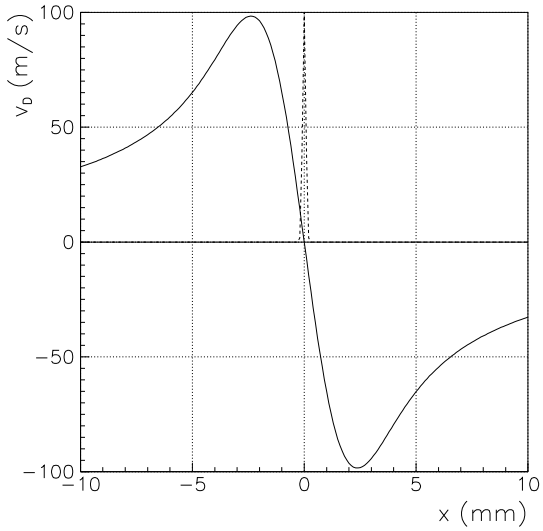

Fig. 24: Cross-field drift velocity $v_D = E_x/B_y$ (solid line) yielding a delta-function peak of trapped ions (dashhed line) in the beam center of a Gaussian antiproton beam with $\sigma_x = \sigma_y = 1.5$ mm and $N_{\bar{p}} = 1.0 \cdot 10^{11}$. Positive x values correspond to the left side of the beam.

13.3 Suppression of the ion peak in the center of dipole magnets

The absolute value of the cross-field drift velocity is very small near the beam center. It is exactly zero at the beam center. Ions created near the beam center are practically not cleared by the mechanism of the cross-field drift velocity. The continuous production of ions yields a high ion concentration near the beam center. The resulting ion distribution as a function of x looks like a delta function, see Fig. 24. Such a massive and narrow ion distribution inside the dipole magnets should be avoided since it causes highly nonlinear electric fields [27].

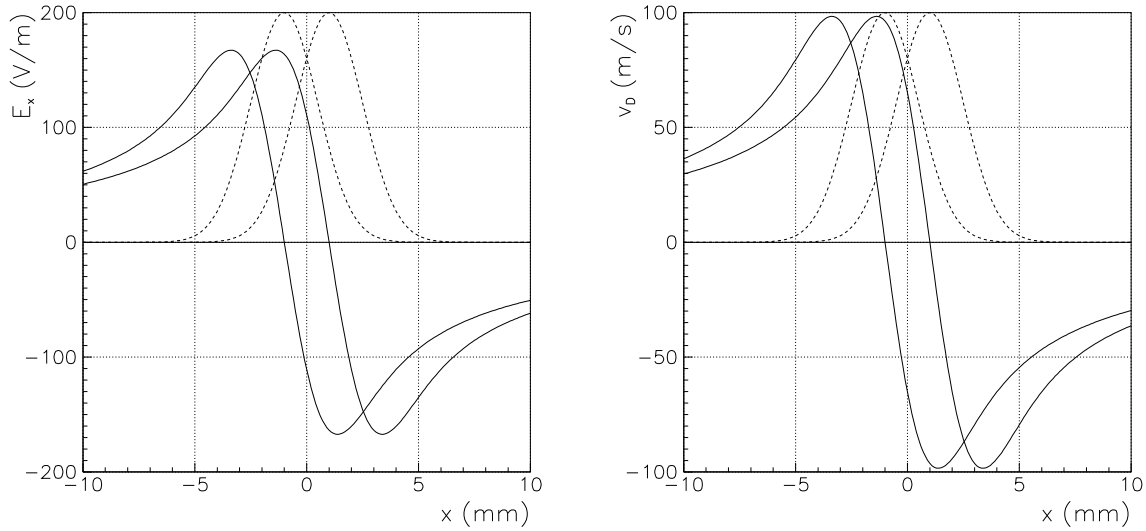

Fig. 25: Left: Electric field components E_x (solid lines) of Gaussian antiproton beams (dashhed lines) with $\sigma_x = \sigma_y = 1.5$ mm and $N_{\bar{p}} = 1.0 \cdot 10^{11}$ shifted back and forth by $\Delta x = \pm 1$ mm. Right: Resulting cross-field drift velocities $v_D = E_x/B_y$ with $B_y = 1.7$ T at maximum beam momentum of 15 GeV/c. Positive x values correspond to the left side of the beam.

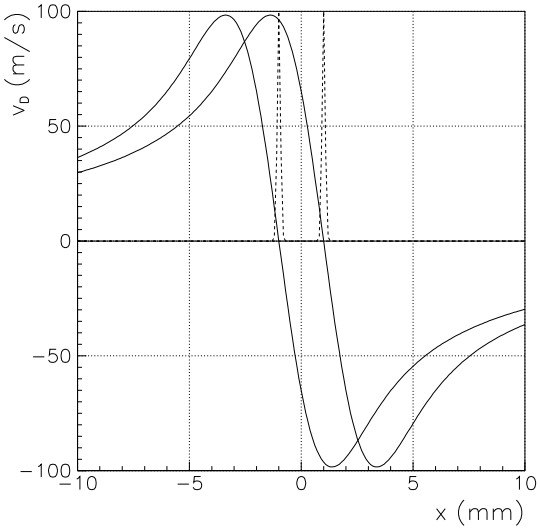

Fig. 26: Cross-field drift velocities $v_D = E_x/B_y$ (solid lines) of Gaussian antiproton beams with $\sigma_x = \sigma_y = 1.5$ mm and $N_{\bar{p}} = 1.0 \cdot 10^{11}$ shifted back and forth by by $\Delta x = \pm 1$ mm. The delta peak of trapped ions at $x = -1.0$ mm is cleared if the beam is shifted to $x = +1.0$ mm. Vice versa, the delta peak at $x = +1.0$ mm is cleared if the beam is shifted to $x = -1.0$ mm.

Therefore, we suggest to move the beam center horizontally back and forth in order to avoid the accumulation of trapped ions near $x = 0$. This can easily be achieved by local closed orbit distortions in the region of the first and second arc (North arc and South arc). The closed orbit distortion can be evaluated using the following equation,

$$x(s) = \Theta_x(s_1)\sqrt{\beta_x(s_1)\beta_x(s)}\sin\left[\psi_x(s) - \psi_x(s_1)\right]. \tag{89}$$

Here, $\Theta_x(s_1)$ is the angle kick (unit: rad) at the position of the kicker s_1 in the ring, $\beta_x(s_1)$ and $\beta_x(s)$ the corresponding horizontal betatron function at s_1 and s, respectively, and $[\psi_x(s) - \psi_x(s_1)]$ the horizontal betatron-phase advance between s_1 and s.

We suggest to produce a small angle kick $\Theta_x(s_1)$ at the entrance of the first arc using a steerer magnet located at position $s_1 = 0.990$ m. The angle kick yields a sine-like distortion of the central orbit. The resulting closed orbit distortion is canceled at the exit of the first arc by producing a small angle kick $\Theta_x(s_2)$ with a second steerer at position $s_2 = 167.656$ m. The horizontal betatron phase advance between s_1 and s_2 is exactly $6\,\pi$, see Fig. 27. The closed orbit distortion in the first arc is achieved if

$$\Theta_x(s_2) = \Theta_x(s_1)\sqrt{\beta_x(s_1)/\beta_x(s_2)}. \tag{90}$$

Similarly, we suggest to produce a small angle kick $\Theta_x(s_3)$ at the entrance of the second arc using a steerer magnet located at position $s_3 = 275.9983$ m. The angle kick yields a sine-like distortion of the central orbit. The resulting closed orbit distortion is canceled at the exit of the second arc by producing a small angle kick $\Theta_x(s_4)$ using a steerer at position $s_4 = 442.7891$ m. The horizontal betatron phase advance between s_3 and s_4 is also exactly $6\,\pi$, see Fig. 28. The closed orbit distortion in the second arc is achieved if

$$\Theta_x(s_4) = \Theta_x(s_3)\sqrt{\beta_x(s_3)/\beta_x(s_4)}. \tag{91}$$

13.4 Timing of beam shifting in the arcs

A possible timing of beam shifting in the arcs is a periodic square wave-oscillation. That means the angle kicks Θ_1 - Θ_4 are positive in the first half period and negative in the second half period. The half period $T_s/2$ for a single position should be larger than the clearing time T_c which can be achieved by the mean cross-field drift velocity $\bar{v}_D$, see Tables 16 and 17. In addition it should be shorter than the production time T_p. A reasonable timing is given if $T_s/2 = 1.0$ s yielding a frequency $f_s = 0.5$ Hz.

13.5 Estimate of beam neutralization with beam shifting in the arcs

The main effect of beam shifting in the region of the dipole magnets is to remove the delta-like peak of trapped ions in the beam center. But there is an additional advantage. The mean clearing rate $R_c = 1/T_c$ increases. This can be seen by inspecting Fig. 26. The standard mean clearing rate R_c is not affected by shifting the beam back and forth. But in addition, the delta peaks of trapped ions at $x = \pm 1.0$ mm are cleared by rather high cross-field drift velocities if the beam is shifted to $x = \mp 1.0$ mm. This additional clearing yields a substantial enhancement of the clearing rate R_c. The enhancement depends on the shift Δx and the beam width σ_x.

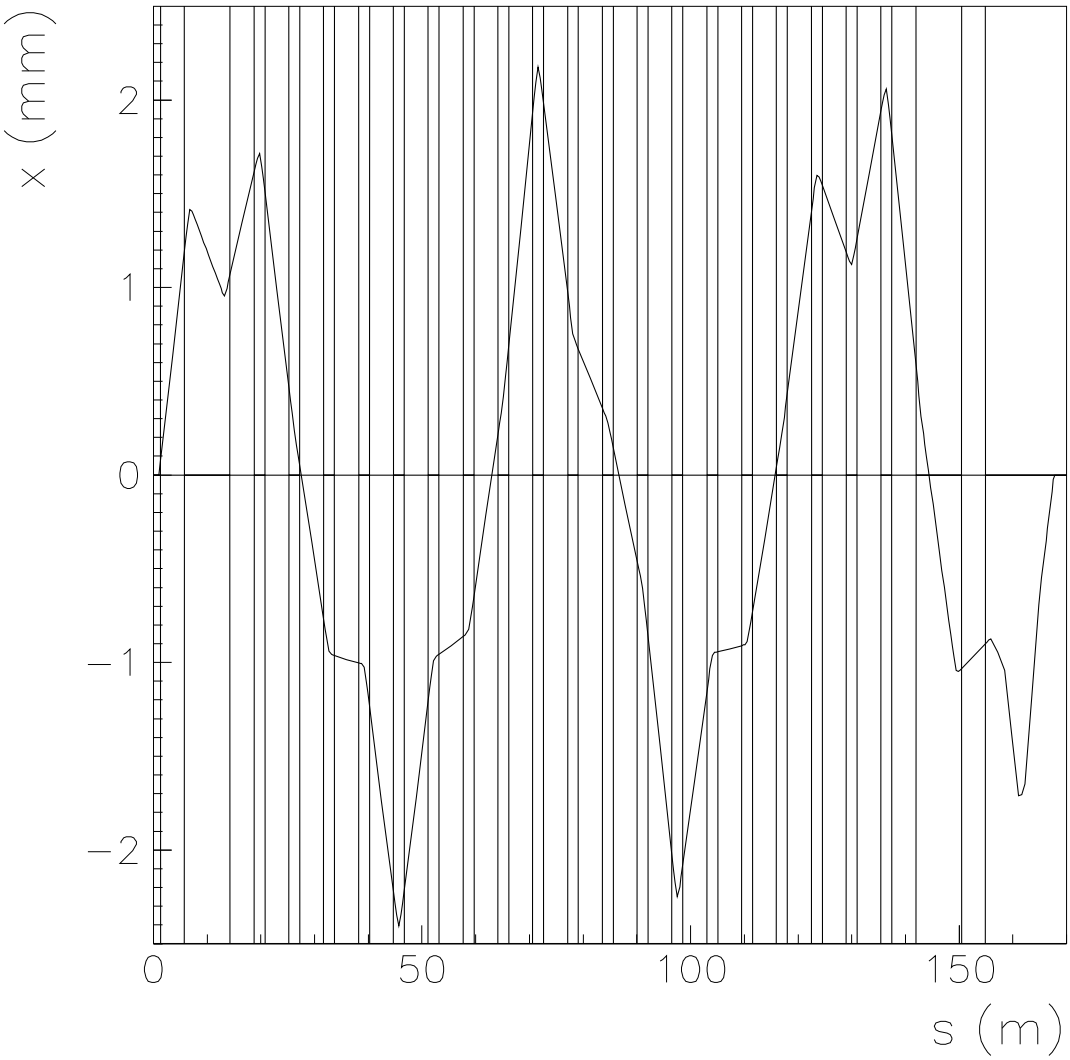

Fig. 27: Closed orbit distortion in the first arc with angle kick $\Theta_x(s_1) = 0.2500$ mrad at $s_1 = 0.9900$ m and compensation kick $\Theta_x(s_2) = 0.23843$ mrad at $s_2 = 167.6497$ m. The location of the 22 dipole magnets (4.2 m long) is indicated by the vertical bars.

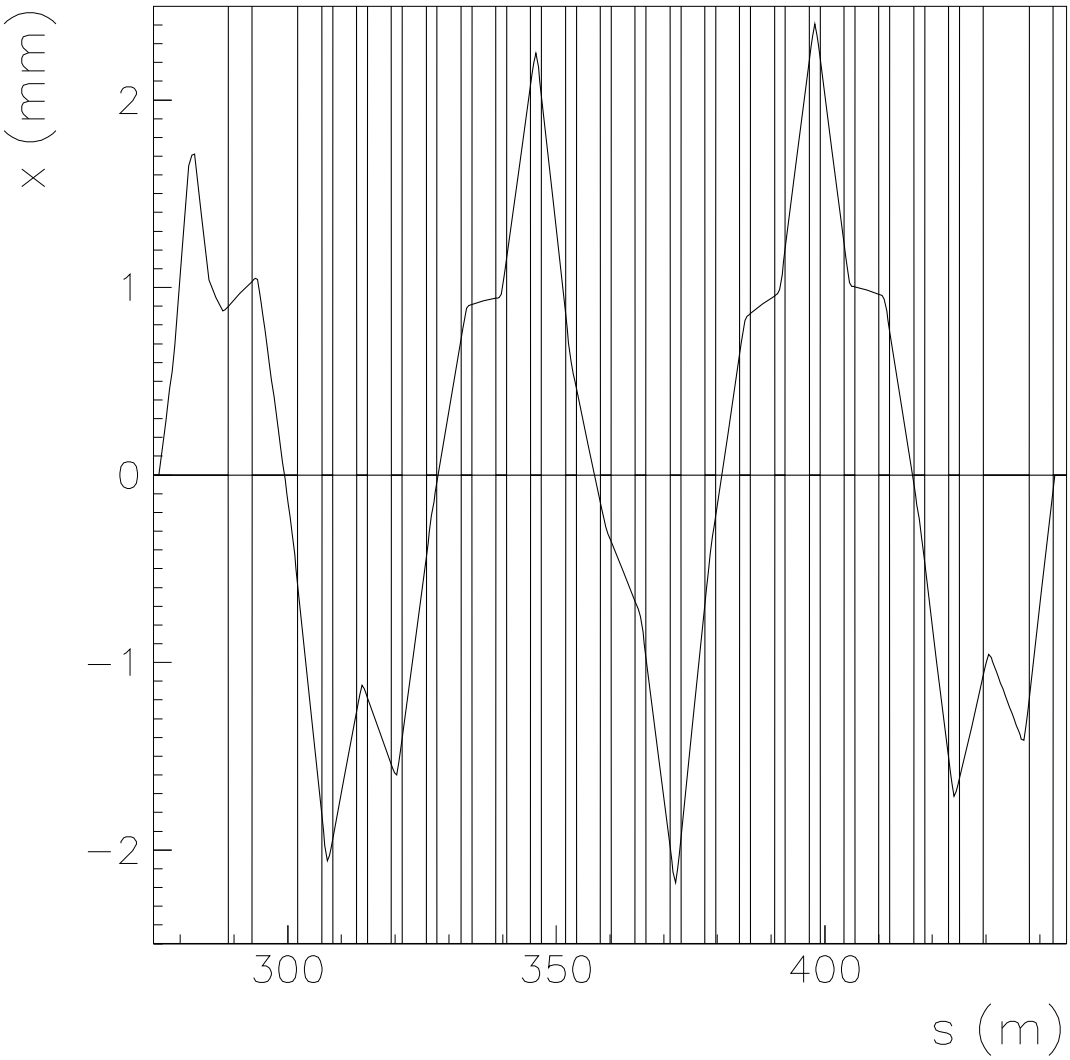

Fig. 28: Closed orbit distortion in the second arc with angle kick $\Theta_x(s_3) = 0.1958$ mrad at $s_3 = 275.9983$ m and compensation kick $\Theta_x(s_4) = 0.2500$ mrad at $s_4 = 442.7891$ m. The location of the 22 dipole magnets (4.2 m long) is indicated by the vertical bars.

13.6 Shift of zero crossings of the closed orbit distortion inside of dipole magnets

A closer look to the closed orbit distortions in Figs. 27 and 28 reveals that four zero crossings of the closed orbit distortion are located in the region of dipole magnets. In the first arc (North arc) the zero crossings are located at the entrance of dipole 4, inside of the dipoles 9 and 13 and at the exit of dipole 17. In the second arc (South arc) the zero crossings are located at the entrance of dipole 6, inside of the dipoles 10 and 14 and at the exits of dipoles 19 and 22. In order to avoid the build-up of ion peaks at those zero crossings we suggest to provide two additional closed orbit distortions where the zero crossings are shifted longitudinally.

This can be achieved in the first arc by locating the kicker 1 at $s_1 = -0.7849$ m and kicker 2 at $s_2 = 165.3395$ m, and in the second arc by locating the kicker 3 at $s_3 = 278.4395$ m and kicker 4 at $s_4 = 444.5640$ m, see Figs. 29 and 30. Comparing Figs. 27 and 28 with 29 and 30 one sees that the zero crossings inside of dipole magnets are shifted. Now, in the first arc (North arc) the zero crossings are located inside of the dipoles 3, 8, 12, 16 and at the exit of dipole 21. In the second arc (South arc) the zero crossings are located at the entrance of dipole 2 and inside of the dipoles 7, 11, 15 and 20.

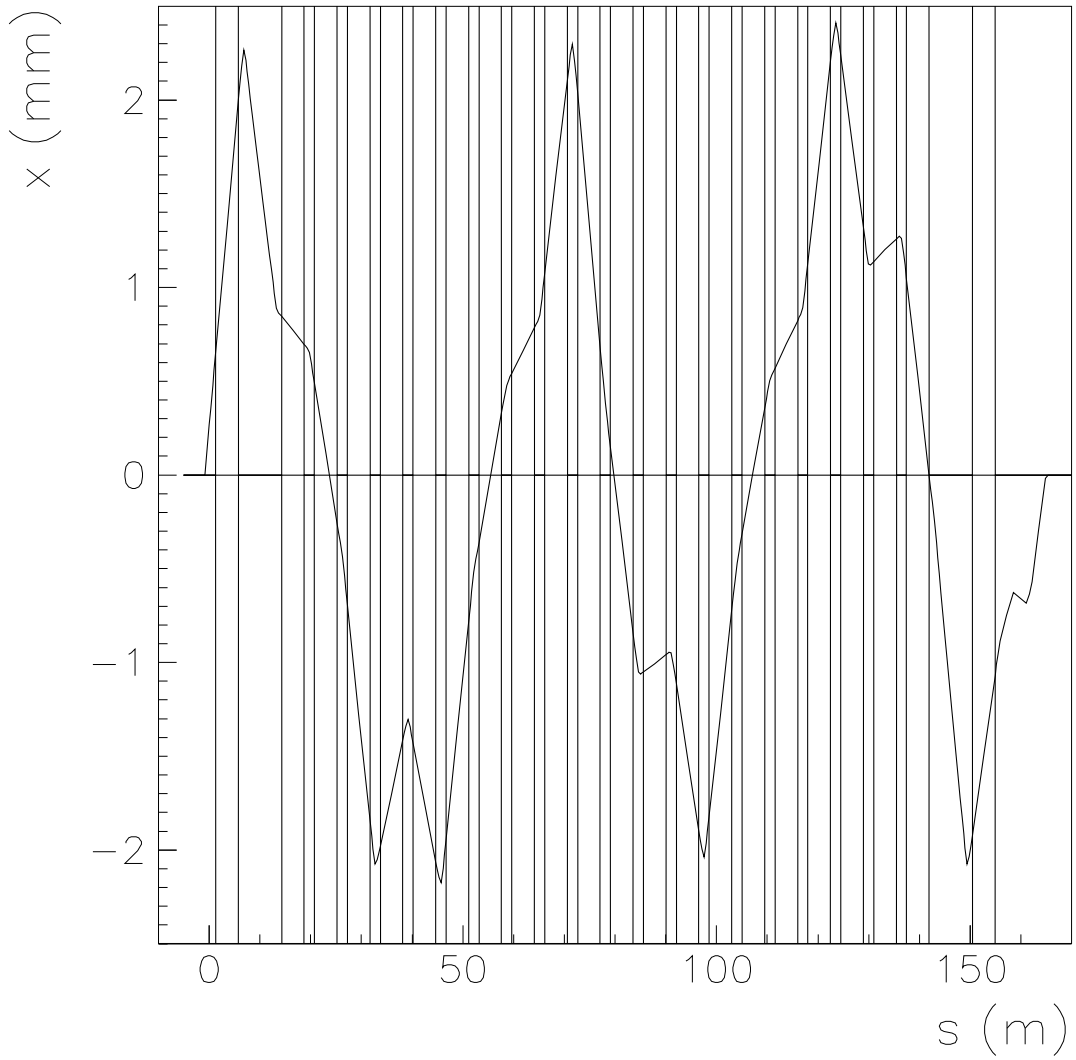

Fig. 29: Shifted closed orbit distortion in the first arc with angle kick $\Theta_x(s_1) = 0.2500$ mrad at $s_1 = -0.7849$ m and compensation kick $\Theta_x(s_2) = 0.2081$ mrad at $s_2 = 165.3396$ m. The location of the 22 dipole magnets (4.2 m long) is indicated by the vertical bars.

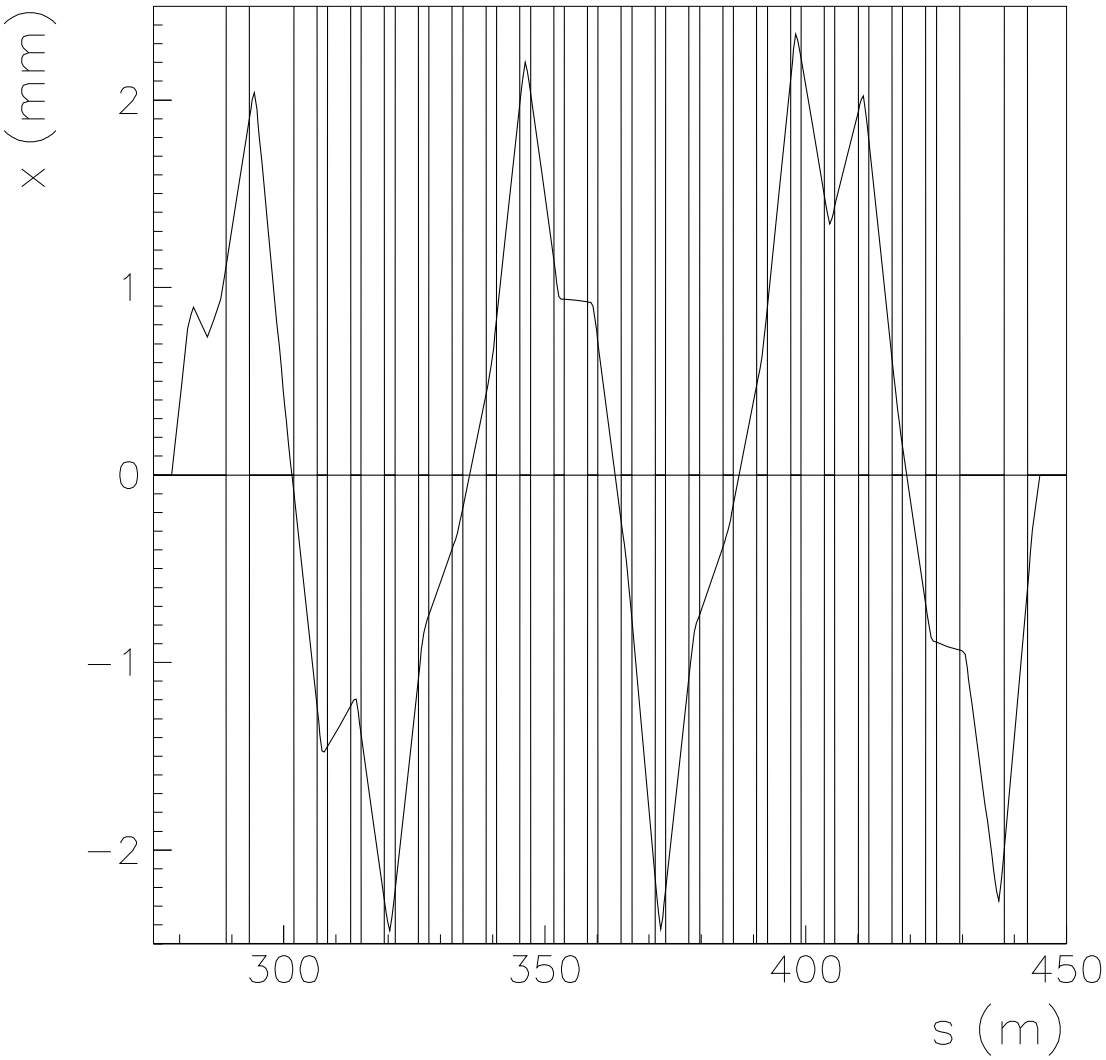

Fig. 30: Shifted closed orbit distortion in the second arc with angle kick $\Theta_x(s_3) = 0.2500$ mrad at $s_3 = 278.4395$ m and compensation kick $\Theta_x(s_4) = 0.2986$ mrad at $s_4 = 444.5640$ m. The location of the 22 dipole magnets (4.2 m long) is indicated by the vertical bars.

13.7 Ion clearing in dipole magnets by continuous clearing electrodes

The optimum solution of the trapped ion problem in dipole magnets is the installation of continuous clearing electrodes. In dipole magnets, only vertical electric fields with field components E_y along the magnetic field lines can be used in order to accelerate the trapped ions towards clearing electrodes.

As discussed in Subsect. 10.3 such clearing electrodes can be produced by plasma spraying a 0.1 mm thick and 30 mm wide Al_2O_3 layer at the bottom of the beam pipes. On top of the isolating layer a 25 mm wide highly resistive thick film coating can be applied. The clearing voltage of about -1.0 kV can be supplied by feedthrouhgs at one or both ends of the electrode. Such clearing electrodes have been developed at CERN [28, 29].

The electric field component E_y in the beam center is about -640 V/m. The estimated clearing times T_c amount to about $7.66 \cdot 10^{-7}$ s for H_2^+ ions and $2.87 \cdot 10^{-6}$ s for CO^+ ions, see Subsect. 10.6. The resulting clearing rates are so high that even UHV pressures of more than $1.0 \cdot 10^{-9}$ mbar can be tolerated, see Tables 22 and 23.

In principle, we recommend the installation of continuous clearing electrodes inside the 4.2 m long dipole magnets, even if the are not needed at the beginning. They can always be used if problems with the ultra-high vacuum occur. In the following Subsection we discuss another interesting method which can be used in order to achieve continuous ion clearing inside of the dipole magnets.

Table 22: Continuous clearing electrodes in dipole magnets: Mean clearing time T_c, production time T_p and neutralization η for H_2^+ ions assuming a partial H_2 pressure of $0.8 \cdot 10^{-9}$ mbar and $N_{\bar{p}} = 1.0 \cdot 10^{11}$.

p (GeV/c)	T_c (s)	T_p (s)	η
1.5	$7.66 \cdot 10^{-7}$	9.22	$7.48 \cdot 10^{-8}$
3.825	$7.66 \cdot 10^{-7}$	9.29	$7.42 \cdot 10^{-8}$
8.889	$7.66 \cdot 10^{-7}$	8.69	$7.93 \cdot 10^{-8}$
15.0	$7.66 \cdot 10^{-7}$	7.98	$8.64 \cdot 10^{-8}$

Table 23: Continuous clearing electrodes in dipole magnets: Mean clearing time T_c, production time T_p and neutralization η for CO^+ ions assuming a partial CO pressure of $0.2 \cdot 10^{-9}$ mbar and $N_{\bar{p}} = 1.0 \cdot 10^{11}$.

p (GeV/c)	T_c (s)	T_p (s)	η
1.5	$1.0 \cdot 10^{-6}$	8.50	$3.04 \cdot 10^{-7}$
3.825	$1.0 \cdot 10^{-6}$	8.33	$3.10 \cdot 10^{-7}$
8.889	$1.0 \cdot 10^{-6}$	7.45	$3.47 \cdot 10^{-7}$
15.0	$1.0 \cdot 10^{-6}$	6.92	$3.73 \cdot 10^{-7}$

13.8 Continuous ion clearing in dipole magnets using two half-cylinder electrodes

Another possibility to achieve continuous ion clearing in dipole magnets has been discussed during a recent meeting at FZ Jülich (03.07.2012). The idea is to cut the beam pipe along the horizontal midplane. The two halfs are joined together using a suitable dielectric as for instance a highly resistive glass insulator, see Fig. 31. Applying opposite voltages $+U_0$ and $-U_0$ yields an electric field component E_y which can be used in order to extract the ions. This technique has the additional advantage that the UHV vacuum can still be improved substantially by sputtering thin-film NEG[9] coatings onto the surface of the half cylinders and by using heating jackets along the beam tubes.

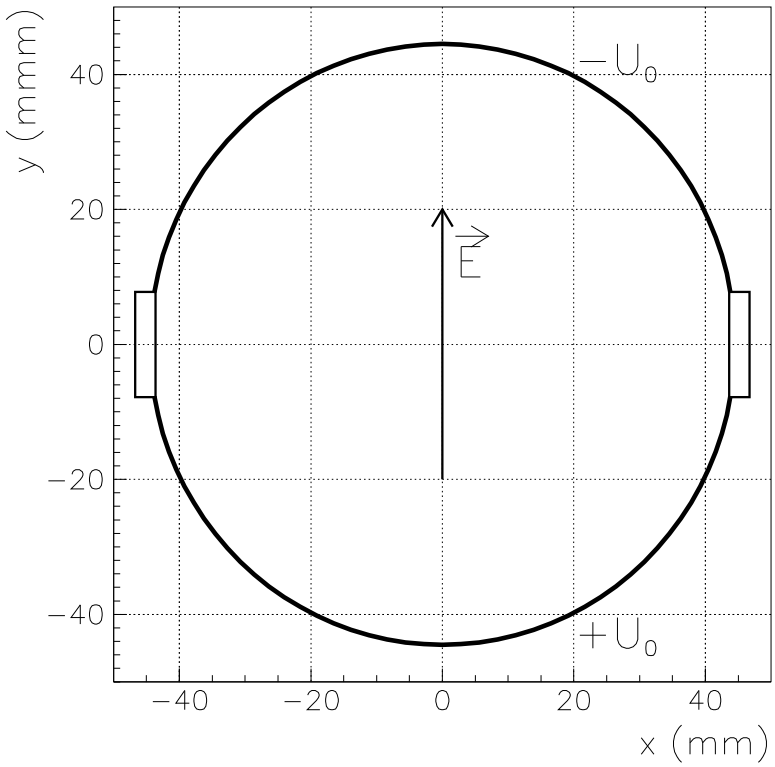

Fig. 31: Scheme of continuous ion clearing in a dipole magnet: The transverse electric field $\vec{E}$ is generated with two metallic half cylinders separated by high-resistive-glass insulators. The resulting electric field component E_y is directed along the magnetic field component B_y of the dipole magnet.

[9]Non-Evaporating Getter Material

14. Damping of Coherent Instabilities

Here, we discuss the possibility to damp the coherent instabilities which are caused by trapped ions. Transverse coherent instabilities have been observed at several antiproton machines. There, collective oscillations of the beam center (dipole mode) or the beam shape (quadrupole mode) grow exponentially due to the interaction of the beam with the trapped ions. The most dangerous mode is the dipole mode, i.e. the coherent oscillation of the beam center. The coherent instabilities can be estimated using the two-beam instability theory developed by Koshkarev and Zenkevich [10], Laslett, Sessler and Möhl [11] Keil and Zotter [12] and Alves-Pires et al. [14]. Additional information can be found in the thesis of Zhou [17] and in the references [13, 21].

Trapped ions oscillate in the electric field of the antiproton beam. They cause forces back on the beam. Vice versa, the beam disturbs the motion of the ions which interact with trailing beam particles. Thus, the beam is forced to interact coherently with itself. This phenomenon is very similar to the interaction between beam and wake fields which are described by the machine impedance $Z(\omega)$. Here, ω is the angular frequency of the resulting coherent oscillation. The effect of trapped ions can be described by some extra impedance $Z_i(\omega)$. Since the real part of $Z(\omega) + Z_i(\omega)$ is positive the fast-wave mode with the sideband frequency $\omega = (n + Q)\omega_0$ is always stable [17]. Here, ω_0 is the revolution frequency, Q the betatron tune and n an integer with $n > -Q$. Without Landau damping, i.e. without any frequency spreads the slow-wave mode with $\omega = (n - Q)\omega_0$ is always unstable. Here, n is an integer with $n > Q$. Thus, dangerous coherent oscillations can occur if the trapped ions oscillate at frequencies near the sideband frequencies $(n - Q)\omega_0$.

14.1 Ion oscillations

Ions trapped in the potential well of the antiproton beam perform oscillations. Using the linear approximation of the electric field the equation of motion reads for an ion of mass m_i and charge $Z_i e$

$$\begin{aligned} \frac{\mathrm{d}^2 x_i}{\mathrm{d}t^2} &= \frac{Z_i e}{m_i} E_x = -\frac{e^2 N_{\bar{p}}}{2\pi\epsilon_0 L_1} \frac{Z_i}{m_i} \frac{1-\eta}{\sigma_x(\sigma_x+\sigma_y)} x_i = -q_x^2 \omega_0^2 x_i \\ \frac{\mathrm{d}^2 y_i}{\mathrm{d}t^2} &= \frac{Z_i e}{m_i} E_y = -\frac{e^2 N_{\bar{p}}(1-\eta)}{2\pi\epsilon_0 L_1 m \sigma_y(\sigma_x+\sigma_y)} y_i = -q_y^2 \omega_0^2 y_i. \end{aligned} \tag{92}$$

Here, $m_i \approx A_i m_p$ is the mass of the ion and Z_i is the charge number of the ionization where $Z_i = 1$ for singly charged ions, $Z_i = 2$ for doubly charged ions and so on. The other quantities are defined in Sect. 3.. The transverse and longitudinal velocities of the ion are so small that the weak Lorentz force due to the magnetic field of the beam can be neglected. The ions perform harmonic oscillations. The frequencies f_x and f_y of the ion oscillations ('bounce frequency') read

$$\begin{aligned} f_x &= \frac{1}{2\pi}\sqrt{\frac{Z_i e^2 N_{\bar{p}}(1-\eta)}{2\pi\epsilon_0 L_1 m_i \sigma_x(\sigma_x+\sigma_y)}} = q_x f_0 \\ f_y &= \frac{1}{2\pi}\sqrt{\frac{Z_i e^2 N_{\bar{p}}(1-\eta)}{2\pi\epsilon_0 L_1 m_i \sigma_y(\sigma_x+\sigma_y)}} = q_y f_0. \end{aligned} \tag{93}$$

where η is the neutralization factor, ω_0 the angular revolution frequency and f_0 the revolution frequency of the antiprotons ($f_0 = 520.2$ kHz at 15 GeV/c) and q_x, q_y the 'tune numbers' of the

ion oscillations. These equations can also be written in the following form,

$$
\begin{aligned}
q_x^2 &= \frac{1}{\omega_0^2}\frac{Z_i e^2 N_{\bar{p}}(1-\eta)}{2\pi\epsilon_0 L_1 m_i \sigma_x(\sigma_x+\sigma_y)} = \frac{2R^2}{L_1}\frac{N_{\bar{p}} r_p}{\beta^2}\frac{Z_i}{A_i}\frac{1-\eta}{\sigma_x(\sigma_x+\sigma_y)}, \\
q_y^2 &= \frac{1}{\omega_0^2}\frac{Z_i e^2 N_{\bar{p}}(1-\eta)}{2\pi\epsilon_0 L_1 m_i \sigma_y(\sigma_x+\sigma_y)} = \frac{2R^2}{L_1}\frac{N_{\bar{p}} r_p}{\beta^2}\frac{Z_i}{A_i}\frac{1-\eta}{\sigma_y(\sigma_x+\sigma_y)}.
\end{aligned}
\tag{94}
$$

Here, $r_p = e^2/(4\pi\epsilon_0 m_p c^2) = 1.535 \cdot 10^{-18}$ m is the classical proton radius.

In the region of solenoids the ion motion is modified by the presence of the longitudinal magnetic field B. The resulting motion can be described by a superposition of a fast modified cyclotron motion around the field lines (large angular frequency ω_+ and small radius r_+) and a slow magnetron motion around the beam center (angular frequency ω_- and radius r_-), see Sect. 9.2. Direct transverse oscillations in x- and y-direction are not possible. Therefore, we set $q_x = 0$ and $q_y = 0$ in the region of solenoids.

In the region of dipole magnets the transverse ion motion in x-direction is strongly affected by the magnetic field B_y. The ions perform a fast cyclotron motion around the vertical field lines. This motion is modified by the transverse electric field component E_x of the antiproton beam. The resulting $\vec{E} \times \vec{B}/B^2$ cross-field drift velocity is directed in the longitudinal direction. A transverse oscillation in x-direction is not possible. Therefore, we set $q_x = 0$ in the region of dipole magnets.

The resulting 'tune numbers' q_x and q_y depend on the position s in the HESR ring since the rms envelopes σ_x and σ_y and the neutralization η are functions of s. The danger of coherent oscillations is especially high if the rms values of q_x and/or q_y are close to a resonance line. This occurs for instance for $q_y(\mathrm{H}^+)$ near 1.5 GeV/c, $q_x(\mathrm{H}^+)$ near 3.825 GeV/c, for $q_y(\mathrm{H}_2^+)$ near 3.825 GeV/c and for $q_x(\mathrm{H}_2^+)$ near 8.889 GeV/c. The 'tune numbers' of CO^+ ions are always below the critical resonance lines $(8 - Q_x)$ and $(8 - Q_y)$.

We note that the 'tune numbers' q_x and q_y depend not only on the ion mass, ion charge and beam momentum but also on the number of stored antiprotons and the neutralization η which determine the depth of the potential well and the electric field strengths E_x and E_y. The 'tune numbers' $q_{x,y}$ are proportional to $\sqrt{N_{\bar{p}}/[\sigma_{x,y}(\sigma_x+\sigma_y)]}$. The beam widths $\sigma_{x,y}$ are proportional to $N_{\bar{p}}^{2/5}$ (see Sect. 2.). Therefore, we get $q_{x,y} \propto \sqrt{N_{\bar{p}}^{1/5}}$, and the 'tune numbers' for $1.0 \cdot 10^{10}$ antiprotons are by a factor $\sqrt{10^{1/5}} = 1.26$ lower than those for $1.0 \cdot 10^{11}$ antiprotons.

We mention that the bounce frequencies of the trapped ions decrease with increasing oscillation amplitude. This effect is due to the nonlinearity of the electric field of a Gaussian beam distribution. The non-linear detuning of the ion bounce frequency plays an important role when resonant transverse shaking is applied in order to remove the ions out of the beam (see Sect. 15.).

14.2 Formalism of coherent instabilities

Here, we sketch the formalism of coherent oscillations of the $\bar{p}$-beam and trapped ions, see Refs. [13, 14, 21]. Because beam instabilities develop on a time scale much larger than the revolution period, the theoretical description of coupled oscillations can be simplified by introducing ring-averaged forces. Usually, the ring-averaged forces are calculated assuming a constant neutralization η in the ring and using a smooth approximation for the envelopes, $\sigma_x = \sqrt{\epsilon_x \langle\beta_x\rangle}$ and $\sigma_y = \sqrt{\epsilon_y \langle\beta_y\rangle}$ with $\langle\beta_x\rangle = R/Q_x$ and $\langle\beta_y\rangle = R/Q_y$. However, in the HESR ring the neutral-

ization η depends strongly on the position s due to the large pressure bump in the vicinity of the PANDA target. Also the envelopes depend strongly on the position s due to the low beta values at the PANDA target and the large beta values in the region of the electron-cooler. Therefore, the HESR ring is segmented in small sections and the ring-averaged forces are numerically evaluated.

In the following we write the coupled equations for coherent oscillations in the y-direction and we omit the index y for the characteristic forces F_β, F_{sc}, F_c, $F_{i,sc}$ and $F_{i,c}$ and the related quantities Q_0^2, Q_{sc}^2, Q_c^2, q_{sc}^2 and q_c^2. Similar equations can be written for the coupled oscillations in x-direction.

The model for coupled oscillations yields the following coupled equations for the motion of an individual antiproton (y) and ion (y_i),

$$\gamma m_{\bar{p}} \frac{\mathrm{d}^2 y}{\mathrm{d}t^2} = \langle F_\beta \rangle + \langle F_{sc} \rangle + \langle F_c \rangle, \tag{95}$$

$$m_i \frac{\mathrm{d}^2 y_i}{\mathrm{d}t^2} = \langle F_{i,sc} \rangle + \langle F_{i,c} \rangle. \tag{96}$$

Here, $\langle F_\beta \rangle$ represents the external focusing forces of the betatron oscillation, $\langle F_{sc} \rangle$ the $\bar{p}$ space-charge forces acting on the $\bar{p}$ beam particles, $\langle F_c \rangle$ the trapped ion space-charge forces acting on the $\bar{p}$ beam particles, $\langle F_{i,sc} \rangle$ the trapped ion space-charge forces acting on the ions and $\langle F_{i,c} \rangle$ the $\bar{p}$ space-charge forces acting on the ions. We note that space charge image forces are neglected. These equations are rewritten by introducing the tune number Q_0 of the unperturbed betatron oscillation and the 'tune numbers' Q_{sc}, Q_c, q_{sc} and q_c. The ring averaged forces are represented by the corresponding 'tune numbers' times the angular frequency ω_0 of the beam using the following definitions

$$\begin{aligned}
\frac{\langle F_\beta \rangle}{\gamma m_{\bar{p}}} &= Q_0^2 \omega_0^2 \, y, \\
\frac{\langle F_{sc} \rangle}{\gamma m_{\bar{p}}} &= Q_{sc}^2 \omega_0^2 \, (y - \bar{y}), \\
\frac{\langle F_c \rangle}{\gamma m_{\bar{p}}} &= Q_c^2 \omega_0^2 \, (y - \bar{y}_i), \\
\frac{\langle F_{i,sc} \rangle}{m_i} &= q_{sc}^2 \omega_0^2 \, (y_i - \bar{y}_i), \\
\frac{\langle F_{i,c} \rangle}{m_i} &= q_c^2 \omega_0^2 \, (y_i - \bar{y}).
\end{aligned} \tag{97}$$

Thus, the model for linearized coupled oscillations as described in [14] yields the following coupled equations for the dipole mode.

$$\frac{1}{\omega_0^2} \frac{\mathrm{d}^2 y}{\mathrm{d}t^2} + Q_0^2 \, y - Q_{sc}^2 (y - \bar{y}) + Q_c^2 (y - \bar{y}_i) = 0, \tag{98}$$

$$\frac{1}{\omega_0^2} \frac{\mathrm{d}^2 y_i}{\mathrm{d}t^2} - q_{sc}^2 (y_i - \bar{y}_i) + q_c^2 (y_i - \bar{y}) = 0. \tag{99}$$

The external focusing forces are represented by the squared tune Q_0^2 of the unperturbed betatron oscillation. The other forces are represented by the corresponding mean squared 'tune

numbers',

$$Q_{sc}^2 = 2\frac{R^2}{L_1}\frac{N_{\bar{p}} r_p}{\beta^2\gamma^3}\left\langle \frac{1}{\sigma_y(s)(\sigma_x(s)+\sigma_y(s))}\right\rangle, \quad \bar{p} \text{ space charge acting on } \bar{p}, \tag{100}$$

$$Q_c^2 = 2\frac{R^2}{L_1}\frac{N_{\bar{p}} r_p}{\beta^2\gamma}\left\langle \frac{\eta(s)}{\sigma_y(s)(\sigma_x(s)+\sigma_y(s))}\right\rangle, \quad \text{ion space charge acting on } \bar{p}, \tag{101}$$

$$q_{sc}^2 = 2\frac{R^2}{L_1}\frac{N_{\bar{p}} r_p Z_i}{\beta^2 A_i}\left\langle \frac{\eta(s)}{\sigma_y(s)(\sigma_x(s)+\sigma_y(s))}\right\rangle, \quad \text{ion space charge acting on ion}, \tag{102}$$

$$q_c^2 = 2\frac{R^2}{L_1}\frac{N_{\bar{p}} r_p Z_i}{\beta^2 A_i}\left\langle \frac{1}{\sigma_y(s)(\sigma_x(s)+\sigma_y(s))}\right\rangle, \quad \bar{p} \text{ space charge acting on ion}. \tag{103}$$

Here, Z_i is the charge number of the ion, A_i the mass number and r_p the classical proton radius. We assume that the neutralization $\eta(s)$ is dominated by singly charged H_2^+ ions. The coherent transverse motion of the ions is fixed in space and oscillates only in time. The coherent transverse motion of the $\bar{p}$ beam particles is oscillating in space and in time like a travelling wave. We are interested in resonant harmonics of coupled oscillations of the beam centers $\bar{y}$ and $\bar{y}_i$. To this end, we make the following ansatz,

$$\bar{y} = a\exp[i\,(k\,s-\omega\,t)] = a\exp[i\,(\frac{n}{R}\,s-\omega\,t)] \tag{104}$$

$$\bar{y}_i = a_i\exp\,[-i\omega t], \tag{105}$$

Here, the resonance condition imposes that the wave number k and the wave length λ of the travelling wave satisfy the resonance condition

$$k=\frac{n}{R}, \qquad \lambda=\frac{C}{n}. \tag{106}$$

where n is an integer, C the circumference and $R=C/(2\pi)$ the effective 'radius' of the machine. The substitution of $\bar{y}$ and $\bar{y}_i$ from (104) and (105) into (98) and (99) gives two equations,

$$\frac{1}{\omega_0^2}\frac{\mathrm{d}^2\bar{y}}{\mathrm{d}t^2} + (Q_0^2+Q_c^2)\,\bar{y} = Q_c^2\,\bar{y}_i, \tag{107}$$

$$\frac{1}{\omega_0^2}\frac{\mathrm{d}^2\bar{y}_i}{\mathrm{d}t^2} + q_c^2\,\bar{y}_i = q_c^2\,\bar{y}. \tag{108}$$

Since the $\bar{p}$ oscillations are oscillating in space (s) and time (t) (travelling wave ansatz, see Eq. (104)) the total differential $\mathrm{d}/\mathrm{d}t$ in the $\bar{p}$ equation of motion (98) must be written

$$\frac{\mathrm{d}}{\mathrm{d}t}=\left(\frac{\partial}{\partial t}+\frac{\partial}{\partial s}\dot{s}\right). \tag{109}$$

Inserting the travelling wave ansatz (104) yields

$$\frac{\mathrm{d}\bar{y}}{\mathrm{d}t} = \left(-i\omega+i\frac{n}{R}\dot{s}\right)\bar{y} = i(-\omega+n\omega_0)\bar{y},$$

$$\frac{\mathrm{d}^2\bar{y}}{\mathrm{d}t^2} = -(n\omega_0-\omega)^2\bar{y}. \tag{110}$$

Similarly, we get

$$\frac{\mathrm{d}^2\bar{y}_i}{\mathrm{d}t^2} = -\omega^2\bar{y}_i. \tag{111}$$

Using these relations in (107) and (108) yields

$$\left[-\frac{(n\omega_0-\omega)^2}{\omega_0^2}+(Q_0^2+Q_c^2)\right]\bar{y} = Q_c^2\bar{y}_i, \tag{112}$$

$$\left[-\frac{\omega^2}{\omega_0^2}+q_c^2\right]\bar{y}_i = q_c^2\bar{y}. \tag{113}$$

Eliminating $\bar{y}$ and $\bar{y}_i$ yields an equation for the angular frequency ω of the coherent oscillation. Introducing the reduced frequency $w=\omega/\omega_0$ the resulting equation may be written

$$(q_c^2-w^2)[(Q_0^2+Q_c^2)-(n-w)^2]-q_c^2Q_c^2=0. \tag{114}$$

In this equation, n, q_c, Q_c and Q_0 are the parameters and w is the unknown. Stable solutions occur if w becomes real, i.e. if ω becomes real. If w is complex the solutions come in pairs, one with a negative imaginary part corresponding to a damping of the oscillations and one with a positive imaginary part corresponding to a growing (anti-damping) of the oscillations which means instability!

Since $Q_c \ll Q_0$, we can ignore it in the sum $(Q_0^2+Q_c^2)$ or slightly shift the value of Q_0 by introducing $Q^2=(Q_0^2+Q_c^2)$. Unstable values (complex w) can occur if q_c is close to a sideband frequency $(n-Q)$, i.e. $q_c \cong (n-Q)$ and $w \cong (n-Q)$. Replacing w by $w=(n-Q)+\delta$ yields an equation quadratic in δ,

$$\delta^2+[(n-Q)-q_c]\delta+\frac{q_c^2Q_c^2}{4q_cQ}\cong 0. \tag{115}$$

The solution reads

$$\delta=-\frac{(n-Q)-q_c}{2}\pm\sqrt{\left(\frac{(n-Q)-q_c}{2}\right)^2-\frac{q_c^2Q_c^2}{4q_cQ}}. \tag{116}$$

Thus, the equation yields complex solutions if

$$|(n-Q)-q_c|<\frac{q_cQ_c}{\sqrt{q_cQ}}. \tag{117}$$

This equation defines a band δQ for q_c in the vicinity of $(n-Q)$,

$$\delta Q=\frac{q_cQ_c}{\sqrt{q_cQ}}, \tag{118}$$

where instability can occur, i.e. where the solution $\omega=Re(\omega)+iIm(\omega)$ has a positive imaginary part.

The fastest growth rate occurs in the center of the band where $|(n-Q)-q_c|=0$. There, we get $Re(\omega)=(n-Q)\omega_0$ and $Im(\omega)=(\omega_0/2)(q_cQ_c)/\sqrt{q_cQ}$. Thus. the fastest growth rate reads

$$\frac{1}{\tau}=\frac{\omega_0}{2}\frac{q_cQ_c}{\sqrt{q_cQ}}. \tag{119}$$

14.3 Landau damping of coherent instabilities

The coherent instability can be suppressed by Landau damping. We denote the $\bar{p}$ tune spread by $\Delta_{\bar{p}}$ and the ion oscillation tune spread Δ_i. Landau damping works if the following three conditions are fulfilled simultaneously,

$$\Delta_{\bar{p}} > \left| \frac{Q_{sc}^2}{Q} \right|, \tag{120}$$

$$\Delta_i > \left| \frac{q_{sc}^2}{q} \right|, \tag{121}$$

$$\Delta_{\bar{p}} \Delta_i > \left| \frac{q_c^2 Q_c^2}{qQ} \right|. \tag{122}$$

Here, the space charge effects are taken into account in the definition of the betatron tune Q and the ion bounce frequency q, $Q^2 = Q_0^2 + Q_c^2 - Q_{sc}^2$ and $q^2 = q_c^2 - q_{sc}^2$. We emphasize that the suppression of the two-beam instability requires that the product of the two tune spreads is larger than the right side of Eq. (122).

Including also the possibility of quadrupole modes, it is found that the risk of transverse instabilities exists in a band around the resonance line $(n - Q)$ given by

$$\delta Q = p \frac{q_c Q_c}{\sqrt{q_c Q}}, \tag{123}$$

where $p = 1$ for a dipole mode, $p = 1/2$ for a symmetric ($\zeta = \xi$) quadrupole mode and $p = 1/4$ for an antisymmetric ($\zeta = -\xi$) quadrupole mode. The width of this band reflects the risk of instability. It is proportional to Q_c, i.e. to the square root of the averaged neutralization $\sqrt{\langle \eta / [\sigma_y (\sigma_x + \sigma_y)] \rangle}$ (see Eq. (101)). It is narrower for quadrupole modes than for dipole modes. Including the possibility of quadrupole modes, the necessary condition for Landau damping reads

$$\Delta_{\bar{p}} > p \left| \frac{Q_{sc}^2}{Q} \right|, \tag{124}$$

$$\Delta_i > p \left| \frac{q_{sc}^2}{q} \right|, \tag{125}$$

$$\Delta_{\bar{p}} \Delta_i > p^2 \left| \frac{q_c^2 Q_c^2}{qQ} \right|. \tag{126}$$

14.4 Numerical results

The HESR tune is $Q \cong 7.6$ ($Q_x = 7.5995$ and $Q_y = 7.6216$). For $n = 8$ we get the smallest value of $(n - Q_x)$ as 0.4005 which defines the 'tune number' $q_{c,x}$ where instability can occur. For $n = 9$, $n = 10$, etc. we get $(n - Q_x)$ as 1.4005, 2.4005, etc.. Similarly, for $n = 8$ we get the smallest value of $(n - Q_y)$ as 0.3784 which defines the 'tune number' $q_{c,y}$ where instability can occur. For $n = 9$, $n = 10$, etc. we get $(n - Q_y)$ as 1.3784, 2.3784, etc..

The occurrence of coherent oscillations depends critically on the neutralization of the beam by trapped ions. The coupling between beam and ions is determined by Q_c^2 which depends on the neutralization η (see Eq. (101)). The characteristic quantities i.e. the ring-averaged 'tune numbers' $q = \sqrt{q_c^2 - q_{sc}^2}$ and Q_c of ion and $\bar{p}$ bounce frequencies, the bandwidth δQ and the

difference $\Delta = |(8 - Q) - q| - \delta Q$ are listed in Tables 24-27 for H^+ and H_2^+ ions and four beam momenta. The danger of an unstable coherent oscillation is given in regions where q is near a resonance line $(8 - Q)$. Then, the difference $|(8 - Q) - q|$ can be very small. The risk of instability is given if q lies within the resonance band $(8-Q)\pm\delta Q$, i.e. if $\Delta = |(8-Q)-q|-\delta Q$ is negative. This occurs in our examples for q_x and H^+ ions near 3.825 GeV/c and for q_x and H_2^+ ions near 8.889 GeV/c. In this context we note that $\Delta_y \approx 0$ for H^+ ions near 1.5 GeV/c and H_2^+ ions near 3.825 GeV/c, that means q_y is very near to the resonance line $(8 - Q_y)$.

We note that the 'tune numbers' q_x and q_y of the ion oscillations depend on the number $N_{\bar{p}}$ of stored antiprotons. For instance, they are by a factor $\sqrt{10^{1/5}} = 1.26$ lower for $N_{\bar{p}} = 1.0 \cdot 10^{10}$, see Subsect. 14.1. Therefore, the occurence of unstable coherent oscillations depends also on the number of stored antiprotons.

Finally, we note that the ion bounce frequencies for N_2^+ and/or CO^+ ions are always below the critical resonance lines $(8 - Q_x)$ and $(8 - Q_y)$.

Table 24: Ring-averaged 'tune numbers' $q_x = \sqrt{q_{c,x}^2 - q_{sc,x}^2}$ and $Q_{c,x}$ of ion and $\bar{p}$ bounce frequencies, the bandwidth δQ_x and the difference $\Delta_x = |(8 - Q_x) - q_{c,x}| - \delta Q_x$ for **coherent H^+ oscillations in x-direction** assuming $N_{\bar{p}} = 1.0 \cdot 10^{11}$, a beam-free gap of 10 % and the standard optics.

p (GeV/c)	q_x	$Q_{c,x}$	δQ_x	Δ_x
1.500	0.282	0.0662	0.0128	0.106
3.825	0.393	0.0618	0.0141	-0.00615
8.889	0.582	0.0614	0.0170	0.165
15.00	0.754	0.0616	0.0194	0.334

Table 25: Ring-averaged 'tune numbers' $q_y = \sqrt{q_{c,y}^2 - q_{sc,y}^2}$ and $Q_{c,y}$ of ion and $\bar{p}$ bounce frequencies, the bandwidth δQ_y and the difference $\Delta_y = |(8 - Q_y) - q_{c,y}| - \delta Q_y$ for **coherent H^+ oscillations in y-direction** assuming $N_{\bar{p}} = 1.0 \cdot 10^{11}$, a beam-free gap of 10 % and the standard optics.

p (GeV/c)	q_y	$Q_{c,y}$	δQ_y	Δ_y
1.500	0.401	0.0722	0.0166	0.00597
3.825	0.558	0.0674	0.0182	0.162
8.889	0.829	0.0669	0.0221	0.428
15.00	1.07	0.0671	0.0252	0.669

Table 26: Ring-averaged 'tune numbers' $q_x = \sqrt{q_{c,x}^2 - q_{sc,x}^2}$ and $Q_{c,x}$ of ion and $\bar{p}$ bounce frequencies, the bandwidth δQ_x and the difference $\Delta_x = |(8 - Q_x) - q_{c,x}| - \delta Q_x$ for **coherent $\mathbf{H_2^+}$ oscillations in x-direction** assuming $N_{\bar{p}} = 1.0 \cdot 10^{11}$, a beam-free gap of 10 $\%$ and the standard optics.

p (GeV/c)	q_x	$Q_{c,x}$	δQ_x	Δ_x
1.500	0.199	0.0662	0.0107	0.190
3.825	0.278	0.0618	0.0118	0.111
8.889	0.412	0.0614	0.0143	-0.00299
15.00	0.533	0.0616	0.0163	0.116

Table 27: Ring-averaged 'tune numbers' $q_y = \sqrt{q_{c,y}^2 - q_{sc,y}^2}$ and $Q_{c,y}$ of ion and $\bar{p}$ bounce frequencies, the bandwidth δQ_y and the difference $\Delta_y = |(8 - Q_y) - q_{c,y}| - \delta Q_y$ for **coherent $\mathbf{H_2^+}$ oscillations in y-direction** assuming $N_{\bar{p}} = 1.0 \cdot 10^{11}$, a beam-free gap of 10 $\%$ and the standard optics.

p (GeV/c)	q_y	$Q_{c,y}$	δQ_y	Δ_y
1.500	0.283	0.0722	0.0139	0.0810
3.825	0.395	0.0674	0.0153	0.000933
8.889	0.586	0.0669	0.0186	0.189
15.00	0.759	0.0671	0.0212	0.359

14.5 Risk of coherent instabilities

The risk of instability depends on the beam neutralization η. This is due to fact that the coupling strength Q_c^2 and the resulting band width δQ for unstable oscillations depend on the neutralization η. We mention that instabilities at low sideband frequencies are the most unstable modes because the frequency spreads are low. Thus, it is difficult to fulfill the conditions for the Landau damping of those instabilities [18]. Therefore, dipole instabilities driven by H^+ ions and H_2^+ ions occur already at very low neutralization levels ($\eta < 0.01$). It has been observed that the neutralization from a single trapped-ion pocket created by a localized vacuum chamber enlargement, may be sufficient to drive an instability [18, 45].

14.6 Damping of instabilities using feedback systems

Finally, we note that instabilities caused by ions can be effectively damped by transverse feedback systems using a highly sensitive resonant pick-up tuned at the frequency of the single unstable mode [17, 18]. At the cooler synchrotron COSY a broad band feedback system has been developed in order to damp transverse instabilities of electron cooled beams [46, 47]. The effect of the damping system can be measured by it's damping time τ. An oscillation with an initial amplitude A will be damped by the damper system as $A\exp(-t/\tau)$. As long as the damping time τ is less than the growing time of the instability, the beam can be stabilized [17].

15. Beam Shaking

The beam shaking can be used in order to remove trapped ions and to decrease the neutralization η and the coupling strength Q_c^2 for coherent oscillations in regions where the clearing electrodes cannot remove trapped ions sufficiently. The $\bar{p}$ beam is shaken using an RF electric field and the $\bar{p}$ beam shakes the ions. This method works if the shaking frequency is close to one of the side-band frequencies $(n-Q)\omega_0$ ('slow wave' frequency) or $(n+Q)\omega_0$ ('fast wave' frequency) and close to the ion bounce frequency $q_c\omega_0$. This condition corresponds to the resonance condition for coherent oscillations of beam and trapped ions as discussed in Sect. 14.2.

15.1 Formalism

We start with the coupled equations of motion (98) and (99) of beam and trapped ions in Sect. 14.2. We extend this equation by adding the force term of the shaking kicker $F\exp[-i\omega t]$,

$$\frac{1}{\omega_0^2}\frac{\mathrm{d}^2 y}{\mathrm{d}t^2} + Q_0^2\, y - Q_{sc}^2(y-\bar{y}) + Q_c^2(y-\bar{y}_i) = F\exp[-i\omega t]. \tag{127}$$

$$\frac{1}{\omega_0^2}\frac{\mathrm{d}^2 y_i}{\mathrm{d}t^2} - q_{sc}^2(y_i-\bar{y}_i) + q_c^2(y_i-\bar{y}) = 0. \tag{128}$$

The force term F on the r.h.s of (127) represents the shaking kicker assumed to be a δ function in azimuth. The integrated electric field $E_0\Delta s\exp[-i\omega t]$ enters as (see Refs. [14, 19])

$$F\exp[-i\omega t] = \frac{eE_0\Delta s\exp[-i\omega t]}{m_{\bar{p}}\gamma\omega_0^2}\,\delta(s) = \frac{\Delta s}{C}\frac{eE_0}{m_{\bar{p}}\gamma\omega_0^2}\sum_{n=-\infty}^{n=+\infty}\exp[in\frac{s}{R} - i\omega t]. \tag{129}$$

Only the resonant harmonic with $\omega \approx (n\pm Q)\omega_0 \approx q_c\omega_0$ is retained yielding

$$F = \frac{\Delta s}{C}\frac{eE_0}{m_{\bar{p}}\gamma\omega_0^2}\exp[in\frac{s}{R}]. \tag{130}$$

We are interested in the resonant excitation of coupled oscillations of the beam centers $\bar{y}$ and $\bar{y}_i$. As in Sect. 14.2, we make the following ansatz for the coupled motion of the beam and ion centers,

$$\bar{y} = a\exp[i\,(k\,s-\omega\,t)] = a\exp[i\,(n\,\frac{s}{R}-\omega\,t)] \tag{131}$$

$$\bar{y}_i = a_i\exp[-i\omega t], \tag{132}$$

The substitution of $\bar{y}$ and $\bar{y}_i$ from (131) and (132) into (127) and (128) yields two equations,

$$[-(n\omega_0-\omega)^2 + (Q_0^2+Q_c^2)\omega_0^2]\,\bar{y} - Q_c^2\omega_0^2\bar{y}_i = \omega_0^2 F\exp[-i\omega t], \tag{133}$$

$$(-\omega^2+q_c^2\omega_0^2)\,\bar{y}_i - q_c^2\omega_0^2\bar{y} = 0. \tag{134}$$

Using these relations and defining $Q^2=(Q_0^2+Q_c^2)$, we get the equations of the forced oscillation of two coupled oscillators,

$$\bar{y} = \frac{-\omega^2+q_c^2\omega_0^2}{[-(n\omega_0-\omega)^2+Q^2\omega_0^2](-\omega^2+q_c^2\omega_0^2) - q_c^2Q_c^2\omega_0^4}\omega_0^2 F\exp[-i\omega t], \tag{135}$$

$$\bar{y}_i = \frac{q_c^2\omega_0^2}{[-(n\omega_0-\omega)^2+Q^2\omega_0^2](-\omega^2+q_c^2\omega_0^2) - q_c^2Q_c^2\omega_0^4}\omega_0^2 F\exp[-i\omega t]. \tag{136}$$

Introducing the reduced frequency $w = \omega/\omega_0$ these equations may be written

$$\bar{y} = -\frac{w^2 - q_c^2}{(w^2 - q_c^2)[(n-w)^2 - Q^2] - q_c^2 Q_c^2} F \exp[-i\omega t], \tag{137}$$

$$\bar{y}_i = \frac{q_c^2}{(w^2 - q_c^2)[(n-w)^2 - Q^2] - q_c^2 Q_c^2} F \exp[-i\omega t]. \tag{138}$$

It is interesting to note that the denominator in those equations is equal to the l.h.s. of the important equation (114). Shaking works if the amplitude of $\bar{y}_i$ becomes large, i.e. when the denominator approaches zero. Here, we must consider the non-linear detuning and the condition for the so-called 'lock-on' of the ions onto the resonance. With increasing amplitudes the bounce frequency q_c of the ions decreases. Thus, $(w^2 - q_c^2)$ is positive and increases. As a consequence, in order to achieve a denominator approaching zero, $[(n-w)^2 - Q^2]$ must also be positive and the condition for $\bar{y}_i$ becoming large may be written

$$(w^2 - q_c^2) > 0, \tag{139}$$

$$(n-w)^2 - Q^2 > 0. \tag{140}$$

That means for the excitation near a slow wave sideband frequency with $\omega \approx (n-Q)\omega_0$ and positive n with $n > Q$,

$$w < n - Q, \tag{141}$$

i.e. the excitation frequency ω must be slightly below the resonance frequency $(n-Q)\omega_0$. For the excitation near a fast wave sideband frequency with $\omega \approx (n+Q)\omega_0$ and negative n with $n > -Q$,

$$w > n + Q, \tag{142}$$

i.e. the excitation frequency ω must be slightly above the resonance frequency $(n+Q)\omega_0$.
Finally, we note the relation between $\bar{y}$ and $\bar{y}_i$

$$\bar{y} = -\frac{\omega^2 - q_c^2\omega_0^2}{q_c^2\omega_0^2}\bar{y}_i = -\frac{w^2 - q_c^2}{q_c^2}\bar{y}_i. \tag{143}$$

Since $\omega \approx q_c\omega_0$, the amplitude of the beam oscillation is very small compared to the large amplitude of the ion oscillation.

15.2 Experimental observations

Here, we cite some important observations during shaking experiments at the CERN Antiproton Accelerator (CERN AA) which are reported by Alain Poncet [16]:

"The effects of neutralization have been considerably reduced by exciting vertical coherent oscillations with a transverse kicker in the CERN AA. The shaking system has been permanently implemented. It has the following parameters:
shaking: vertical
shaking frequency: 490 kHz
sideband frequency: 480 kHz
length of kicker electrodes: 0.6 m
kicker field: ~ 20 V/cm
The experimental observations can be summarized as follows:

1. Beam shaking works best when applied vertically. A possible reason is that neutralization is high in dipole fields due to the low ion drift velocity. In addition the ions can oscillate freely along the vertical magnetic field lines.
2. The beam shaking relies on the longitudinal motion of the ions. Due to changing beam dimensions, the ion 'bounce frequency' is not constant. But the frequency of the shaking kicker defines the positions in the ring where the bounce frequency is in resonance with the kicker frequency. Thus, ions must move longitudinally to the resonance positions. Therefore, beam shaking works best in conjunction with clearing electrodes which provide a low level of neutralization. Then, the ions can be accelerated by the longitudinal gradients of the beam potential towards the resonance positions.
3. Beam shaking depends on the non-linearity of the space-charge field. This allows the 'lock-on' of the sweeping ions onto the resonance. There, they keep large oscillation amplitudes and their density is reduced in the beam center.
4. Beam shaking is efficient even with low RF fields of only 10 V/cm, provided it is applied close to a beam betatron sideband whose frequency lies close to the ion bounce frequency. In this case, the beam resonant response yields sufficiently large non-linear forces on the ion. Experimentally, it is found that for a weakly exciting RF field, shaking works best above a band $(n + Q)$ or below a band $(n - Q)$. This observation of asymmetry of weak resonant shaking is important in that it validates the non-linear character of the ion motion and the 'lock-on' conditions."

15.3 Resonant transverse shaking of the HESR beam

The HESR ring is an energy variable machine yielding beam momenta between 1.5 and 15.0 GeV/c. Thus, the revolution frequencies $f_0 = \omega_0/(2\pi)$ are not constant but depend on the beam momentum. The betatron tunes amount to $Q_x = 7.5995$ and $Q_y = 7.6216$. In Table 28 we list the corresponding slow-wave sideband frequencies $(n - Q)f_0$ for $n = 8$ and the fast-wave sideband frequencies $(n + Q)f_0$ for $n = -7$.

Table 28: Slow- and fast-wave sideband frequencies.

p (GeV/c)	f_0 (kHz)	$(8 - Q_x)f_0$ (kHz)	$(8 - Q_y)f_0$ (kHz)	$(Q_x - 7)f_0$ (kHz)	$(Q_y - 7)f_0$ (kHz)
1.500	441.9	177.0	167.2	264.9	274.7
3.825	506.2	202.7	191.5	303.5	314.7
8.889	518.3	207.6	196.1	310.7	322.2
15.00	520.2	208.3	196.8	311.9	323.4

If we assume $1.0 \cdot 10^{11}$ antiprotons in the HESR ring the 'tune numbers' q_x and q_y of H^+ and H_2^+ ions coincide at many places with one of the sideband tunes $(8 - Q_x) = 0.4005$, $(8 - Q_y) = 0.3784$, $(Q_x - 7) = 0.5995$ or $(Q_y - 7) = 0.6216$. The 'tune numbers' are proportional to $\sqrt{N_{\bar{p}}/[\sigma_{x,y}(\sigma_x + \sigma_y)]}$. For $N_{\bar{p}} = 1.0 \cdot 10^{10}$ all 'tune numbers' decrease by a factor $\sqrt{10^{1/5}} = 1.26$. Resonant transverse shaking is not all possible for heavier ions like CO^+ ions. Even for $N_{\bar{p}} = 1.0 \cdot 10^{11}$ the 'tune numbers' of CO^+ oscillations are below the sideband tunes.

The possible shaking frequencies are in the range of about 165-330 kHz. A broad-band kicker covering this frequency range with field strengths of about 20 V/cm would be sufficient for resonant transverse shaking of the most critical H^+- and H_2^+-ions.

Summarizing, we note that beam shaking alone is not sufficient to remove trapped ions. Clearing of trapped ions by shaking is only possible under certain conditions at discrete specific positions in the ring and for light ions like H^+ and H_2^+. Heavier ions cannot be removed by beam shaking. Therefore, clearing of trapped ions in the HESR ring should be mainly done with the aid of clearing electrodes.

Finally, we mention that beam shaking deteriorates the transverse beam quality. This fact must be taken into account when applying beam shaking in the HESR ring.

16. Trapped Ion Effects in the Electron Cooler

Here, we discuss the special problems due to the electron beam if the electron cooler (EC) is installed. We refer to the final HESR Electron Cooler Design Study [43]. The electron beam current I_e amounts to 1.0 A. It is guided by the EC solenoid with a constant beam radius $a = 5$ mm. The inner diameter of the EC vacuum chamber amounts to 200 mm. The resulting radius profile $r_c(s)$ is shown in Fig. 32. The total length of the EC solenoid is $L_{EC} = 24.0$ m. In addition, nine beam position monitors are foreseen. The beam position monitors consist of four electrodes that together form a cylinder with an inner diameter of 200 mm and a length of 200 mm.

16.1 Negative potential well of the electron beam

We first estimate the negative potential well due to the strong electron beam. The linear charge density λ is given by

$$\lambda = \frac{\mathrm{d}Q}{\mathrm{d}s} = \frac{I}{v}. \tag{144}$$

Here, I is the current and $v = \beta c$ the longitudinal velocity of the electrons. The resulting potential well and the electric field can be calculated using Eqs. (4)-(6). A round electron beam of 1.0 A with a constant density within a radius $a = 5$ mm yields the following values (kinetic energy of the electron beam: 4.5 MeV, $\beta = 0.994787$):

$$\frac{\lambda}{2\pi\epsilon_0} = -60.3 \text{ V}, \tag{145}$$

$$U(0) = -210.7 \text{ V}, \tag{146}$$

$$E_r(a) = -12.1 \text{ kV/m}. \tag{147}$$

The absolute value of the electric field component in radial direction, $|E_r|$, is maximum at the edge of the electron beam, i.e. at $r = a$. For comparison we calculate the corresponding potential well parameters of an antiproton beam with $N_{\bar{p}} = 1.0 \cdot 10^{10}$ at 8.889 GeV/c using Eqs. (8) and (13). In order to have more than 90% of the antiproton beam inside the electron beam the beta-values in the EC section are chosen to be $\beta_x = \beta_y = 80$ m [43]. For $N_{\bar{p}} = 1.0 \cdot 10^{10}$ the rms emittance amounts to $\epsilon_x = \epsilon_y \approx 0.043$ mm mrad. These values yield the rms-widths of the beam in the EC section, $\sigma_x \approx \sigma_y \approx 1.86$ mm. We note that these values are used in the BETACOOL simulations of the EC [43]. They are considerably smaller than the σ_x and σ_y values shown in Figs. 3 and 4 which are calculated for $N_{\bar{p}} = 1.0 \cdot 10^{11}$ assuming $\beta_x = \beta_y \approx 175$ m and $\epsilon_x = \epsilon_y = 0.148$ mm mrad at 15 GeV/c. Thus, we assume inside of the EC a round Gaussian beam distribution with $\sigma_r \approx 1.86$ mm. The maximum of the absolute value of the electric field is located at $r_m = 1.585\,\sigma_r = 2.94$ mm. The inner radius of the beam pipe amounts to 100 mm. These parameters yield for $1.0 \cdot 10^{10}$ antiprotons at 8.889 GeV/c

$$\frac{\lambda}{2\pi\epsilon_0} = -0.0556 \text{ V}, \tag{148}$$

$$U(0) = -0.219 \text{ V}, \tag{149}$$

$$E_r(r_m) = -17.4 \text{ V/m}. \tag{150}$$

The depth of the electron potential well is a factor of 962 larger than the depth of the antiproton potential well and the maximum of the electric field is a factor of 694 larger.

Summarizing, the negative potential well of the electron beam acts as a very deep pocket for trapped ions (see Fig. 33). The positive ions perform modified cyclotron motions around the magnetic field lines of the solenoid and magnetron motions around the central axis of the electron beam, see Subsections 9.2.

It is interesting to note that the transverse electric field of the electron beam (about 12 kV/m at beam edge) is so strong that $\omega_b = 1.07 \cdot 10^7$ s^{-1} for H_2^+ ions. The magnetic field of the EC solenoid is rather low (0.2 T) yielding $\omega_c = 9.58 \cdot 10^6$ s^{-1} for H_2^+ ions. Using Eqs. (59) and (60), we get $f_+ = 2.63 \cdot 10^6$ Hz for the frequency of the modified cyclotron motion and $f_- = 1.11 \cdot 10^6$ Hz for the frequency of the magnetron motion of H_2^+ ions. The high value of f_- is a consequence of the high transverse electric field. In the PANDA target solenoid and the compensation solenoids the frequency f_- is rather low.

16.2 Ionization rate and neutralization due to the electron beam

The number of antiprotons per second amounts to about $\dot{N}_{\bar{p}} = 5.0 \cdot 10^{16}$ s^{-1} if $1.0 \cdot 10^{11}$ antiprotons are stored in the HESR ring. This corresponds to a mean $\bar{p}$ current of about 8 mA. The current of the electron beam amounts to 1.0 A. This corresponds to a number of electrons per second of $\dot{N}_e = 6.24 \cdot 10^{18}$ s^{-1} which is a factor of 125 larger. Therefore, the ionization rate due to the electron beam is also a factor of 125 larger. In the following estimates of ionization and neutralization we neglect the very small contribution of the antiproton beam in the region of the electron cooler.

We recall that the ionization cross section depends on the molecules in the residual gas and the velocity $\beta = v/c$ of the beam particles. It does not depend on the charge and the mass of the beam particles. Now, the velocity of the electron beam is exactly equal to the velocity of the antiproton beam. Therefore, applying Bethe's formula (23) yields identical ionization cross sections σ for electrons and antiprotons and we can use the values listed in Table 2. The corresponding production rate R_p for a certain ion species is given by

$$R_p = \sigma \rho_m \beta c. \tag{151}$$

Here, σ is the ionization cross section, ρ_m the number density of the residual molecules and βc the velocity of the beam particles. The production time T_p is the inverse of the production rate, $T_p = 1/R_p$. It is simply the time which a single antiproton and/or electron needs in order to produce one singly charged ion. We note that the production rate R_p and the production time T_p are also identical for electrons and antiprotons.

The following estimates are taken from the final electron cooler design study [43]. In the region of the electron cooler big pumps on both sides of the straight cooling section and the return straight section are installed. The distance between the pumps is 30 m. The outgassing rate is assumed to be $q = 1.0 \cdot 10^{-12}$ mbar·liter/cm^2/s after bake-out to 150°C. The residual gas is assumed to consist of H_2 (75 %), CH_4 (14 %) and CO (11 %). The average pressure for each gas is calculated taking the specific molecular conductance $w = 305\, r^3 \sqrt{T/M}$ into account. The calculated average partial pressures become

1. $5.5 \cdot 10^{-10}$ mbar for H_2 ($\rho_m = 1.5 \cdot 10^{13}$ m^{-3}),
2. $1.3 \cdot 10^{-10}$ mbar for CO ($\rho_m = 3.5 \cdot 10^{12}$ m^{-3}),
3. $2.0 \cdot 10^{-10}$ mbar for CH_4 ($\rho_m = 5.3 \cdot 10^{12}$ m^{-3}).

The ionization cross sections σ and the resulting production times T_p are

1. $\sigma = 2 \cdot 10^{-23}$ m^2, $T_p = 11$ s for H_2,

2. $\sigma = 9 \cdot 10^{-23}$ m^2, $T_p = 11$ s for CO,
3. $\sigma = 11 \cdot 10^{-23}$ m^2 $T_p = 6$ s for CH_4.

It is planned to remove the trapped ions with clearing electrodes near the entrance and exit of the straight cooling section [43]. The clearing electrodes are installed in the merging modules. The resulting clearing times due to the mean thermal velocity in one direction are estimated as [43]

1. $T_c = 13$ ms for H_2,
2. $T_c = 50$ ms for CO,
3. $T_c = 38$ ms for CH_4.

The resulting mean neutralization η from H_2, CO and CH_4 amounts to

$$\eta = \left(\frac{T_c}{T_p}\right)_{H_2} + \left(\frac{T_c}{T_p}\right)_{CO} + \left(\frac{T_c}{T_p}\right)_{CH_4} = \frac{0.013}{11} + \frac{0.050}{11} + \frac{0.038}{6} = 0.012. \tag{152}$$

We note that a neutralization of 1.2 % is rather high when comparing it with the neighbouring sections of the HESR ring. This is due to the fact that the clearing electrodes are located outside of the 24 m long cooler section. Taking the rotation of the electron beam by the space charge of the trapped ions into account the allowed upper limit of η amounts to 6 % at 4.5 MeV kinetic energy of the EC [43], see also Subsection 16.3. Thus, the achievable neutralization of 1.2 % is sufficiently small for the operation of the electron cooler at high beam energies, especially at the maximum energy 4.5 MeV [43].

However, it is not always desirable to have η as small as possible. That means, there is not only an upper limit for η but also a lower limit if the beam rotation is considered in the low-energy range 0.45 MeV - 2.0 MeV, see Subsections 16.4 and 16.5. For instance at the lowest energy 0.45 MeV, the neutralization should be limited to

$$0.247 \leq \eta \leq 0.319. \tag{153}$$

The method to achieve a certain well defined neutralization of the electron-cooling beam is presented in Subsections 18.1 and 18.3.

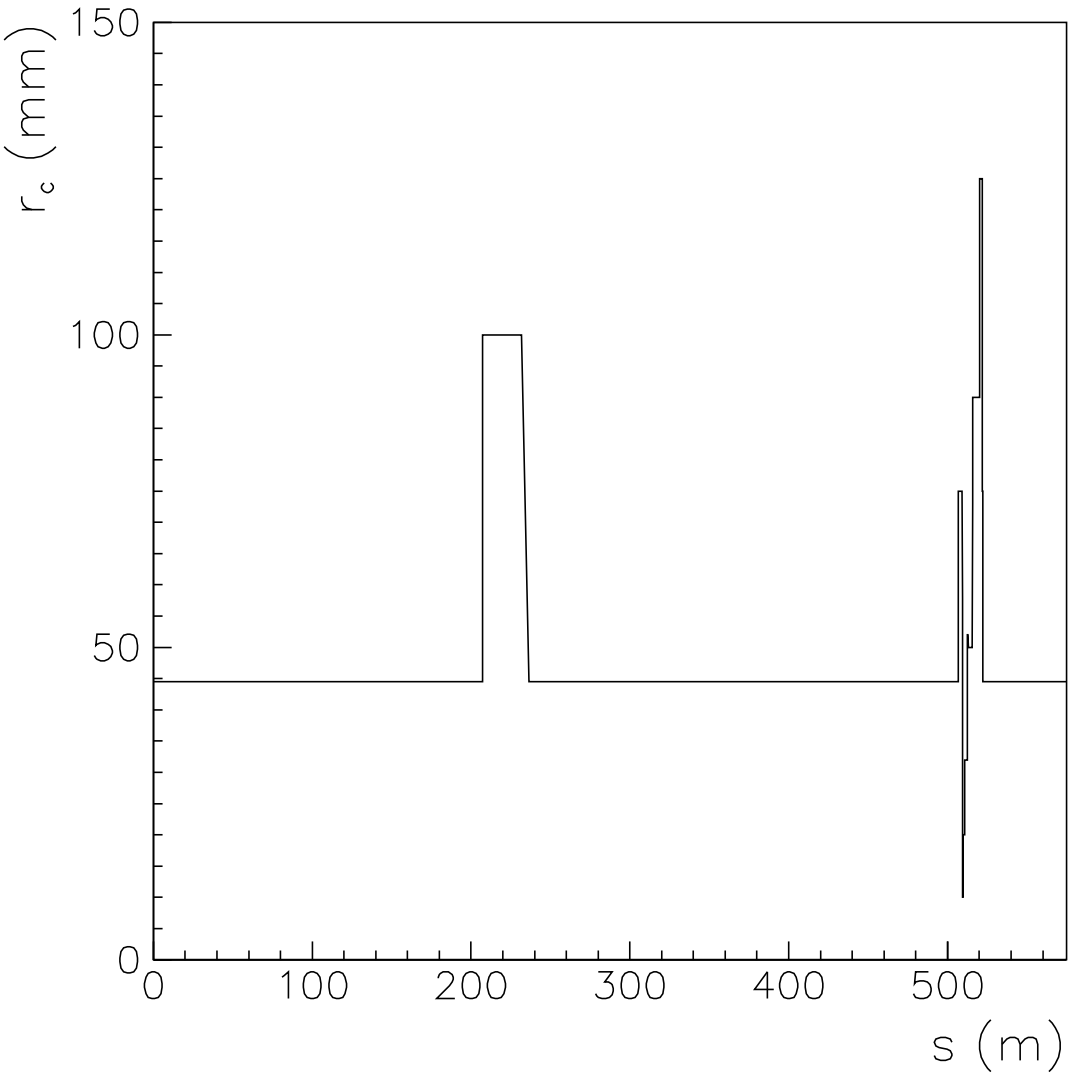

Fig. 32: Inner beam pipe radius $r_c(s)$ after installation of the electron cooler.

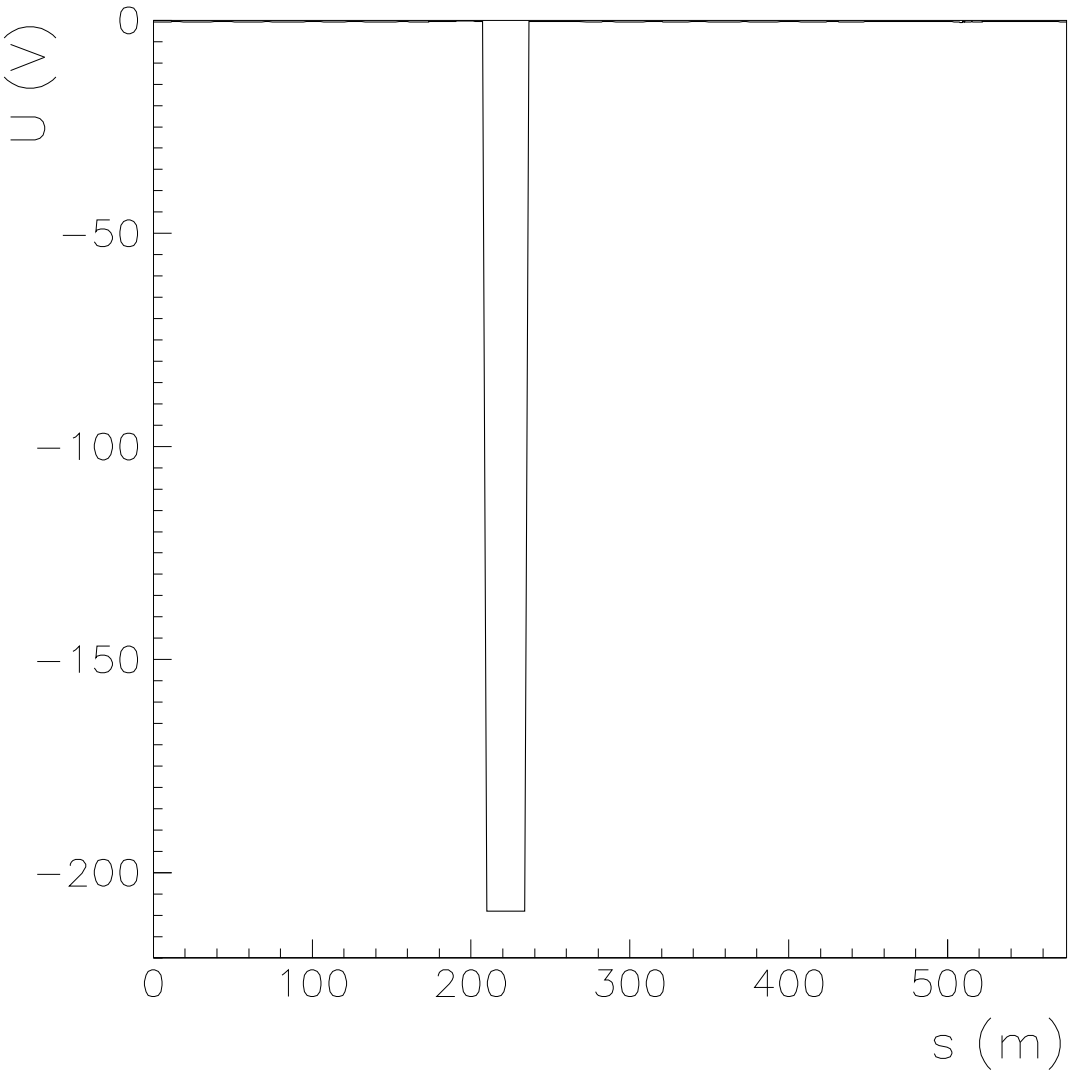

Fig. 33: Central potential $U(s)$ showing the large potential depth due to the electron beam.

16.3 Upper limit of EC neutralization by trapped ions at high beam energies

In order to estimate an upper limit of electron-beam neutralization the rotation of the electron beam by the space-charge of trapped ions was calculated in Subsection 7.10.1 of the HESR Electron Cooler Design Study [43]. The absolute value of the azimuthal velocity of an electron at the beam edge $r = a$ is given by (for a derivation see Subsection 17.2):

$$|v_{az}(a)| = \left|\frac{1-\eta\gamma_e^2}{\gamma_e^2}\right| \frac{I_e}{\beta_e c}\frac{1}{2\pi\epsilon_0}\frac{1}{B}\frac{1}{a}. \tag{154}$$

Here, I_e is the electron beam current, η the neutralization, B the magnetic field of the solenoid, a the radius of the electron beam. The quantities γ_e and β_e are defined by the electron beam energy. The upper limit is specified by the requirement

$$\frac{|v_{az}(a)|}{\beta_e c} \leq 1.0 \cdot 10^{-5} \tag{155}$$

This condition corresponds to the maximum r.m.s. non-straightness of the magnetic field lines [43]. Using this condition yields for $I_e = 1.0$ A, $a = 5$ mm, $B = 0.2$ T and the maximum kinetic energy 4.5 MeV of the electron cooler[10]

$$\eta \leq \left(\frac{1}{\gamma_e^2} + \frac{10^{-5}\beta_e^2 c^2 2\pi\epsilon_0 aB}{I_e}\right) = 0.06. \tag{156}$$

16.4 Lower limit of EC neutralization by trapped ions at low beam energies

Taking the requirement $|v_{az}(a)|/(\beta_e c) \leq 1.0\cdot 10^{-5}$ at the lowest kinetic energy 0.45 MeV yields not only an upper limit but also a lower limit for the neutralization η. This is due to the fact that the azimuthal velocity $v_{az}(a)$ can be either positive or negative depending on the sign of $1-\eta\gamma_e^2$. At the lowest energy 0.45 MeV γ_e is rather small ($\gamma_e = 1.88$ at 0.45 MeV) and $|v_{az}(a)|/(\beta_e c)$ becomes rather large if $\eta \approx 0$, see Table 31. Thus, if $\eta < 1/\gamma_e^2$ the corresponding inequality may be written

$$\eta \geq \left(\frac{1}{\gamma_e^2} - \frac{10^{-5}\beta_e^2 c^2 2\pi\epsilon_0 aB}{I_e}\right). \tag{157}$$

This yields for $T_e = 0.45$ MeV

$$\eta \geq 0.247. \tag{158}$$

16.5 Consideration of lower and upper limits of EC neutralization

In the HESR Electron Cooler Design Study [43] only an upper limit of η at the highest energy 4.5 MeV has been considered. Here, we compile the lower and upper limits at different beam energies between 0.45 MeV and 4.5 MeV. The requirement $|v_{az}(a)|/(\beta_e c) \leq 1.0 \cdot 10^{-5}$ yields the following inequality

$$\left(\frac{1}{\gamma_e^2} - \frac{10^{-5}\beta_e^2 c^2 2\pi\epsilon_0 aB}{I_e}\right) \leq \eta \leq \left(\frac{1}{\gamma_e^2} + \frac{10^{-5}\beta_e^2 c^2 2\pi\epsilon_0 aB}{I_e}\right). \tag{159}$$

In Table 29 we list the resulting lower and upper limits of η for the energy range 0.45 MeV-4.5 MeV.

[10] There is a typo in the corresponding equation of Ref. [43]. The right side must be multiplied with $1/\gamma_e^2$, i.e.

$$\eta \leq \left(1 + \frac{10^{-5}\beta_e^2\gamma_e^2 c^2 2\pi\epsilon_0 aB}{I_e}\right)\frac{1}{\gamma_e^2}.$$

Table 29: Lower and upper limits η_{min} and η_{max} yielding sufficiently low $|v_{az}(a)|/(\beta_e c) \leq 1.0 \cdot 10^{-5}$.

T_e (MeV)	β_e	γ_e	$1/\gamma_e^2$	η_{min}	η_{max}
0.45	0.847	1.88	0.283	0.247	0.319
1.5	0.967	3.94	0.0646	0.0178	0.111
2.0	0.979	4.91	0.0414	0.0	0.0893
2.5	0.985	5.89	0.0288	0.0	0.0774
3.5	0.992	7.85	0.0162	0.0	0.0654
4.5	0.995	9.81	0.0104	0.0	0.0599

We note that a neutralization with a negative sign cannot occur since negatively charged ions cannot be created and trapped in the antiproton beam. Therefore, the entries of η_{min} with negative sign have been replaced by a zero. The list in Table 29 shows that a lower limit of η should be considered at low energies.

17. Drawbacks of the Space-Charge Potential of the Electron Beam

The electron beam of the HESR electron cooler is very intensive and dense (current $I_e = 1.0$ A, radius $a = 5$ mm). Here, we discuss the drawbacks of the high space-charge for the cooling process. (i) The space-charge potential of the electron beam causes a significant radial dependence of the electron energies, see Subsection 17.1. (ii) In addition. there is the cross-field drift velocity due to the longitudinal magnetic field of the cooler solenoid and the radial force F_r caused by the electric and magnetic field of the fast-moving electron beam. Also this effect must be taken into account. It yields a non-negligible transverse azimuthal velocity v_{az}, see Subsection 17.2.

17.1 Dependence of the electron energy on the space-charge potential of the electron beam

The space-charge potential $U(r)$ of the EC beam can be calculated using (160) – (162)

$$\lambda = -\frac{I_e}{\beta_e c}. \tag{160}$$

Here, $I_e = 1.0$ A is the electron current and $\beta_e c$ the electron velocity. Taking the neutralization η due to trapped ions into account and assuming $U(r_c) = 0$ at the inner surface of the beam pipe (radius $r_c = 100$ mm) the space-charge potential $U(r)$ may be written

$$U(r) = \frac{\lambda(1-\eta)}{2\pi\epsilon_0} \ln\frac{r_c}{r} = (-60.0\,\mathrm{V})\frac{(1-\eta)}{\beta_e}\ln\frac{r_c}{r} \quad r \geq a, \tag{161}$$

$$\begin{aligned} U(r) &= \frac{\lambda(1-\eta)}{2\pi\epsilon_0}\left[\frac{1}{2} - \frac{r^2}{2a^2} + \ln\left(\frac{r_c}{a}\right)\right] \\ &= (-60.0\,\mathrm{V})\frac{(1-\eta)}{\beta_e}\left[\frac{1}{2} - \frac{r^2}{2a^2} + \ln\left(\frac{r_c}{a}\right)\right] \quad r \leq a. \end{aligned} \tag{162}$$

In Fig. 34 we show the space-charge potential U(r) for two electron beam energies (0.45 MeV and 4.5 MeV). The potential is zero at the vacuum chamber ($r_c = 100$ mm) and has its deep minimum at the beam center. It depends strongly on the neutralization η of the electron beam, see factor $(1-\eta)$ in Eqs. (161) and (162). If the neutralization is negligibly small ($\eta \approx 0$) the space charge potential is maximal. If the electron beam is fully neutralized ($\eta = 1$) the space charge potential is zero.

The kinetic energy of the electrons T_e is given by the absolute value of the cathode potential $|U_{cath}|$ and the *negative* space-charge potential $U(r)$,

$$T_e = (\gamma - 1)m_e c^2 = e[|U_{cath}| + U(r)]. \tag{163}$$

In Fig. 35 we show the variation of the electron energy due to the space-charge potential in the region of the beam ($r \leq 5$ mm). The full curve refers to $\eta = 0$, the dashed curve to $\eta = 0.9$. The variation is zero if the electron beam is fully neutralized by trapped ions, i.e. $\eta = 1$.

The variation of the electron energy due to the space-charge potential is rather large. Taking the difference of kinetic energies, $\Delta T_e = e[U(a) - U(0)]$, between the beam edge and the beam center yields the characteristic relative energy deviation $\Delta T_e/T_e$ due to the space-charge potential, see Table 30.

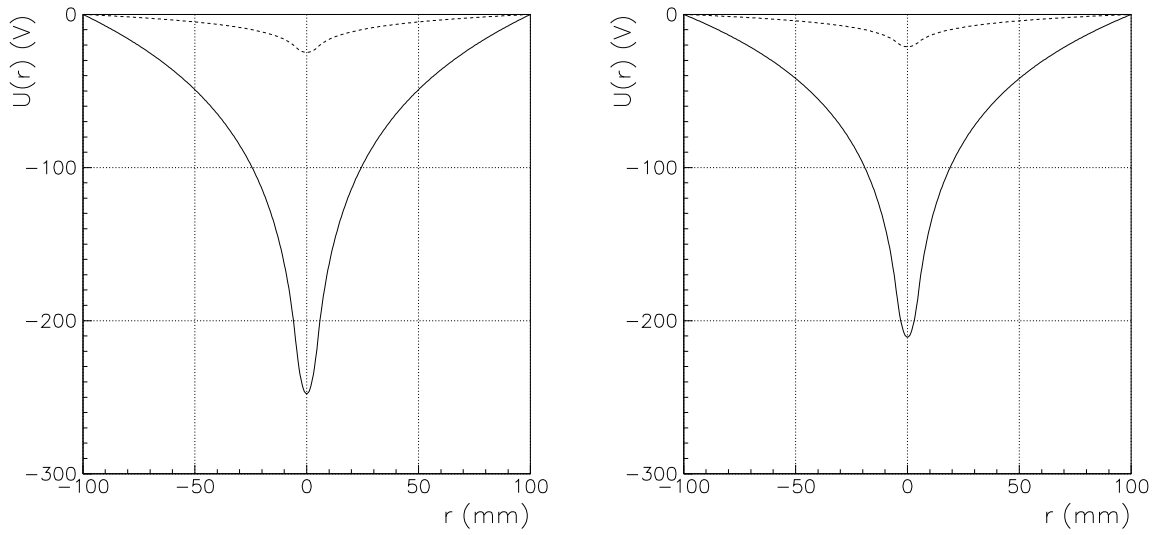

Fig. 34: Space charge potential $U(r)$ of the electron beam ($I_e = 1.0$ A, beam radius $a = 5$ mm, radius of vacuum chamber: $r_c = 100$ mm). Note: The space charge potential is zero at the vacuum chamber radius $r_c = 100$ mm. Full line: Beam neutralization $\eta = 0.0$. Dashed line: Beam neutralization $\eta = 0.9$. Left: Nominal kinetic energy 0.45 MeV. Right: Nominal kinetic energy 4.5 MeV.

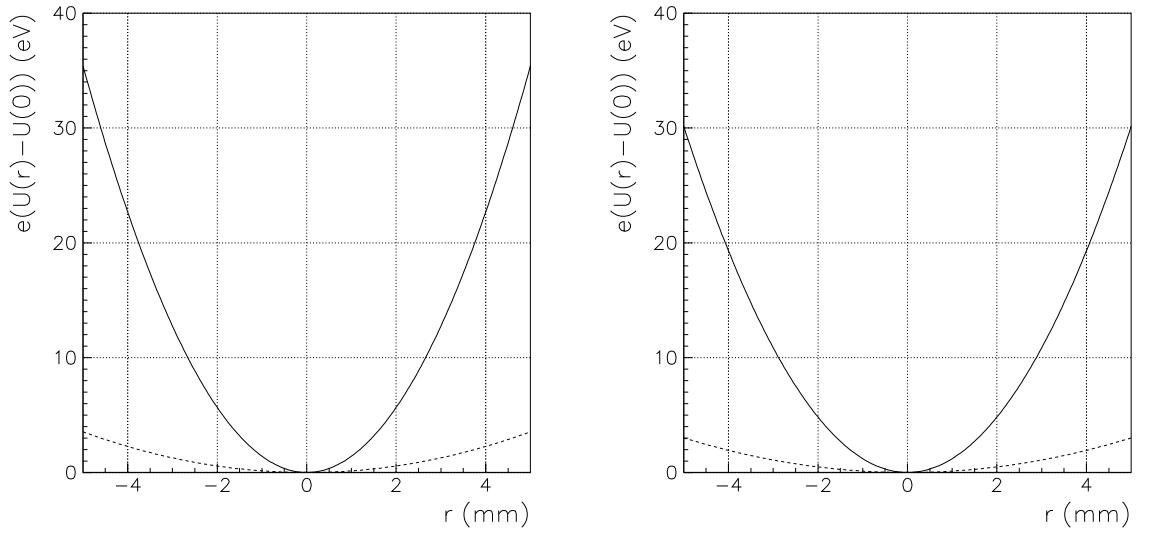

Fig. 35: Variation of the electron energy due to the space-charge potential $U(r)$ of the EC beam. Full line: Beam neutralization $\eta = 0.0$. Dashed line: Beam neutralization $\eta = 0.9$. Left: Nominal kinetic energy 0.45 MeV. Right: Nominal kinetic energy 4.5 MeV.

The corresponding relative momentum deviation can be calculated using

$$\frac{\Delta p_{\bar{p}}}{p_{\bar{p}}} = \frac{\Delta p_e}{p_e} = \frac{\gamma_e - 1}{\gamma_e} \frac{1}{\beta_e^2} \frac{\Delta T_e}{T_e}. \tag{164}$$

The velocity $\beta_{\bar{p}} c$ of the antiproton beam approaches the velocity $\beta_e c$ of the electron beam during the cooling process. Therefore we get with $\beta_{\bar{p}} = \beta_e$ and $\gamma_{\bar{p}} = \gamma_e$

$$\frac{\Delta p_{\bar{p}}}{p_{\bar{p}}} = \frac{\Delta p_e}{p_e}. \tag{165}$$

In order to see the effects of the space-charge potential at a glance we list the relative energy and momentum deviations for $\eta \approx 0$ in Table 30.

Table 30: Relative energy and momentum deviations due to space-charge effects assuming negligibly small neutralization ($\eta \approx 0$).

T_e (MeV)	$\Delta T_e/T_e$	$\Delta p_e/p_e$
0.45	$7.87 \cdot 10^{-5}$	$5.14 \cdot 10^{-5}$
1.5	$2.07 \cdot 10^{-5}$	$1.65 \cdot 10^{-5}$
2.5	$1.22 \cdot 10^{-5}$	$1.04 \cdot 10^{-5}$
3.5	$8.64 \cdot 10^{-6}$	$7.66 \cdot 10^{-6}$
4.5	$6.70 \cdot 10^{-6}$	$6.08 \cdot 10^{-6}$

The rationale of the HESR EC is to reach a momentum resolution of the antiproton beam in the order of $1.0 \cdot 10^{-5}$. This cannot be achieved at low beam energies. Therefore, one should try to reduce the variation of the electron energy which is due to the large space-charge potential of the electron beam. This can be achieved by neutralizing the electron beam, see Subsect. 18.1. However, the effect of transverse motions due to the space-charge of trapped ions must also be taken into account, see Subsection 18.4.

17.2 Azimuthal velocities due to the space-charge potential of the electron beam

Now, we consider the transverse motion of an electron due to the interaction with the space-charge of the EC beam and the space charge of trapped ions. The radial force F_r due to the space charge of a fast-moving beam may be written

$$F_r = e(1 - \beta_e^2) \frac{I_e}{\beta_e c} \frac{1}{2\pi\epsilon_0} \frac{r}{a^2}. \tag{166}$$

The term with β_e^2 takes the azimuthal magnetic field B_Θ of a fast-moving beam into account. The resulting radial force $F_r = e(E_r - \vec{v_e} \times \vec{B}) = e(E_r - \beta_e c B_\Theta) = e(1 - \beta_e^2) E_r$ is directed outwards. In addition the radially attractive force due to the space charge of the trapped ions must be taken into account. Thus, we get

$$F_r = e(1 - \beta_e^2 - \eta) \frac{I_e}{\beta_e c} \frac{1}{2\pi\epsilon_0} \frac{r}{a^2}. \tag{167}$$

Using $(1-\beta_e^2) = 1/\gamma_e^2$, this equation may be written

$$F_r = e\frac{1-\eta\gamma_e^2}{\gamma_e^2}\frac{I_e}{\beta_e c}\frac{1}{2\pi\epsilon_0}\frac{r}{a^2}. \tag{168}$$

This equation shows that the effect of the beam neutralization η is magnified by the factor γ_e^2. We note that the factor γ_e^2 is rather large ($\gamma_e^2 = 3.54$ at $T_e = 0.45$ MeV and $\gamma_e^2 = 96.2$ at $T_e = 4.5$ MeV).

Writing the equations of motions one sees that the combination of a radial force F_r with the cyclotron motion in a longitudinal magnetic field B yields a modified cyclotron motion ω_+ and a magnetron motion ω_- around the beam center, see Sect. 9. and Appendix of Ref. [1]. These two angular frequencies are related to the basic angular frequency ω_c of the cyclotron motion

$$\omega_c = \frac{eB}{\gamma_e m_e}, \tag{169}$$

and the angular frequency ω_b which takes the effect of the radial force F_r into account,

$$\omega_b^2 = \frac{e}{\gamma_e m_e}\frac{1-\eta\gamma_e^2}{\gamma_e^2}\frac{I_e}{\beta_e c}\frac{1}{2\pi\epsilon_0}\frac{1}{a^2}. \tag{170}$$

The resulting angular frequencies ω_+ and ω_- may be written

$$\begin{aligned}
\omega_+ &= \frac{\omega_c}{2} + \sqrt{\left(\frac{\omega_c}{2}\right)^2 - \omega_b^2}, \\
\omega_- &= \frac{\omega_c}{2} - \sqrt{\left(\frac{\omega_c}{2}\right)^2 - \omega_b^2}.
\end{aligned} \tag{171}$$

Numerically, we get for $\eta = 0$, $I_e = 1.0$ A, $a = 0.005$ m, $B = 0.2$ T and the kinetic energy range $0.45\ \mathrm{MeV} - 4.5\ \mathrm{MeV}$

$$\begin{aligned}
\omega_c &= 1.87046 \cdot 10^{10}\ \mathrm{s}^{-1}, \quad \omega_b^2 = 2.64845 \cdot 10^{17}\ \mathrm{s}^{-2}, \quad T_e = 0.45\ \mathrm{MeV}, \\
\omega_c &= 3.51763 \cdot 10^{9}\ \mathrm{s}^{-1}, \quad \omega_b^2 = 4.24034 \cdot 10^{16}\ \mathrm{s}^{-2}, \quad T_e = 4.5\ \mathrm{MeV},
\end{aligned} \tag{172}$$

$$\begin{aligned}
\omega_+ &= 1.8690 \cdot 10^{10}\ \mathrm{s}^{-1}, \quad \omega_- = 1.4170 \cdot 10^{7}\ \mathrm{s}^{-1}, \quad T_e = 0.45\ \mathrm{MeV}, \\
\omega_+ &= 3.5056 \cdot 10^{9}\ \mathrm{s}^{-1}, \quad \omega_- = 1.2096 \cdot 10^{7}\ \mathrm{s}^{-1}, \quad T_e = 4.5\ \mathrm{MeV}.
\end{aligned} \tag{173}$$

We are interested to estimate the transverse velocities $v_{az} = r\omega_-$ which are due to the azimuthal magnetron motion around the beam center. Since $(\omega_c/2)^2 \gg \omega_b^2$, we can use the approximation

$$\omega_- \approx \frac{\omega_b^2}{\omega_c}. \tag{174}$$

Thus, we get for ω_-

$$\omega_- = \frac{1-\eta\gamma_e^2}{\gamma_e^2}\frac{I_e}{\beta_e c}\frac{1}{2\pi\epsilon_0}\frac{1}{B}\frac{1}{a^2}. \tag{175}$$

The resulting transverse (azimuthal) velocity $v_{az}(r)$ of the electrons may thus be written

$$v_{az}(r) = \omega_- r = \frac{1-\eta\gamma_e^2}{\gamma_e^2}\frac{I_e}{\beta_e c}\frac{1}{2\pi\epsilon_0}\frac{1}{B}\frac{r}{a^2}. \tag{176}$$

The transverse velocity is maximum at the beam edge $r = a$,

$$v_{az}(a) = \omega_- a = \frac{1-\eta\gamma_e^2}{\gamma_e^2}\frac{I_e}{\beta_e c}\frac{1}{2\pi\epsilon_0}\frac{1}{B}\frac{1}{a}. \tag{177}$$

Assuming a negligibly small neutralization ($\eta \approx 0$), we get for the azimuthal velocity $v_{az}(a)$ at the beam edge ($r = a = 5$ mm) the results listed in Table 31. The transverse velocities

Table 31: Electron beam rotation v_{az} due to space-charge effects assuming negligibly small neutralization ($\eta \approx 0$).

T_e (MeV)	ω_+ (s^{-1})	ω_- (s^{-1})	$v_{az}(a)$ (m/s)	$v_{az}(a)/\beta_e c$
0.45	$1.87 \cdot 10^{10}$	$4.00 \cdot 10^{6}$	$2.00 \cdot 10^{4}$	$7.89 \cdot 10^{-5}$
1.5	$8.94 \cdot 10^{9}$	$8.01 \cdot 10^{5}$	$4.00 \cdot 10^{3}$	$1.38 \cdot 10^{-5}$
2.0	$7.16 \cdot 10^{9}$	$5.07 \cdot 10^{5}$	$2.54 \cdot 10^{3}$	$8.64 \cdot 10^{-6}$
2.5	$5.97 \cdot 10^{9}$	$3.50 \cdot 10^{5}$	$1.75 \cdot 10^{3}$	$5.93 \cdot 10^{-6}$
3.5	$4.48 \cdot 10^{9}$	$1.96 \cdot 10^{5}$	$9.81 \cdot 10^{2}$	$3.30 \cdot 10^{-6}$
4.5	$3.59 \cdot 10^{9}$	$1.25 \cdot 10^{5}$	$6.25 \cdot 10^{2}$	$2.10 \cdot 10^{-6}$

v_{az} vary linearly between zero at the beam center and a maximum at the beam edge. In order to achieve a relative momentum resolution $\Delta p/p \leq 1.0 \cdot 10^{-5}$ one can accept $v_{az}(a)/(\beta_e c) \leq 1.0 \cdot 10^{-5}$. This corresponds to the r.m.s. non-straightness of the magnetic field lines [43]. At low electron energies $T_e < 2$ MeV, this requirement is not fulfilled if $\eta \approx 0$, see Table 31. This drawback can be avoided by neutralizing the electron-cooling beam, i.e. by adjusting $\eta = 1/\gamma_e^2$. Then, the numerator $1 - \eta\gamma_e^2 = 0$ in Eq. (177) becomes zero and the azimuthal velocities v_{az} vanish, see next Subsection.

18. Counteracting Space-Charge Effects of the EC beam

The space-charge potential of the electron-cooling beam destroys the homogeneity of the longitudinal velocity profile $v_{\|}$ and causes a transverse (azimuthal) velocity spread v_{az}. Both effects affect the cooling process, i.e. the velocity matching between the electrons and the antiprotons. Both effects can be mitigated by admitting a certain neutralization of the electron beam.

18.1 Neutralization of the electron-cooling beam with trapped ions

The drawback of the space-charge potential can be removed to some extent by a space-charge neutralization of the electron-cooling beam. Such a space-charge neutralization system has been successfully implemented on the LEAR EC [49, 50, 51]. Instead of extracting the ions which are produced by ionization of the residual gas in the EC, the ions are accumulated. To this end, two sets of neutralization electrodes have been installed outside the interaction region towards the electron gun and towards the electron collector, respectively. The electrodes consist of two metallic half cylinders which are separated by a high-resistive-glass insulator, see Fig. 36. The positive voltages on the electrodes are not equal in order to generate also a transverse electric field $\vec{E}$. The low-energy ions and electrons from the ionization processes move in the longitudinal direction towards the neutralization electrodes. The positively charged ions will be reflected, and therefore stored. The low-energy electrons will be attracted by the positive voltages of the neutralization electrodes. Thereby, the effect of the cross-field-drift velocity $\vec{v}_D = \vec{E} \times \vec{B}/B^2$ is used in order to extract the low-energy electrons from the ionization processes. They drift in the crossed electric and magnetic fields towards the high-resistive-glass insulator.

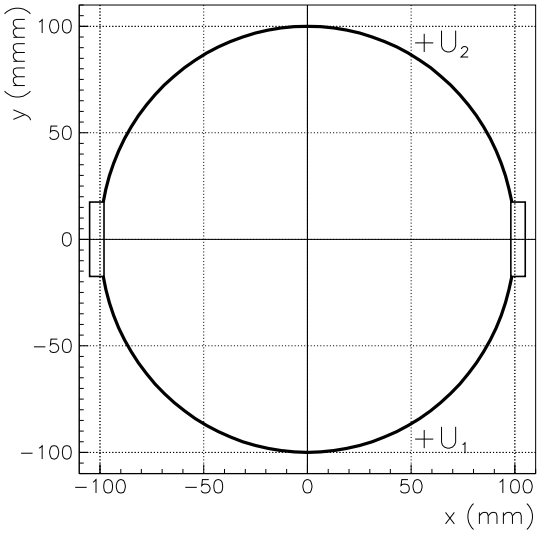

Fig. 36: Scheme of a neutralization electrode for the HESR EC. The electrode consist of two metallic half cylinders which are separated by a high-resistive-glass insulator. The positively charged ions will be reflected, and therefore stored in the EC interaction region. The low-energy electrons drift in the crossed electric and magnetic fields towards the high-resistive-glass insulator.

The ions are trapped in the cooling section of the EC and the neutralization η increases according to the production time. The production time T_p amounts to about 11 s for H_2^+ and

CO^+ ions and about 6 s for CH_4^+ ions. Thus, a specific neutralization (for instance $\eta = 1/\gamma^2$) is quickly reached. In order to stabilize the neutralization level the continuously produced surplus ions can be removed by shaking the ions with a sine-wave signal applied to a transverse kicker, see Subsect. 18.3.

18.2 Measurement of the EC neutralization

There are two methods which can be used in order to determine the neutralization η of the EC beam [50]. Both methods rely on measurements of the velocity, i.e. the velocity of the cooled antiproton beam or the velocity of the electron beam. A precise knowledge of the velocity allows the determination of the kinetic energy of the electron beam and therewith the neutralization η, see Eqs. (162) and (163).

(i) One can measure the cooled antiproton velocity by measuring the revolution frequency of the antiproton beam. The mean velocity $\bar{v}_{\bar{p}}$ of the cooled antiproton beam depends on the neutralization η of the electron beam, see Subsect. 17.1. An increase of η implies a decrease of the cathode potential $|U_{cath}|$ if the the ion revolution frequency is kept constant. The corrections of the cathode potential $\Delta|U_{cath}|$ can be used in order to deduce $\Delta\eta$.

(ii) A more direct method has also been developed at LEAR [50]. The Time-Of-Flight (TOF) method is based on the fact that a density modulation signal imposed on the electron beam depends on the mean velocity $\bar{v}_e$ of the electron beam and therewith also on the neutralization η. The longitudinal density of the electron beam is weakly modulated by a sinusoidal signal applied on the neutralization electrode at the entrance of the EC. This signal is taken from a network analyzer at a frequency of about 300 MHz. The modulated signal is detected at the neutralization electrode at the exit of the EC. The phase difference $\Delta\phi$ between the signals at the entrance and exit can be used in order to determine the mean velocity $\bar{v}_e$ of the EC beam and therewith the neutralization level η. The TOF method can be calibrated using the method (i), i.e. by measuring the revolution frequency of the antiproton beam and readjusting the cathode potential.

Caveat: We mention that sufficient high accuracies can only be obtained at relatively low kinetic energies T and therewith low values of γ. This is due to the fact that

$$\frac{\mathrm{d}T}{T} = \gamma(\gamma+1)\frac{\mathrm{d}\beta}{\beta}. \tag{178}$$

In the electron kinetic energy range 0.45 - 4.5 MeV the relativistic Lorentz factor γ varies between 1.88 and 9.81, and the factor $\gamma(\gamma+1)$ varies between 5.4 and 106. Fortunately, a precise determination of the neutralization η in the EC interaction region is only necessary at low kinetic energies, i.e. for $T_e \leq 1.63$ MeV ($\gamma_e \leq 4.20$, $T_{\bar{p}} \leq 3.0$ GeV), see Subsect. 18.6.

18.3 Stabilization of the EC neutralization

Neutralization experiments at LEAR [49, 50, 51] have shown that instabilities of the neutralization η occur at large electron currents. These instabilities cause energy jumps of the electron beam and the circulating antiproton beam due to the sudden changes of the space charge potential, see factor $(1-\eta)$ in Eq. (162). The energy jumps occur at regular intervals, related to the production time T_p of the trapped ions. The repetitive energy jumps lead to heating and sometimes even to losses of the antiproton beam. This harmful effect can only be avoided by a very strict control of the neutralization level.

In order to stabilize the neutralization level an additional device called 'LEAR shaker' has been installed in LEAR. The 'LEAR shaker' consists of two electrodes, similar in shape to position pick-ups, which act as a transverse kicker. They are excited with a sinusoidal RF-voltage of a few volts and at frequencies of some 100 kHz, in the range of the bounce frequencies of the trapped ions in the electron beam. The RF-voltages heat up the trapped ions and they expel continuously the surplus ions. In this way neutralization levels between $\eta = 0$ and $\eta = 1$ could be stabilized at 1.5 A electron currents [51].

18.4 What is the optimum neutralization of the electron beam at low energies?

Here, we discuss the question: What is the optimum neutralization of the electron beam? To this end, we consider $\Delta p_e/p_e$ and $|v_{az}(a)|/(\beta_e c)$ assuming three different options for η, see Tables 32-34.

A solution with $\eta \approx 0$ has the disadvantage that both, $\Delta p_e/p_e$ and $|v_{az}(a)|/(\beta_e c)$, are rather large at low energies, see Table 32.

Concerning $\Delta p_e/p_e$, the optimum neutralization would be $\eta = 1$, see Table 33. Then, the electron beam would be completely neutralized and the relative momentum deviation $\Delta p_e/p_e$ due to the space charge potential would be zero. However, the azimuthal velocities $|v_{az}|$ of the electron beam and the ratios $|v_{az}(a)|/(\beta_e c)$ would be rather large if $\eta = 1$, see Table 33. The ratio $|v_{az}(a)|/(\beta_e c)$ can be calculated using Eq. (177) in Subsection 17.2. For $\eta = 1$ we get

$$\frac{|v_{az}(a)|}{\beta_e c} = \left(1 - \frac{1}{\gamma_e^2}\right) \frac{1}{\beta_e^2} \frac{I_e}{c^2 2\pi\epsilon_0 B a} = \frac{I_e}{c^2 2\pi\epsilon_0 B a} = 2.00 \cdot 10^{-4}. \tag{179}$$

Since $(1 - 1/\gamma_e^2)/\beta_e^2 = [1 - (1 - \beta_e^2)]/\beta_e^2 = 1$, the ratio $|v_{az}(a)|/(\beta_e c)$ would be independent of the EC beam energy if $\eta = 1$. We note that $|v_{az}(a)|/(\beta_e c) = 2.0 \cdot 10^{-4}$ is much too large and cannot be tolerated.

Unfortunately, it is not possible to achieve simultaneously $\Delta p_e/p_e = 0$ and $|v_{az}(a)|/(\beta_e c) = 0$. Therefore, we suggest to adjust the neutralization $\eta = 1/\gamma_e^2$ as the optimum compromise, see Table 34. Then, $|v_{az}(a)|/(\beta_e c)$ would be zero and the relative momentum deviations $\Delta p_e/p_e$ would be somewhat smaller than with $\eta \approx 0$. The resulting relative momentum deviations $\Delta p_e/p_e$ and the ratio $|v_{az}(a)|/(\beta_e c)$ are listed in Table 34. A stable neutralization with $\eta = 1/\gamma_e^2$ can be achieved by (i) accumulating and trapping the continuously produced ions in the EC interaction region with neutralization electrodes (see Subsect. 18.1) and (ii) using the Ion-Cyclotron-Resonance (ICR) heating for stabilization (see Subsect. 18.5).

According to the HESR Electron Cooler Design Study [43] it is planned to run the EC with $\eta = 0.012$, i.e. $\eta \approx 0$. This option is well suited for the high-energy range. However, at low energies $\Delta p_e/p_e$ as well as $|v_{az}(a)|/(\beta_e c)$ become larger than $1.0 \cdot 10^{-5}$, see Table 32. The deviation of $|v_{az}(a)|/(\beta_e c)$ from $1.0 \cdot 10^{-5}$ becomes even larger if the magnetic field of the EC solenoid is decreased. In this context we note a remark in the HESR Electron Cooler Design Study [43]: 'For experiments to be performed at the injection energy of 3 GeV, or below, there is a desire to lower the magnetic field strength in the HESR ring to allow for compensation of the tune shift.' A kinetic energy of 3 GeV corresponds to $\gamma_e = 4.20$ and $T_e = 1.63$ MeV. Thus, if for instance the magnetic field of the solenoid is reduced by a factor of two, i.e. $B = 0.1$ T, the relative azimuthal velocity $|v_{az}(a)|/(\beta_e c)$ is increased by a factor of two! That means, a very high azimuthal velocity would occur for $\eta \approx 0$ at low energies, for instance $|v_{az}(a)|/(\beta_e c) = 1.58 \cdot 10^{-4}$ at the lowest electron energy 0.45 MeV. This drawback can be avoided by adjusting $\eta = 1/\gamma_e^2$ at low energies.

Table 32: Relative momentum deviations and relative azimuthal velocities due to space-charge effects assuming a neutralization $\eta \approx 0$.

T_e (MeV)	γ_e	η	$\Delta p_e/p_e$	$v_{az}(a)/(\beta_e c)$
0.45	1.88	0	$5.24 \cdot 10^{-5}$	$7.89 \cdot 10^{-5}$
1.5	3.94	0	$1.65 \cdot 10^{-5}$	$1.38 \cdot 10^{-5}$
2.5	5.89	0	$1.04 \cdot 10^{-5}$	$5.93 \cdot 10^{-6}$
3.5	7.85	0	$7.66 \cdot 10^{-6}$	$3.30 \cdot 10^{-6}$
4.5	9.81	0	$6.08 \cdot 10^{-6}$	$2.10 \cdot 10^{-6}$

Table 33: Relative momentum deviations and relative azimuthal velocities due to space-charge effects assuming a neutralization $\eta = 1$.

T_e (MeV)	γ_e	η	$\Delta p_e/p_e$	$v_{az}(a)/(\beta_e c)$
0.45	1.88	1	0	$2.00 \cdot 10^{-4}$
1.5	3.94	1	0	$2.00 \cdot 10^{-4}$
2.5	5.89	1	0	$2.00 \cdot 10^{-4}$
3.5	7.85	1	0	$2.00 \cdot 10^{-4}$
4.5	9.81	1	0	$2.00 \cdot 10^{-4}$

Table 34: Relative momentum deviations and relative azimuthal velocities due to space-charge effects assuming a neutralization $\eta = 1/\gamma_e^2$ (**optimum neutralization**).

T_e (MeV)	γ_e	η	$\Delta p_e/p_e$	$v_{az}(a)/(\beta_e c)$
0.45	1.88	0.283	$3.69 \cdot 10^{-5}$	0
1.5	3.94	0.0646	$1.54 \cdot 10^{-5}$	0
2.5	5.89	0.0288	$1.01 \cdot 10^{-5}$	0
3.5	7.85	0.0162	$7.54 \cdot 10^{-6}$	0
4.5	9.81	0.0104	$6.02 \cdot 10^{-6}$	0

18.5 Stabilization of the optimum neutralization $\eta = 1/\gamma_e^2$ at low energies

In order to adapt the LEAR method to the HESR EC we list in Table 35 the characteristic cyclotron frequencies $f_c = \omega_c/(2\pi)$ and bounce frequencies $f_b = \omega_b/(2\pi)$. We note that the resulting modified cyclotron frequencies ω_+ and the magnetron frequencies ω_- depend considerably on the neutralization η. Taking the neutralization in the expression for ω_b into account the equations for the modified cyclotron frequency ω_+ and the magnetron frequency ω_- may be written in the following form,

$$\omega_\pm = \frac{\omega_c}{2} \pm \sqrt{\left(\frac{\omega_c}{2}\right)^2 + (1 - \eta\gamma_e^2)\omega_b^2(\eta = 0)}. \tag{180}$$

If the neutralization η tends towards $1/\gamma^2$ (i.e. $\eta \to 1/\gamma^2$) we have

$$\omega_+ \to \omega_c \quad \omega_- \to 0. \tag{181}$$

That means the magnetron motion around the beam center tends to zero and we are left with the pure cyclotron motion around the magnetic field lines. These cyclotron frequencies are listed in the second column of Table 35. Thus, in order to achieve a stable neutralization with $\eta = 1/\gamma^2$

Table 35: Cyclotron frequencies $f_c = \omega_c/(2\pi)$ and bounce frequencies $f_b = \omega_b/(2\pi)$ in the HESR EC for $I_e = 1.0$ A, $B = 0.2$ T and $a = 5.0$ mm.

Ion	f_c (kHz)	f_b (kHz) at 0.45 MeV	f_b (kHz) at 4.5 MeV
H_2^+	1525	$\sqrt{1-\eta\gamma_e^2} \times 1854$	$\sqrt{1-\eta\gamma_e^2} \times 1710$
CH_4^+	191	$\sqrt{1-\eta\gamma_e^2} \times 655$	$\sqrt{1-\eta\gamma_e^2} \times 605$
CO^+	109	$\sqrt{1-\eta\gamma_e^2} \times 495$	$\sqrt{1-\eta\gamma_e^2} \times 457$

one can use the Ion-Cyclotron-Resonance (ICR) heating of the ions by adjusting the cyclotron resonance frequencies listed in Table 35. Then, the surplus ions which are continuously produced are heated up resonantly if $\eta = 1/\gamma^2$ is reached. Due to the energy gain by the RF field the cyclotron radius of those ions increases continuously until the ions are neutralized at the vacuum chamber. This process is self-regulating. If η becomes less than $1/\gamma^2$ the cyclotron resonance condition is violated and the ICR heating is stopped since the modified cyclotron frequency $\omega_+ \neq \omega_c$ for $\eta < 1/\gamma^2$, see Eq. (180). Thus, the shaker removes only ions if $\eta = 1/\gamma^2$ is reached.

In the HESR EC nine beam position monitors are foreseen. These position monitors can also be used as shakers by applying the shaker RF voltage to pairs of position pick-up electrodes. In view of the fact that different ion species are produced we suggest to use several beam position monitors as shakers. They can be tuned to be in resonance with the characteristic cyclotron frequencies of the ion species, see Table 35. The surplus ions which are produced outside the shaker positions move along the magnetic field lines with their mean thermal velocities towards the shaker positions where they are immediately neutralized.

18.6 Adjustment of the EC neutralization at higher energies

Finally, we mention that the adjustment of the 'optimum neutralization' $\eta = 1/\gamma_e^2$ is only necessary at the lowest kinetic energies of the antiproton beam $T_{\bar{p}} \leq 3.0$ GeV. The corresponding kinetic energies of the electron beam amount to $T_e \leq 1.63$ MeV ($\gamma_e \leq 4.20$). At higher energies the EC can be operated with $\eta \approx 1.2$ % as foreseen in the HESR Electron Cooler Design Study [43]. This is due to the fact that the relative momentum deviations $\Delta p_e/p_e$ and the relative azimthal velocities $|v_{az}|/\beta_e c$ of the electron beam are sufficiently small at higher energies, see Table 36.

Table 36: Relative momentum deviations and relative azimuthal velocities due to space-charge effects assuming a neutralization $\eta \approx 1.2$ %.

T_e (MeV)	γ_e	η	$\Delta p_e/p_e$	$\lvert v_{az}(a)\rvert/(\beta_e c)$
2.5	5.89	0.012	$1.03 \cdot 10^{-5}$	$3.46 \cdot 10^{-6}$
3.5	7.85	0.012	$7.57 \cdot 10^{-6}$	$8.60 \cdot 10^{-7}$
4.5	9.81	0.012	$6.01 \cdot 10^{-6}$	$3.25 \cdot 10^{-7}$

19. Summary and Conclusions

The first part of the present report (Sects. 1.-9.) serves as introduction to the issue of trapped ions. It provides the basic informations on the HESR layout, the electric field of the antiproton beam, the UHV update, the ionization process, the mean thermal velocities of trapped ions, the production time T_p, the clearing time T_c, the neutralization η, the ion motion in dipole magnets and the ion motion in solenoids. The second part of the report is devoted to the question of how to counteract trapped ion effects in the HESR, see Sects. 10. - 18..

The circulating antiproton beam ionizes the residual gas molecules of the UHV vacuum. The produced ions are trapped in the negative potential well of the antiproton beam. The trapped ions can cause emittance growth, beam instabilities, coherent beam-ion oscillations and beam losses. In order to avoid the adverse effects of trapped ions it is necessary to keep the beam neutralization η as low as possible. This can be achieved using clearing electrodes, see Sects. 10. and 11..

The highest clearing efficiency can be achieved with continuous clearing electrodes along the beam pipe, see Subsects. 10.3 - 10.6. In regions of very low residual gas pressures ($1.0 \cdot 10^{-11}$ mbar $< p < 1.0 \cdot 10^{-9}$ mbar) the trapped ions can be extracted with single isolated clearing electrodes, see Subsect. 10.2. Continuous ion clearing in the region of solenoids is possible using transverse cross-field drift velocities $\vec{v}_D = \vec{E} \times \vec{B}/B^2$, see Sect. 11..

Counteracting trapped ion effects near the internal PANDA target is treated in Sect. 12.. The residual gas pressure is very high ($1.0 \cdot 10^{-9}$ mbar $< p < 6.0 \cdot 10^{-5}$ mbar) near the PANDA target, i.e. between $s = 488$ m and $s = 532$ m. Continuous clearing electrodes can be used in order to counteract the very high production of trapped ions and to keep the neutralization $\eta(s)$ sufficiently low, i.e. $\eta(s) < 1.0 \cdot 10^{-2}$, see Subsect. 12.2.

Continuous clearing electrodes all along the beam pipe near the PANDA target would be the optimum solution of the trapped ion problem. However, it is necessary to consider the constraints due to the PANDA experiment. The possibility to abandon continuous ion clearing in the immediate neighbourhood of the PANDA target, i.e. in the region of the target solenoid and the compensation solenoid is discussed in Subsects. 12.3 and 12.4. The resulting neutralization $\eta(s)$ is shown in Fig. 21, see Subsect. 12.5.

The remaining PANDA target regions between $s = 488$ m and $s = 508$ m and between $s = 512.5$ m and $s = 532$ m consist of a dipole magnet (PANDA Forward Spectrometer), drift spaces, quadrupole magnets and two correction dipole magnets of the PANDA chicane. There, the ion-production rate is still rather high and continuous clearing electrodes are mandatory in order to avoid dangerous ion-beam oscillations, see Subsects. 12.6 - 12.9.

The mitigation of trapped ion effects in the region of the dipole magnets in the arcs is treated in Sect. 13.. In principle, the cross-field drift velocity $v_D = E_x/B_y$ can be used in order to guide the trapped ions to the entrance and exit of the 4.2 m long dipole magnets. But this method is not very efficient since the cross-field drift velocities are very low. Therefore, it has already been planned to improve the UHV vacuum considerably [23] by sputtering thin-film NEG[11] coatings onto the surface of the vacuum chamber and by using heating jackets along the beam tubes. The aim is to achieve residual gas pressures of about $1.0 \cdot 10^{-11}$ mbar.

Unfortunately, the cross-field drift velocity $v_D = E_x/B_y$ vanishes at the beam center. Therefore, ions created near the beam center are practically not cleared, see Subsect. 13.2. In order to avoid the build-up of a trapped ion peak in the beam center we suggest to shift the beam

[11] Non-Evaporating Getter Material

periodically back and forth, see Subsects. 13.3 - 13.6.

The highest clearing efficiencies can be achieved using continuous clearing electrodes inside the 4.2 m long dipole magnets, see Subsect. 13.7. The trapped ions can be extracted vertically along the magnetic field lines. As discussed in Subsect. 10.3 continuous clearing electrodes can be produced by plasma spraying a 0.1 mm thick and 30 mm wide Al_2O_3 layer at the bottom of the beam pipes. On top of the isolating layer a 25 mm wide highly resistive thick film coating can be applied. Using clearing voltages of -1.0 kV yields electric fields of about 640 V/m at the beam center. The resulting clearing rates are so high that even UHV pressures of less than $1.0 \cdot 10^{-9}$ mbar can be tolerated.

Another possibility to achieve continuous ion clearing in dipole magnets has been discussed in Subsect. 13.8. Thereby, the beam pipe consists of two metallic half-cylinders separated by high-resistive-glass insulators. Applying opposite voltages $+U_0$ and $-U_0$ yields an electric field component E_y which can be used in order to extract the produced ions.

Anyway, we recommend the installation of continuous clearing electrodes inside the dipole magnets, even if they are not needed at the beginning. They can always be used if problems with the ultra-high vacuum occur.

The possibility to damp coherent ion-beam oscillations is discussed in Sect. 14.. These collective oscillations of the beam center (dipole mode) or the beam shape (quadrupole mode) grow exponentially due to the interaction of the beam with the trapped ions. The most dangerous mode is the dipole mode, i.e. the coherent oscillation of the beam center. Under specific conditions the coherent instabilities can be suppressed by Landau damping if the tune spreads of beam and ion oscillations are sufficiently large, see Subsect. 14.3. Another possibility is the active damping of beam instabilities using feedback systems, see Subsect. 14.6.

Under certain conditions one can also use beam shaking in order to remove trapped ions and to decrease the neutralization η in regions where the clearing electrodes cannot remove trapped ions sufficiently, see Sect. 15.. Transverse kickers can be used in order to excite coherent oscillations of the beam. Thus, the beam is shaken by the applied RF field of a shaking kicker and the oscillating beam shakes the ions. This method works if the shaking frequency ω is close to one of the sideband frequencies $(n-Q)\omega_0$ ('slow wave' frequency) or $(n+Q)\omega_0$ ('fast wave' frequency) and close to the ion bounce frequency $q_c\omega_0$. A consequence of the resonance condition is the fact that clearing of trapped ions by shaking is only possible at specific positions in the ring and for light ions like H^+ and H_2^+. Heavier ions cannot be removed by beam shaking. In addition, we mention that beam shaking deteriorates the transverse beam quality. This fact must be taken into account when applying beam shaking in the HESR ring.

The problem of trapped ions in the electron cooler (EC) beam and methods to counteract trapped ion effects are discussed in Sects. 16. - 18.. The EC beam is guided by a 24 m long solenoid with a constant beam radius of 5 mm. The EC beam current (1.0 A) is very much larger than the current of the circulating antiproton beam. As a consequence, the EC potential well acts as a very deep pocket for trapped ions. The trapped ions perform modified cyclotron motions around the magnetic field lines of the solenoid and magnetron motions around the central axis of the EC beam. According to the electron cooler design study [43] it is planned to remove the trapped ions with clearing electrodes near the entrance and exit of the straight cooling section. The resulting mean neutralization η from H_2, CO and CH_4 amounts to about 1.2 %.

However, it is not always desirable to keep the beam neutralization as small as possible. Especially at low energies the drawbacks of the large space-charge potential of the EC beam are

rather large, see Sect. 17.:
(i) The cooling efficiency is deteriorated by the space-charge potential of the electron beam which causes a significant radial dependence of the electron energies, see Subsection 17.1.
(ii) The cooling efficiency is deteriorated by the azimuthal cross-field drift velocity of the electrons which is caused by the electric field of the electron beam, see Subsection 17.2.

Both effects can be mitigated by adjusting a certain neutralization of the electron beam at low energies, see Sect. 18.. The optimum neutralization is reached if $\eta = 1/\gamma_e^2$, see Subsect. 18.4. Then, the azimuthal cross-field drift velocity of the electrons is zero and the EC space-charge potential is reduced. In order to achieve a stable neutralization with $\eta = 1/\gamma_e^2$ one can use the Ion-Cyclotron-Resonance (ICR) heating. The surplus ions which are produced continuously are heated up resonantly. To this end, the nine beam position monitors can also be used as ion shakers by applying the RF voltage to pairs of position pick-up electrodes. They can be tuned to be in resonance with the characteristic cyclotron frequencies of the trapped ions.

The application of beam shakers has the additional benefit that instabilities of the neutralization η can be prevented. Such instabilities can occur at large EC beam currents [49, 50, 51]. They cause energy jumps of the electron beam due to sudden changes of the space-charge potential. This harmful effect can only be avoided by a strict control and stabilization of the neutralization level.

ACKNOWLEDGEMENTS

I would like to thank Jacques Bosser, Kai-Thomas Brinkmann, Fritz Caspers, Alexander Gruber, Andreas Lehrach, Jürgen Dietrich, Olaf Felden, Bjorn Galnander, Ralf Gebel, Wolfgang Hillert, Alfons Khoukaz, Bernd Lorentz, Rudolf Maier, Dieter Möhl, Alain Poncet, Dieter Prasuhn, Rolf Stassen, Hans Stockhorst, Raimund Tölle and Gerard Tranquille for helpful informations and discussions.

References

[1] F. Hinterberger, Ion Trapping in the High-Energy Storage Ring HESR, Juelich Report 4343 (2011).

[2] P. Zenkevich, O. Boine-Frankenheim and P. Alexeev, Trapped Particle Effects in the HESR Storage Ring, GSI-Acc-Note-2006-03-004 (2006).

[3] P. Zenkevich, Inter-Species Effects in the HESR, Internal HESR Note (2009).

[4] FAIR Baseline Technical Report 2006 (FBTR 2006) GSI Darmstadt, March 2006, see http://www.fair-center.de/fileadmin/fair/publications_FAIR/FAIR_BTR_6.pdf.

[5] Design Work For the High-Energy Storage Ring of the Future GSI Project, A. Lehrach et al., Proceedings of 2005 Particle Accelerator Conference, Knoxville, Tennessee (USA) (2005).

[6] Strong Interaction Studies with Antiprotons, Letter of Intent, PANDA Collaboration, January 2004, see FAIR Baseline Technical Report 2006 (FBTR 2006), http://www.fair-center.de/fileadmin/fair/publications_FAIR/FAIR_BTR_6.pdf.

[7] Antiproton-Proton Scattering Experiments with Polarization, Letter of Intent, PAX Collaboration, January 2004, see FAIR Baseline Technical Report 2006 (FBTR 2006), http://www.fair-center.de/fileadmin/fair/publications_FAIR/FAIR_BTR_6.pdf.

[8] F. Rathmann et al., A Method to Polarize Stored Antiprotons to a High Degree, Phys. Rev. Lett. **94** (2005) 014801.

[9] A Study of Spin-dependent Interactions with Antiprotons, Letter of Intent, ASSIA Collaboration, January 2004, see FAIR Baseline Technical Report 2006 (FBTR 2006), http://www.fair-center.de/fileadmin/fair/publications_FAIR/FAIR_BTR_6.pdf.

[10] D.G. Koshkarev and P.R. Zenkevich, Resonance of Coupled Transverse Oscillations in Two Circular Beams, Particle Accelerators **3** (1972) 1.

[11] L.J. Laslett, A.M. Sessler and D. Möhl, Nucl. Instr. and Meth. **121** (1974) 517.

[12] E. Keil and B. Zotter, CERN-ISR-TH/79-58 (1979).

[13] Y. Baconnier, Neutralization of Accelerator Beams by Ionization of the Residual Gas, CERN Accelerator School, Gif-sur-Yvette, Paris, 1984, CERN 85-19 (1985).

[14] R. Alves-Pires et al., On the Theory of Coherent Instabilities Due to Coupling a Dense Cooled Beam and Charged Particles from the Residual Gas, Particle Accelerator Conference Chicago 1989, IEEE (1989), CERN/PS/89-14 (AR) (1989).

[15] A. Poncet, Ions and Neutralization, in Frontiers of Particle Beams: Intensity Limits, eds. M. Dienes, M. Month, S. Turner, Springer Verlag LNP, p. 488 (1990).

[16] A. Poncet, Ions Trapping and Clearing, CERN/US CAS (1992), CERN MT/93-01

[17] P. Zhou, A Study of Ion Trapping and Instability in the FERMILAB Antiproton Accumulator, PhD Thesis, Northwestern University (1993).

[18] Y. Baconnier, A. Poncet, and P.F. Tavares, Neutralization of Accelerator Beams by Ionisation of the Residual Gas, CAS Proc. CERN 94-01, p.525 (1994).

[19] A. Poncet, Ion Trapping and Clearing, CAS Proc. CERN 95-06, p.859 (1995).

[20] A. Poncet, Ion Trapping, Clearing, Beam-Ion Interactions, CERN Accelerator School CERN99-05, Snekersen, Denmark, 165 (1999).

[21] D. Neuffer and K.Y. Ng, Thoughts on Ion Trapping Instability in the Recycler, Fermilab Report FERMILAB-TM-2256 (2004).

[22] HESR List of Technical Parameters, compiled by K. Bongardt and R. Tölle, Status July 2011, Internal HESR Homepage, http://www2.fz-juelich.de/ikp//hesr/HesrTechnicalParameters_20110715_approved.pdf (2009), R. Tölle, private communication (e-mail: r.toelle@fz-juelich.de).

[23] D. Prasuhn, private communication (2011).

[24] A. Gruber: Development of the cluster-jet target and the interaction region of the PANDA detector; Dr.-Thesis, Universität Wien, to be published.

[25] A. Khoukaz, H. Orth, M. Büscher, P. Fedorets, H. Calen, A. Gruber, J. Zmeskal, D. Prasuhn, A. Lehrach, A. Bersani: Technical Design Report for the PANDA Internal Targets: The Cluster-Jet Target and Developments for the Pellet Target, PANDA Collaboration (2011), http://www.uni-muenster.de/Physik.KP/AGKhoukaz_Files/TechRep/Targets_TDR.pdf.

[26] A. Poncet, private communication (2010).

[27] A. Poncet, private communication (2011)

[28] T. Kroyer et al., A New Type of Distributed Enamel Based Clearing Electrodes, Proc. PAC07, Albuquerque (2007), http://accelconf.web.cern.ch/AccelConf/p07/PAPERS/WEOAC02.PDF.

[29] Fritz Caspers, private communication (2011).

[30] H. Suetsugu et al., Beam Tests of a Clearing Electrode for Electron Mitigation at KEKB Positron Ring, IPAC2010 http://accelconf.web.cern.ch/AccelConf/IPAC10/talks/weoamh01_talk.pdf.

[31] Heraeus Product Information Hybrid Pastes, http://heraeus-thickfilm.com/en/productsapplications/hybridpastes/hybrid_pastes_1.aspx

[32] M. Bassetti and G.A. Erskine, Closed Expression for the Electrical Field of a Two-Dimensional Gaussian Charge, Internal Publication CERN-ISR-TH/80-06, CERN (1980).

[33] J.D. Jackson, Classical Electrodynamics, 2nd edition, Sections 12.4 and 12.5, John Wiley & Sons, New York (1975).

[34] R. Macek and M. Pivi, ExB Drift of e-cloud in a PSR Quadrupole and Dipole, Technical Note of 3/28/05 posted to the ILC website: http://www-project.slac.stanford.edu/ilc/testfac/ecloud/files/ExB_Drift_of_e-cloud_PSRquad_dipole_v9c.pdf.

[35] P.F. Tavares, Transverse Distribution of Ions Trapped in an Electron Beam, CERN-PS/92-55 (LP) (1992).

[36] A.W. Hull, The Effect of a Uniform Magnetic Field on the Motion of Electrons between Coaxial Cylinders, Phys. Rev. **18** (1921) 31.

[37] F.M. Penning, Physica (Utrecht) **3** (1936) 873.

[38] L.S. Brown and G. Gabrielse, Rev. Mod. Phys. **58** (1986) 233.

[39] K. Blaum, Phys. Rep. **425** (2006) 1.

[40] The Panda Collaboration, Technical Design Report for the PANDA Solenoid and Dipole Spectrometer Magnets, http://arxiv.org/pdf/0907.0169v1.pdf (2009).

[41] The Panda Collaboration, Technical Design Report for the PANDA Internal Targets: The Cluster-Jet Target and Developments for the Pellet Target, http://www.uni-muenster.de/Physik.KP/AGKhoukaz_Files/TechRep/Targets_TDR.pdf (2012).

[42] Rudolf Maier, private communication (2011).

[43] HESR-EC Group at Uppsala University, HESR Electron Cooler Design Study, Final Report (2009), see http://www5.tsl.uu.se/hesr/.

[44] Lionel Prost, private communication (2010).

[45] F. Pedersen and A. Poncet, Proton-antiproton instability in the CERN AA, CERN PS/AA/ME Note 81 (1981).

[46] V. Kamerdzhiev, Untersuchung und Verbesserung des Stabilitätsverhaltens eines intensiven elektronengekühlten Teilchenstrahls in COSY, Berichte des Forschungszentrums Jülich 4114, ISSN 0944-2952, Institut für Kernphysik, Jül-4114, D290 (Diss. Dortmund Univ. 2003), e-mail: zb-publikation@fz-juelich.de.

[47] Dieter Prasuhn, private communication (2011).

[48] S.J. Werkema, Control of Trapped Ion Instabilities in the Fermilab Antiproton Accumulator, 16th IEEE Part. Acc. Conf. and Int. Conf. on High-Energy Accelerators, 3397 (1996).

[49] J. Bosser et al., Proceedings of the Particle Accelerator Conference PAC95, www.epaper.kek.jp/p.95/ (1995).

[50] J. Bosser, Review of Recent Work on Electron Cooling at LEAR, CER-PS/96-13 (AR) (1996).

[51] J. Bosser et al., Stability of Cooled Beams, Nucl. Instr. and Meth. in Phys. Res. A **441** (2000) 1.

[52] D. Möhl, private communication (2011).

Jül-4357
Oktober 2012
ISSN 0944-2952